

Enclosure 2

MFN 09-210

**Submittal of NEDO-33239 Revision 4
“GE14 for ESBWR Nuclear Design Report”**



Global Nuclear Fuel

A Joint Venture of GE, Toshiba, & Hitachi

NEDO-33239
Revision 4
eDRF 0000-0062-3232
Class I
March 2009

GLOBAL NUCLEAR FUELS – AMERICAS NON-PROPRIETARY INFORMATION

Licensing Topical Report

**GE14 FOR ESBWR
NUCLEAR DESIGN REPORT**

Vernon W. Mills

Xavier Mouney

Gregory J. Pearson

*COPYRIGHT 2009 GLOBAL NUCLEAR FUELS-AMERICAS, LLC
ALL RIGHTS RESERVED*

INFORMATION NOTICE

This document is the non-proprietary version of NEDC-33239P, Revision. 4, and thus, has the proprietary information removed. Portions of this document that have been removed are indicated by open and closed double brackets, as shown here [[]].

IMPORTANT NOTICE REGARDING CONTENTS OF THIS REPORT

Please Read Carefully

The information contained in this document is furnished as reference material for GE14E for ESBWR, Nuclear Design Report. The only undertakings of Global Nuclear Fuel (GNF) with respect to information in this document are contained in the contracts between GNF and the participating utilities in effect at the time this report is issued, and nothing contained in this document shall be construed as changing those contracts. The use of this information by anyone other than that for which it is intended is not authorized; and with respect to any unauthorized use, GNF makes no representation or warranty, and assumes no liability as to the completeness, accuracy, or usefulness of the information contained in this document.

Copyright, Global Nuclear Fuel - Americas, LLC, 2009, All Rights Reserved.

LIST OF CONDITIONS OF USE FOR ESBWR

1. TGBLA06 is not approved to analyze fuel lattices with gadolinia burnable poison loadings in excess of [[]] gadolinia until the gadolinia bias has been quantified and reviewed by the NRC staff.
2. Licensing evaluations performed with PANAC11 shall use bypass flow fractions consistent with all core operating states as determined by TRACG04 and input in the core-simulator in order to accurately determine the bypass flow. Bypass flow tables or explicit modeling of data from TRACG04 can be used for PANAC11 input values.
3. The bypass voiding will be evaluated on a cycle-specific basis to confirm that the void fraction remains below five percent (5%) at all LPRM levels when operating at steady-state conditions at the upper boundary of the allowable operating domain.
4. The bundle R-factor must be calculated using representative lattice pin power distributions and axial void and power profiles.
5. The SCRAM reactivity calculated using the PANAC11 neutronic solver must be calculated with Doppler reactivity feedback modeling activated to accurately determine the reactivity effect of the blades without including the Doppler reactivity in the SCRAM reactivity.
6. For the Standby Liquid Control System Shutdown Analysis the TGBLA06 borated libraries shall be generated with lattice boron inventories between 600 ppm and 1000 ppm natural boron equivalent.
7. The regional mode stability analysis must be performed using a radial nodalization in TRACG04 based on the PANAC11 generated first harmonic mode. The harmonic calculation performed by PANAC11 must use a full-core representation.
8. Use of PANAC11 generated nuclear data for ESBWR reload transient analyses (AOO, stability, or ATWS) requires that TRACG utilize the void reactivity coefficient correction model described in NEDE-32906P-A, Supplement 3. The fuel lattices input to the model must be representative of the cycle specific fuel loading.

9. The limitations on TGBLA06 and PANAC11 code usage as described in the user manuals are a condition of the acceptance of these methodologies for the ESBWR. Changes to the manuals that are made in accordance with the quality assurance procedures audited by the staff as documented in the applicable reference do not require NRC review and approval. These changes, however, must be documented in the cycle-specific Supplemental Reload Licensing Report (SRLR) if utilized in the safety analysis.
10. Modifications to the models described in NEDC-33239P-A or MFN 098-96 are considered by the NRC staff to constitute a departure from a method of evaluation in the safety analysis and may not be used for licensing calculations without prior NRC review and approval.
11. Modifications to the TGBLA06/PANAC11 codes that result in inconsistency with the NEDC-33239P-A LTR are considered by the NRC staff to constitute a departure from a method of evaluation in the safety analysis and may not be used for licensing calculations without prior NRC review and approval of the necessary revision(s) to the LTR.
12. Updates to the PANAC11 nuclear methods to ensure compatibility with other NRC approved methods are not considered by the NRC staff to constitute a departure from a method of evaluation in the safety analysis. These updates may be used for licensing calculations without prior NRC review and approval as long as the predicted ESBWR equilibrium cycle MLHGR or the downstream DCPR/ICR for the potentially limiting transients (calculated by TRACG04) show less than a one standard deviation difference.
13. Increases in the spatial or energy resolution in the TGBLA06 lattice physics method would not be considered by the NRC staff to constitute a departure from a method of evaluation in the safety analysis (i.e. may be used for licensing calculations without prior NRC review and approval) so long as the uncertainties in the lattice parameters do not increase as a result. In all cases, the modifications or updates done without prior NRC review and approval will be documented in the cycle specific Supplemental Reload Licensing Report (SRLR) if utilized in the safety analysis.
14. Changes in the numerical methods to improve code convergence are not considered by the NRC staff to constitute a departure from a method of evaluation in the safety analysis and may be used in the licensing calculations without prior NRC review and approval.”

CHANGES FROM REVISION 3 TO REVISION 4

1. Purpose

The purpose of Revision 4 is to document modified bundle designs and a reconfigured equilibrium core design that were optimized at a lower TRACG predicted core flow. The lower predicted core flow can be attributed to a correction of the GE14E spacer loss coefficients in the TRACG simulations. The spacer loss coefficients have now been consistently applied in TRACG and in PANACEA based on the same measured pressure drop data base. Standard BWR core design options were exercised in order to improve thermal margins at the lower core flow. These options included:

- Bundle shuffling to flatten radial power, primarily in the peripheral core region.
- Control rod pattern changes, with major sequence adjustments performed every 3000 MWd/ST.
- Reduction in bundle pin powers resulting in improved bundle R-factors.

The modified bundle designs and reconfigured equilibrium core design with key performance results have been documented in this revision.

Note that another key change is that all PANACEA evaluations for the equilibrium core have been performed with revised axial nodalization. The number of axial nodes was reduced from 25 to 20. And the total number of control rod notches was reduced from 100 to 80.

This revision also incorporates a list of conditions of use for ESBWR as documented in MFN 09-073 Enclosure 1.

2. Summary of Revisions

Section 1 contains various minor formatting improvements and grammatical or typographical corrections.

Section 1.6.5, in the first sentence of the first paragraph, the phrase “single control blade withdrawn” was replaced with “single control rod or rod pair withdrawn”.

Section 3 was replaced in its entirety with new Sections 3 and 4. The new Section 3 contains all bundle related data while Section 4 contains all core design and performance related data.

Section 4 reports reactivity coefficient analysis results based on both xenon free and high xenon conditions. Earlier revisions included analysis results based on only xenon free conditions.

TABLE OF CONTENTS

1. NUCLEAR METHODS	1-1
1.1 INTRODUCTION.....	1-1
1.2 GENERAL DESCRIPTION OF LATTICE PHYSICS SOLUTION TECHNIQUES.....	1-4
1.2.1 Thermal Neutron Spectrum and Diffusion Parameter Calculations	1-5
1.2.2 Fast and Epi-thermal Spectrum and Diffusion Parameter Calculations	1-11
1.2.3 Bundle Flux, Power, and Miscellaneous Calculations.....	1-15
1.2.4 Nuclide Depletion Calculation.....	1-21
1.3 LATTICE PHYSICS METHODS QUALIFICATION.....	1-26
1.3.1 Monte Carlo Benchmark Comparison	1-26
1.3.2 Conclusions.....	1-36
1.4 THREE-DIMENSIONAL NUCLEAR MODEL	1-37
1.4.1 Coarse-Mesh Nodal, One-Group Diffusion Theory	1-38
1.4.2 Void and Exposure Effects	1-42
1.4.3 Control Rod Effects	1-44
1.4.4 Doppler Effects	1-44
1.4.5 Xenon Effects.....	1-45
1.4.6 Conversion of Flux to Power	1-46
1.4.7 Isotopic Tracking	1-49
1.4.8 In-Core Instrumentation Calculation	1-49
1.4.9 Power-Void Iteration	1-49
1.4.10 Core Geometry for Nuclear Model	1-52
1.5 THERMAL-HYDRAULICS MODEL.....	1-56
1.5.1 Flow Distribution	1-56
1.5.2 Enthalpy-Quality Distribution Calculation	1-68
1.5.3 Void Distribution	1-70
1.5.4 Bypass Region Calculation	1-78
1.5.5 Total Core Energy Balance	1-79
1.5.6 Thermal Limits Calculation	1-79
1.6 THREE-DIMENSIONAL SIMULATOR MODEL QUALIFICATION	1-82
1.6.1 Introduction.....	1-82
1.6.2 Fine Mesh Diffusion Comparison.....	1-82
1.6.3 Gamma Scan Comparisons	1-85
1.6.4 Plant Tracking Results	1-88
1.6.5 Cold Critical Measurements	1-94
1.6.6 TIP Data Summary for the Cycles Studied.....	1-97
1.6.7 Conclusions.....	1-103
1.7 Reactivity Coefficient Methods.....	1-103
2. NUCLEAR DESIGN BASES.....	2-1
2.1 Negative Reactivity Feedback Bases	2-1
2.2 Control Requirements (Shutdown Margins).....	2-1
2.3 Control Requirements (Overpower Bases).....	2-1
2.3.1 Maximum Linear Heat Generation Rate.....	2-1

2.3.2	Minimum Critical Power Ratio.....	2-2
2.4	Control Requirements (Standby Liquid Control System)	2-2
2.5	Stability Bases.....	2-2
3.	BUNDLE NUCLEAR DESIGN EVALUATION.....	3-1
3.1	Introduction.....	3-1
3.2	Bundle and Lattice Designs.....	3-1
3.2.1	GE14E Bundle Design Features for Equilibrium Core.....	3-2
3.2.2	Bundle Local Peaking	3-2
3.2.3	Bundle R-Factor	3-2
3.2.4	Doppler Reactivity Coefficient	3-2
3.3	Summary.....	3-3
4.	CORE NUCLEAR DESIGN EVALUATION.....	4-1
4.1	INTRODUCTION.....	4-1
4.2	Nuclear Design and Core Loading Pattern Description.....	4-1
4.3	Eigenvalue Determination.....	4-2
4.4	Control Rod Patterns Including Axial Power Considerations	4-2
4.5	Integrated Power Distribution.....	4-3
4.6	Thermal Limit Evaluation	4-3
4.6.1	MLHGR	4-3
4.6.2	MCPR	4-4
4.7	Hot Excess Evaluation	4-4
4.8	Cold Shutdown Margin Evaluation	4-5
4.9	Standby Liquid Control System Evaluation.....	4-6
4.10	Criticality of Reactor During Refueling Evaluation.....	4-6
4.11	Negative Reactivity Feedback Evaluation	4-6
4.11.1	Moderator Temperature Coefficient Evaluation	4-7
4.11.2	Moderator Void Coefficient Evaluation	4-7
4.12	Xenon Stability Evaluation	4-8
4.12.1	BWR Xenon Trends.....	4-8
4.12.2	EBWR Xenon Transient Response Analysis.....	4-9
4.12.3	ESBWR Xenon Transient Conclusions	4-10
5.	REFERENCES.....	5-1

LIST OF TABLES

TABLE 1-1. GROUP STRUCTURE OF THERMAL LIBRARY	1-6
TABLE 1-2. NEUTRON BALANCE COMPARISONS BETWEEN MONTE CARLO AND LATTICE PHYSICS	1-30
TABLE 1-3. NEUTRON BALANCE COMPARISONS BETWEEN MONTE CARLO AND LATTICE PHYSICS	1-31
TABLE 1-4. SAMPLE RELATIVE FISSION DENSITY COMPARISON BETWEEN MONTE CARLO AND LATTICE PHYSICS.....	1-32
TABLE 1-5. 10X10 LATTICE WITH VANISHED RODS AT 0.40 VOID FRACTION	1-33
TABLE 1-6. SUMMARY OF RELATIVE FISSION DENSITY COMPARISON BETWEEN MONTE CARLO AND LATTICE PHYSICS	1-35
TABLE 1-7. CORRELATING FUNCTIONS FOR DISTRIBUTION PARAMETER, C_0	1-72
TABLE 1-8. CORRELATING FUNCTIONS FOR DRIFT VELOCITY, \bar{V}_{gj}	1-73
TABLE 1-9. SUBCOOLED BOILING CORRELATING FUNCTIONS	1-75
TABLE 1-10. VOID FRACTION CORRELATING FUNCTIONS	1-76
TABLE 1-11. VOID FRACTION CORRELATING FUNCTIONS (CONTINUED).....	1-77
TABLE 1-12. PLANT DESCRIPTION FOR DIF3D BENCHMARK STUDY	1-83
TABLE 1-13. HATCH 1 GAMMA SCAN COMPARISONS.....	1-86
TABLE 1-14. KEY CORE PARAMETERS FOR REFERENCE PLANTS.....	1-89
TABLE 1-15. EXPOSURE ACCOUNTING DATA FOR PLANT A, CYCLE 18	1-91
TABLE 1-16. COLD CRITICAL EIGENVALUES FOR ALL STUDIED CYCLES	1-95
TABLE 1-17. TIP COMPARISONS FOR THE STUDIED CYCLES	1-98
TABLE 3-1. LATTICE 8859 K-INFINITY	3-12
TABLE 3-2. LATTICE 8860 K-INFINITY	3-13
TABLE 3-3. LATTICE 8861 K-INFINITY	3-14
TABLE 3-4. LATTICE 8862 K-INFINITY	3-15
TABLE 3-5. LATTICE 8863 K-INFINITY	3-16
TABLE 3-6. LATTICE 8864 K-INFINITY	3-17
TABLE 3-7. LATTICE 8865 K-INFINITY	3-18
TABLE 3-8. LATTICE 8866 K-INFINITY	3-19
TABLE 3-9. LATTICE 8867 K-INFINITY	3-20
TABLE 3-10. LATTICE 8859 PEAKING.....	3-21
TABLE 3-11. LATTICE 8860 PEAKING.....	3-22
TABLE 3-12. LATTICE 8861 PEAKING.....	3-23

TABLE 3-13. LATTICE 8862 PEAKING	3-24
TABLE 3-14. LATTICE 8863 PEAKING	3-25
TABLE 3-15. LATTICE 8864 PEAKING	3-26
TABLE 3-16. LATTICE 8865 PEAKING	3-27
TABLE 3-17. LATTICE 8866 PEAKING	3-28
TABLE 3-18. LATTICE 8867 PEAKING	3-29
TABLE 3-19. BUNDLE 3194 UNCONTROLLED AND CONTROLLED R-FACTORS	3-32
TABLE 3-20. BUNDLE 3195 UNCONTROLLED AND CONTROLLED R-FACTORS	3-33
TABLE 3-21. LATTICE 8860 K_{∞}	3-36
TABLE 3-22. LATTICE 8864 K_{∞}	3-37
TABLE 4-1. HOT DESIGN EIGENVALUES	4-12
TABLE 4-2. COLD DESIGN EIGENVALUES	4-13
TABLE 4-3. AXIAL NODAL POWER SEQ-1	4-21
TABLE 4-4. AXIAL NODAL POWER SEQ-2	4-22
TABLE 4-5. AXIAL NODAL POWER SEQ-3	4-23
TABLE 4-6. AXIAL NODAL POWER SEQ-4	4-24
TABLE 4-7. AXIAL NODAL POWER SEQ-5	4-25
TABLE 4-8. AXIAL NODAL POWER SEQ-6	4-26
TABLE 4-9. NODAL EXPOSURE SEQ-1	4-27
TABLE 4-10. NODAL EXPOSURE SEQ-2	4-28
TABLE 4-11. NODAL EXPOSURE SEQ-3	4-29
TABLE 4-12. NODAL EXPOSURE SEQ-4	4-30
TABLE 4-13. NODAL EXPOSURE SEQ-5	4-31
TABLE 4-14. NODAL EXPOSURE SEQ-6	4-32
TABLE 4-15. HOT K-EFF VS EXPOSURE.....	4-33
TABLE 4-16. MAXIMUM RPF VS EXPOSURE	4-35
TABLE 4-17. MFLPD VS EXPOSURE.....	4-48
TABLE 4-18. MCPR VS EXPOSURE.....	4-61
TABLE 4-19. HOT EXCESS REACTIVITY	4-74
TABLE 4-20. COLD SHUTDOWN MARGIN.....	4-76
TABLE 4-21. SLCS SHUTDOWN MARGIN	4-83
TABLE 4-22. EIGENVALUES FOR MTC – ZERO XENON.....	4-84
TABLE 4-23. MTC WITHOUT XENON.....	4-85

TABLE 4-24. EIGENVALUES FOR MVC - ZERO XENON.....	4-86
TABLE 4-25. MVC WITHOUT XENON	4-87
TABLE 4-26. EIGENVALUES FOR MTC/XENON	4-88
TABLE 4-27. MTC WITH XENON	4-89
TABLE 4-28. EIGENVALUES FOR MVC/XENON.....	4-90
TABLE 4-29. MVC WITH XENON.....	4-91

LIST OF ILLUSTRATIONS

FIGURE 1-1. TYPICAL BUNDLE CONFIGURATION	1-2
FIGURE 1-2. LATTICE PHYSICS CODE FLOW DIAGRAM.....	1-3
FIGURE 1-3. FLOW DIAGRAM FOR THE LATTICE PHYSICS/BWR CORE SIMULATOR SYSTEM	1-3
FIGURE 1-4. AN EQUIVALENT FUEL CELL	1-8
FIGURE 1-5 GEOMETRIC RELATIONSHIP BETWEEN THE ONE-DIMENSIONAL EQUIVALENT AND THE ACTUAL BUNDLES	1-14
FIGURE 1-6. TYPICAL MESH POINT AND ITS NEAREST NEIGHBORS	1-17
FIGURE 1-7. FISSIONABLE NUCLIDE CHAINS	1-23
FIGURE 1-8. FISSION PRODUCT NUCLIDE CHAINS.....	1-24
FIGURE 1-9. COMPARISON OF K-INFINITIES FOR BEGINNING-OF-LIFE LATTICES (TGBLA06 vs. MCNP).....	1-27
FIGURE 1-10. COMPARISON OF K-INFINITIES FOR EXPOSED LATTICES (TGBLA06 vs. MCNP)	1-28
FIGURE 1-11. K-INFINITY COMPARISON OF TGBLA06 vs. MCNP FOR VARIOUS LATTICE STATE CONDITIONS.....	1-36
FIGURE 1-12. PIECEWISE-LINEAR FLUX VARIATION.....	1-41
FIGURE 1-13. THERMAL FLUX VARIATION WITHIN AND BETWEEN NODES	1-48
FIGURE 1-14. POWER-VOID ITERATION FLOW CHART.....	1-51
FIGURE 1-15. NODE AND MESH ARRANGEMENT FOR A GIVEN CHANNEL.....	1-52
FIGURE 1-16. BWR SYMMETRY OPTIONS	1-53
FIGURE 1-17. CHANNEL AND FUEL TYPES	1-54
FIGURE 1-18. CONTROL ROD AND MONITOR POSITIONS.....	1-55
FIGURE 1-19. SCHEMATIC OF CHARACTERISTIC CHANNEL NODALIZATION.....	1-62
FIGURE 1-20. FLOW CHANNEL GEOMETRY.....	1-69
FIGURE 1-21. QUARTER CORE HOT BENCHMARKS: EIGENVALUE DIFFERENCE BETWEEN DIF3D AND PANACEA	1-83
FIGURE 1-22. QUARTER CORE HOT BENCHMARKS: NODAL POWER RMS DIFFERENCES BETWEEN DIF3D AND PANACEA.....	1-84
FIGURE 1-23. QUARTER CORE HOT BENCHMARKS: NODAL PEAK TO PEAK POWER DIFFERENCES BETWEEN DIF3D AND PANACEA	1-84
FIGURE 1-24. BUNDLE GAMMA SCAN COMPARISON FOR CYCLE 1	1-87
FIGURE 1-25. BUNDLE GAMMA SCAN COMPARISON FOR CYCLE 3	1-88
FIGURE 1-26 HOT CRITICAL EIGENVALUE FOR STUDIED BWR CYCLES.....	1-90
FIGURE 1-27. COLD CRITICAL EIGENVALUES FOR ALL CYCLES STUDIED	1-97

FIGURE 3-1. BUNDLE DESIGN FOR 3194.....	3-4
FIGURE 3-2. FUEL RODS FOR 3194.....	3-5
FIGURE 3-3. FUEL ROD AXIAL PROFILES FOR 3194	3-6
FIGURE 3-4. SPLITS AND WEIGHTS FOR 3194.....	3-7
FIGURE 3-5. BUNDLE DESIGN FOR 3195.....	3-8
FIGURE 3-6. FUEL RODS FOR 3195.....	3-9
FIGURE 3-7. FUEL ROD AXIAL PROFILES FOR 3195	3-10
FIGURE 3-8. SPLITS AND WEIGHTS FOR 3195.....	3-11
FIGURE 3-10. LATTICE 8860 K-INFINITY	3-13
FIGURE 3-11. LATTICE 8861 K-INFINITY	3-14
FIGURE 3-12. LATTICE 8862 K-INFINITY	3-15
FIGURE 3-13. LATTICE 8863 K-INFINITY	3-16
FIGURE 3-14. LATTICE 8864 K-INFINITY	3-17
FIGURE 3-15. LATTICE 8865 K-INFINITY	3-18
FIGURE 3-16. LATTICE 8866 K-INFINITY	3-19
FIGURE 3-17. LATTICE 8867 K-INFINITY	3-20
FIGURE 3-18. LATTICE 8859 MAXIMUM LOCAL PEAKING	3-21
FIGURE 3-19. LATTICE 8860 MAXIMUM LOCAL PEAKING	3-22
FIGURE 3-20. LATTICE 8861 MAXIMUM LOCAL PEAKING	3-23
FIGURE 3-21. LATTICE 8862 MAXIMUM LOCAL PEAKING	3-24
FIGURE 3-22. LATTICE 8863 MAXIMUM LOCAL PEAKING	3-25
FIGURE 3-23. LATTICE 8864 MAXIMUM LOCAL PEAKING	3-26
FIGURE 3-24. LATTICE 8865 MAXIMUM LOCAL PEAKING	3-27
FIGURE 3-25. LATTICE 8866 MAXIMUM LOCAL PEAKING	3-28
FIGURE 3-26. LATTICE 8867 MAXIMUM LOCAL PEAKING	3-29
FIGURE 3-27. ROD LOCAL PEAKING (BUNDLE 3194, LATTICE 8860, VF=40%, BOL)	3-30
FIGURE 3-28. ROD LOCAL PEAKING (BUNDLE 3195, LATTICE 8864, VF=40%, BOL).....	3-31
FIGURE 3-29. UNCONTROLLED ROD R-FACTORS (BUNDLE 3194, 20 GWD/ST).....	3-34
FIGURE 3-30. UNCONTROLLED ROD R-FACTORS (BUNDLE 3195, 20 GWD/ST).....	3-35
FIGURE 3-31. BUNDLE 3194 LATTICE 8860 K-INFINITY AT 40% VF.....	3-36
FIGURE 3-32. BUNDLE 3195 LATTICE 8864 K-INFINITY AT 40% VF.....	3-37
FIGURE 4-1. REFERENCE EQUILIBRIUM CORE FUEL TYPES AND QUANTITIES.....	4-11
FIGURE 4-2. HOT DESIGN EIGENVALUE VS. EXPOSURE	4-12

FIGURE 4-3. COLD DESIGN EIGENVALUE VS. EXPOSURE	4-13
FIGURE 4-4. ROD PATTERNS	4-14
FIGURE 4-5. SEQUENCE 1 CORE AVERAGE AXIAL POWER DISTRIBUTIONS	4-21
FIGURE 4-6. SEQUENCE 2 CORE AVERAGE AXIAL POWER DISTRIBUTIONS	4-22
FIGURE 4-7. SEQUENCE 3 CORE AVERAGE AXIAL POWER DISTRIBUTIONS	4-23
FIGURE 4-8. SEQUENCE 4 CORE AVERAGE AXIAL POWER DISTRIBUTIONS	4-24
FIGURE 4-9. SEQUENCE 5 CORE AVERAGE AXIAL POWER DISTRIBUTIONS	4-25
FIGURE 4-10. SEQUENCE 6 CORE AVERAGE AXIAL POWER DISTRIBUTIONS	4-26
FIGURE 4-11. SEQUENCE 1 CORE AVERAGE AXIAL EXPOSURE DISTRIBUTIONS	4-27
FIGURE 4-12. SEQUENCE 2 CORE AVERAGE AXIAL EXPOSURE DISTRIBUTIONS	4-28
FIGURE 4-13. SEQUENCE 3 CORE AVERAGE AXIAL EXPOSURE DISTRIBUTIONS	4-29
FIGURE 4-14. SEQUENCE 4 CORE AVERAGE AXIAL EXPOSURE DISTRIBUTIONS	4-30
FIGURE 4-15. SEQUENCE 5 CORE AVERAGE AXIAL EXPOSURE DISTRIBUTIONS	4-31
FIGURE 4-16. SEQUENCE 6 CORE AVERAGE AXIAL EXPOSURE DISTRIBUTIONS	4-32
FIGURE 4-17. HOT EIGENVALUE VS. CYCLE EXPOSURE	4-33
FIGURE 4-18. END OF CYCLE BUNDLE AVERAGE EXPOSURE (16.73 GWd/ST)	4-34
FIGURE 4-19. RADIAL PEAKING FACTOR VS. CYCLE EXPOSURE.....	4-35
FIGURE 4-20. BEGINNING OF SEQUENCE 1 INTEGRATED BUNDLE POWER (0.0 GWd/ST).....	4-36
FIGURE 4-21. END OF SEQUENCE 1 INTEGRATED BUNDLE POWER (3.0 GWd/ST).....	4-37
FIGURE 4-22. BEGINNING OF SEQUENCE 2 INTEGRATED BUNDLE POWER (3.0 GWd/ST).....	4-38
FIGURE 4-23. END OF SEQUENCE 2 INTEGRATED BUNDLE POWER (6.0 GWd/ST).....	4-39
FIGURE 4-24. BEGINNING OF SEQUENCE 3 INTEGRATED BUNDLE POWER (6.0 GWd/ST).....	4-40
FIGURE 4-25. END OF SEQUENCE 3 INTEGRATED BUNDLE POWER (9.0 MWD/ST)	4-41
FIGURE 4-26. BEGINNING OF SEQUENCE 4 INTEGRATED BUNDLE POWER (9.0 MWD/ST)	4-42
FIGURE 4-27. END OF SEQUENCE 4 INTEGRATED BUNDLE POWER (12.0 GWd/ST).....	4-43
FIGURE 4-28. BEGINNING OF SEQUENCE 5 INTEGRATED BUNDLE POWER (12.0 MWD/ST)	4-44
FIGURE 4-29. END OF SEQUENCE 5 INTEGRATED BUNDLE POWER (15.0 GWd/ST).....	4-45
FIGURE 4-30. BEGINNING OF SEQUENCE 6 INTEGRATED BUNDLE POWER (15.5 MWD/ST)	4-46
FIGURE 4-31. END OF SEQUENCE 6 INTEGRATED BUNDLE POWER (16.73 GWd/ST).....	4-47
FIGURE 4-32. MFLPD VS. CYCLE EXPOSURE.....	4-48
FIGURE 4-33. BEGINNING OF SEQUENCE 1 MFLPD (0.0 GWd/ST)	4-49
FIGURE 4-34. END OF SEQUENCE 1 MFLPD (3.0 GWd/ST)	4-50
FIGURE 4-35. BEGINNING OF SEQUENCE 2 MFLPD (3.0 GWd/ST)	4-51

FIGURE 4-36. END OF SEQUENCE 2 MFLPD (6.0 GWd/ST)	4-52
FIGURE 4-37. BEGINNING OF SEQUENCE 3 MFLPD (6.0 GWd/ST)	4-53
FIGURE 4-38. END OF SEQUENCE 3 MFLPD (9.0 MWD/ST).....	4-54
FIGURE 4-39. BEGINNING OF SEQUENCE 4 MFLPD (9.0 MWD/ST).....	4-55
FIGURE 4-40. END OF SEQUENCE 4 MFLPD (12.0 GWd/ST)	4-56
FIGURE 4-41. BEGINNING OF SEQUENCE 5 MFLPD (12.0 MWD/ST).....	4-57
FIGURE 4-42. END OF SEQUENCE 5 MFLPD (15.0 GWd/ST)	4-58
FIGURE 4-43. BEGINNING OF SEQUENCE 6 MFLPD (15.5 MWD/ST).....	4-59
FIGURE 4-44. END OF SEQUENCE 6 MFLPD (16.73 GWd/ST)	4-60
FIGURE 4-45. MCPR VS. CYCLE EXPOSURE.....	4-61
FIGURE 4-46. BEGINNING OF SEQUENCE 1 MCPR (0.0 GWd/ST)	4-62
FIGURE 4-47. END OF SEQUENCE 1 MCPR (3.0 GWd/ST).....	4-63
FIGURE 4-48. BEGINNING OF SEQUENCE 2 MCPR (3.0 GWd/ST)	4-64
FIGURE 4-49. END OF SEQUENCE 2 MCPR (6.0 GWd/ST).....	4-65
FIGURE 4-50. BEGINNING OF SEQUENCE 3 MCPR (6.0 GWd/ST)	4-66
FIGURE 4-51. END OF SEQUENCE 3 MCPR (9.0 MWD/ST).....	4-67
FIGURE 4-52. BEGINNING OF SEQUENCE 4 MCPR (9.0 GWd/ST)	4-68
FIGURE 4-53. END OF SEQUENCE 4 MCPR (12.0 GWd/ST).....	4-69
FIGURE 4-54. BEGINNING OF SEQUENCE 5 MCPR (12.0 GWd/ST)	4-70
FIGURE 4-55. END OF SEQUENCE 5 MCPR (15.0 GWd/ST).....	4-71
FIGURE 4-56. BEGINNING OF SEQUENCE 6 MCPR (15.5 GWd/ST)	4-72
FIGURE 4-57. END OF SEQUENCE 6 MCPR (16.73 GWd/ST).....	4-73
FIGURE 4-58. HOT EXCESS REACTIVITY VS. CYCLE EXPOSURE	4-74
FIGURE 4-59. HYDRAULIC CONTROL UNIT ASSIGNMENTS	4-75
FIGURE 4-60. COLD SHUTDOWN MARGIN VS. CYCLE EXPOSURE	4-76
FIGURE 4-61. CONTROL ROD WORTH COMPARISONS AT BOC (0.00 GWd/ST).....	4-77
FIGURE 4-62. CONTROL ROD WORTH COMPARISONS AT MOC (8.00 GWd/ST).....	4-78
FIGURE 4-63. CONTROL ROD WORTH COMPARISONS AT EOC (16.73 GWd/ST).....	4-79
FIGURE 4-64. COLD SHUTDOWN MARGIN DISTRIBUTION (%) AT BOC (0.0 GWd/ST).....	4-80
FIGURE 4-65. COLD SHUTDOWN MARGIN DISTRIBUTION (%) AT MOC (8.0 GWd/ST).....	4-81
FIGURE 4-66. COLD SHUTDOWN MARGIN DISTRIBUTION (%) AT EOC (16.73 GWd/ST).....	4-82
FIGURE 4-67. STANDBY LIQUID CONTROL MARGIN VS. CYCLE EXPOSURE.....	4-83
FIGURE 4-68. EIGENVALUES VS. MODERATOR TEMPERATURE (FOR MTC/ZERO XENON).....	4-84

FIGURE 4-69. MODERATOR TEMPERATURE COEFFICIENT WITHOUT XENON..... 4-85
FIGURE 4-70. EIGENVALUES VS. MODERATOR TEMPERATURE (FOR MVC/ZERO XENON) 4-86
FIGURE 4-71. MODERATOR VOID COEFFICIENT WITHOUT XENON..... 4-87
FIGURE 4-72. EIGENVALUES VS. MODERATOR TEMPERATURE (FOR MTC/XENON) 4-88
FIGURE 4-73. MODERATOR TEMPERATURE COEFFICIENT WITH XENON 4-89
FIGURE 4-74. EIGENVALUES VS. MODERATOR TEMPERATURE (FOR MVC/XENON)..... 4-90
FIGURE 4-75. MODERATOR VOID COEFFICIENT WITH XENON 4-91
FIGURE 4-76. LOAD DROP – POWER VS. TIME..... 4-92
FIGURE 4-77. LOAD DROP – XENON WORTH VS. TIME..... 4-92
FIGURE 4-78. LOAD DROP – POWER VS. TIME 4-93
FIGURE 4-79. SCRAM RECOVERY – POWER VS. TIME 4-93
FIGURE 4-80. SCRAM RECOVERY – XENON WORTH..... 4-94
FIGURE 4-81. SCRAM RECOVERY – AXIAL POWER SHAPE..... 4-94

ABSTRACT

In this report, the nuclear design of the ESBWR reference equilibrium core with the GE14E fuel type is presented along with a detailed discussion of the nuclear physics methods applied to the design. This report is based on a collection of work performed by various technical authors at GNF/GEH over the past five years. Key contributions in the area of nuclear methods and core and bundle design have been made by William Russell, Lukas Trosman, John Elam, James Smith, Atul Karve and many others.

Section 1 provides details about the nuclear methods of an ESBWR, including lattice physics techniques, lattice physics methods qualification, the three-dimensional nuclear model, the thermal-hydraulics model, three dimensional simulator model qualification, and reactivity coefficient methods. Section 2 provides design basis information. Negative feedback bases, shutdown margins, overpower bases, standby liquid control system, and stability bases are described. Section 3 provides descriptions and detailed data on two GE14E bundle designs that have been utilized in an equilibrium cycle evaluation. Detailed data includes axial k-infinity and local peaking for each lattice, enrichment distributions, rod types, R-factors, etc. Finally, Section 4 provides detailed analysis results from PANACEA, a 3-D BWR simulator code. Results include reactivity margins (hot excess and cold shutdown), thermal margins (2-D MCPR and MFLPD) and 2-D bundle power distributions based on a detailed rodded depletion analysis, core average axial power and exposure distributions at analysis state points through the cycle, etc., for a GE14E equilibrium cycle core loading pattern. This document contains over one hundred tables and figures in order to aid in the understanding of the ESBWR nuclear design with GE14E fuel.

Acronyms and Abbreviations

Acronym	Definition
ALPHGR	Average Planar Linear Heat Generation Rate
AOO	Anticipated Operational Occurrences
ARI	All Rods In
ASME	American Society of Mechanical Engineering
BOC	Beginning of Operating Cycle
BOL	Beginning of Life
BWR	Boiling Water Reactor
CPR	Critical Power Ratio
EFPD	Effective Full Power Days
ENDF	Evaluated Nuclear Data File
EOC	End of Operating Cycle
GDC	General Design Criteria
GETAB	General Electric Thermal Analysis Basis
IR	Intermediate Resonance
LHGR	Linear Heat Generation Rate
MAPLHGR	Maximum Average Planar Linear Heat Generation Rate
MAPRAT	Ratio of ALPHGR to MAPLHGR
MeV	Million Electron Volts
MFCLPR	Maximum Fraction of Limiting Critical Power Ratio
MFLPD	Maximum Fraction of Limiting Power Density
MLHGR	Maximum Linear Heat Generation Rate
MOC	Middle of Operating Cycle
MTC	Moderator Temperature Coefficient
MVC	Moderator Void Coefficient
OLMCPR	Operating Limit Minimum Critical Power Ratio
OLTP	Operating Licensed Thermal Power
RLP	Reference Loading Pattern
SLCS	Standby Liquid Control System
TIP	Traveling In-core Probe
TPFM	Two Phase Friction Multiplier

1. NUCLEAR METHODS

1.1 INTRODUCTION

The ESBWR core design is performed using the analytical tools and methods that are used for the steady-state nuclear evaluations of all General Electric BWR cores. These nuclear physics methods, described and approved for application to current BWR cores in References 6 and 7, are described in detail in this section. These nuclear physics methods have proven their abilities and capabilities over hundreds of reactor operating years. The nuclear evaluation procedure for both ESBWR and standard BWRs is best addressed as two parts: lattice analysis and core analysis.

Due to the differences in bundle design, control state, void condition and accumulated exposure, bundle nuclear properties in a core are non-uniform both in transverse and axial directions. As a result, the neutron behavior in each axial segment of a bundle is determined not only by the nuclear properties of that segment but also by the nuclear properties of adjacent segments of that bundle and neighboring bundles. The calculation of the influence of neighboring bundles is very complex because each bundle can conceivably undergo a wide spectrum of environments, depending on its location and core operating history. Fortunately, this influence is generally minor because of the effects of the solid (non-voided) water in the bypass region outside of the channel. An approximate way to model the bundle, therefore, is to account for the influence of neighboring bundles in the core simulator and to generate homogenized cross sections by assuming that the bundle is located in an infinite, periodic lattice along the transverse directions and is uniform and infinitely long along the axial direction.

As a result of the preceding approximation, a bundle can be simulated as an “isolated” two-dimensional heterogeneous system that may comprise fuel rods, water rods, burnable poison (gadolinia), in-channel water, channel, out-of-channel water, and the control rod (Figure 1-1). Again, due to the complexity of the system, it is not economically feasible to model a whole bundle by using transport theory methods alone. The bundle modeling is therefore further divided into two stages: (1) the fuel rod cell and external region modeling by using transport theory methods, and (2) the coarse-mesh bundle modeling based on cell homogenization and diffusion theory methods.

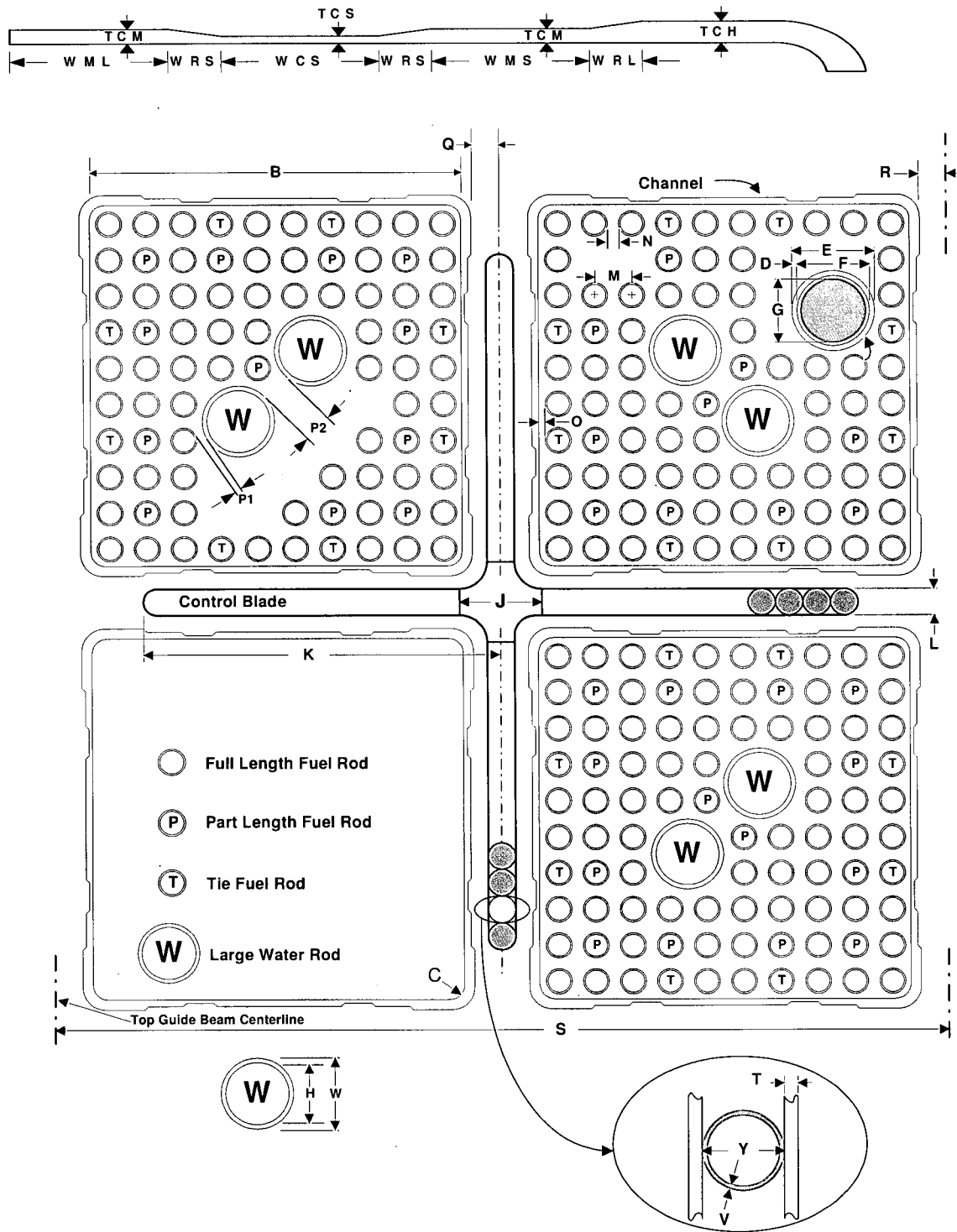


Figure 1-1. Typical Bundle Configuration

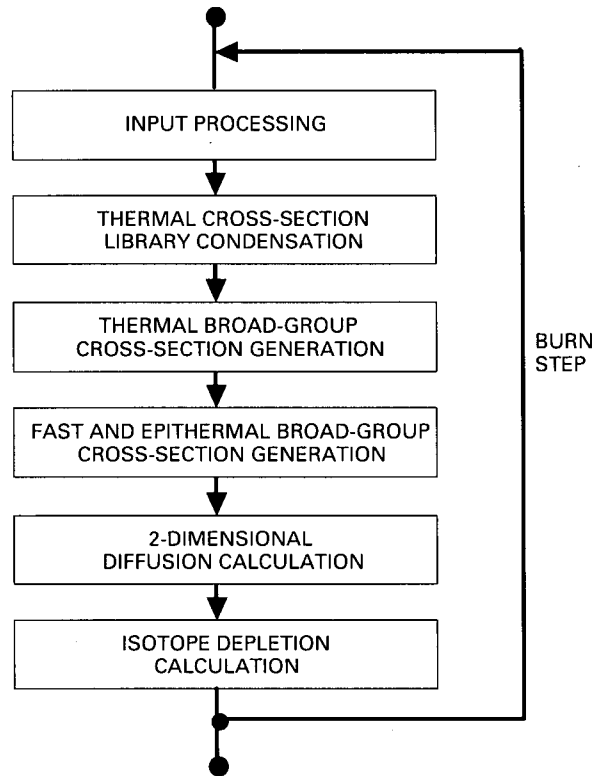


Figure 1-2. Lattice Physics Code Flow Diagram

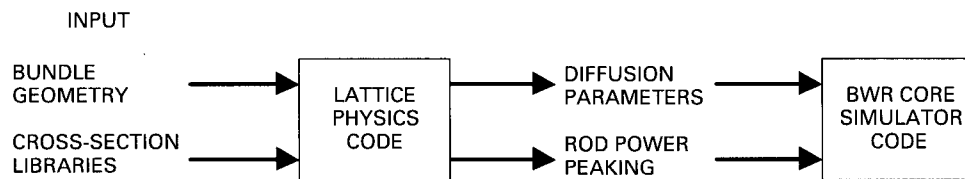


Figure 1-3. Flow Diagram for the Lattice Physics/BWR Core Simulator System

1.2 GENERAL DESCRIPTION OF LATTICE PHYSICS SOLUTION TECHNIQUES

The source for all neutron cross sections used by the lattice physics code is the Evaluated Nuclear Data File, ENDF/B. The cross sections for the principal heavy nuclides (U^{235} , U^{238} , Pu^{239} , etc.) and gadolinium isotopes (Gd^{154} , Gd^{155} , Gd^{157} , etc.) were obtained from ENDF/B-V, while all the other cross sections were obtained from either ENDF/B-IV or ENDF/B-V. In either case, the ENDF/B data must be collapsed to obtain multi-group cross sections, single-level Breit-Wigner resonance parameters, and scattering matrices. In the collapsing process, a spectrum representative of the BWR operating environment is used in the thermal energy range (below 0.785 eV), a $1/E$ spectrum in the resonance range (between 0.785 eV and 7 keV), and a Watt fission spectrum (based on ENDF/B-V) in the fission energy range. The thermal energy range is divided into 30 energy groups (as shown in Table 1-1) and the epithermal range is divided into 68 equal-lethargy intervals with a maximum neutron energy of 10.0 MeV.

A description of the calculations performed by the lattice physics code is provided in detail in the following sections and is represented in general terms in Figure 1-2. The lattice physics code provides lattice-averaged diffusion cross-sections, relative rod power peaking, and lattice edge discontinuity factors for the BWR simulator core calculations. A flow diagram for the lattice physics/BWR core simulator system is given in Figure 1-3.

The solution techniques begin with the generation of thermal broad-group neutron cross-sections for all homogenized fuel rod cells and external regions in a bundle. In the thermal energy range, the rod-by-rod thermal spectra are calculated by a method similar to the THERMOS [Reference 1] formulation. The major difference is that neutron leakage from rod to rod is taken into account. The leakage is determined by diffusion theory and is fed into the thermal spectrum calculation. Iterations between diffusion theory and collision probability thermal spectrum calculations are carried out to determine accurate, spatially dependent, thermal energy range cross sections.

The second step is to generate the cell- and region-homogenized cross sections for the fast and epithermal broad groups. In the epithermal and fast energy range, the level-wise resonance integrals are calculated by an improved intermediate resonance (IR) approximation in which the IR parameters are fuel-rod-temperature dependent. This temperature dependence is omitted in the conventional IR approximations. In addition, the fuel rod escape probability is calculated according to an improved treatment by Mizuta [Reference 2].

The third step utilizes the cross sections generated in steps one and two in a two-dimensional, coarse-mesh, broad-group, diffusion-theory calculation to determine the nodal flux and power distributions in the bundle. Intra-region flux information from steps 1 and 2 is combined with the cell average flux information to construct a detailed flux distribution within each region.

The fourth and final step is to perform the nuclide depletion calculation. In the depletion calculation, 100 nuclides are treated, including 25 fissile and fertile nuclides and up to 48 fission products plus one pseudo fission product and one gadolinium tail pseudo product. An improved burnup integration scheme is employed in nuclide depletion calculations.

The preceding steps are repeated for each burn step until all given burn steps are completed.

1.2.1 Thermal Neutron Spectrum and Diffusion Parameter Calculations

In this section, the generation of thermal cross sections and diffusion coefficients is discussed. This process includes the condensation of the thermal cross-section library from 30 groups to 16 groups, the calculation of leakage-dependent region-wise neutron spectrum, and the generation of thermal homogenized leakage dependent diffusion parameters.

1.2.1.1 Thermal Library Condensation

The conventional library for thermal spectrum calculations is composed of 30-group thermal cross sections. A properly condensed 16-group (group structure is shown in Table 1-1), rather than a 30-group thermal library, is adequate to calculate the thermal spectrum correctly.

The fluxes for the condensation of the cross sections from 30 to 16 groups are calculated by using the THERMOS method for the averaged regular and the averaged gadolinia (Gd) fuel rod cells. Each averaged cell is assumed to have two regions (fuel region and cladding-moderator homogenized region) in the radial direction and to be infinitely long in the axial direction.

1.2.1.2 Thermal Neutron Spectrum Calculation

The integral transport theory method has been widely utilized for calculating thermal neutron spectra in reactor lattices. The THERMOS computer code (based on this method) was introduced by Honeck in 1961. The integral transport method has continued to be used along with two improvements: (1) the collision probability is calculated more accurately, and (2) the reflecting boundary condition is generalized to the albedo (or leakage-dependent) boundary condition.

1.2.1.3 Integral Transport Theory

Following the Wigner-Seitz cell approximation, each fuel rod and its surrounding cladding and moderator are represented by an equivalent cylindrical cell as shown in Figure 1-4.

Table 1-1. Group Structure of Thermal Library

16-Group	30-Group	Upper Boundaries		
		Velocity, v (Units of 2200 m/sec)	Lethargy, $u(u = 0$ at 10 MeV)	E (eV)
1	1	[[
	2			
	3			
	4			
2	5			
	6			
	7			
	8			
3	9			
	10			
	11			
	12			
4	13			
	14			
	15			
	16			
5	17			
	18			
	19			
	20			
6	21			
	22			
	23			
	24			
7	25			
	26			
	27			
	28			
8	29			
	30			
	31			
	32			
9	33			
	34			
	35			
	36			
10	37			
	38			
	39			
	40			
11	41			
	42			
	43			
	44			
12	45			
	46			
	47			
	48			
13	49			
	50			
	51			
	52			

16-Group	30-Group	Upper Boundaries		
		Velocity, v (Units of 2200 m/sec)	Lethargy, $u(u = 0$ at 10 MeV)	E (eV)
14	28			
15	29			
16	30]]

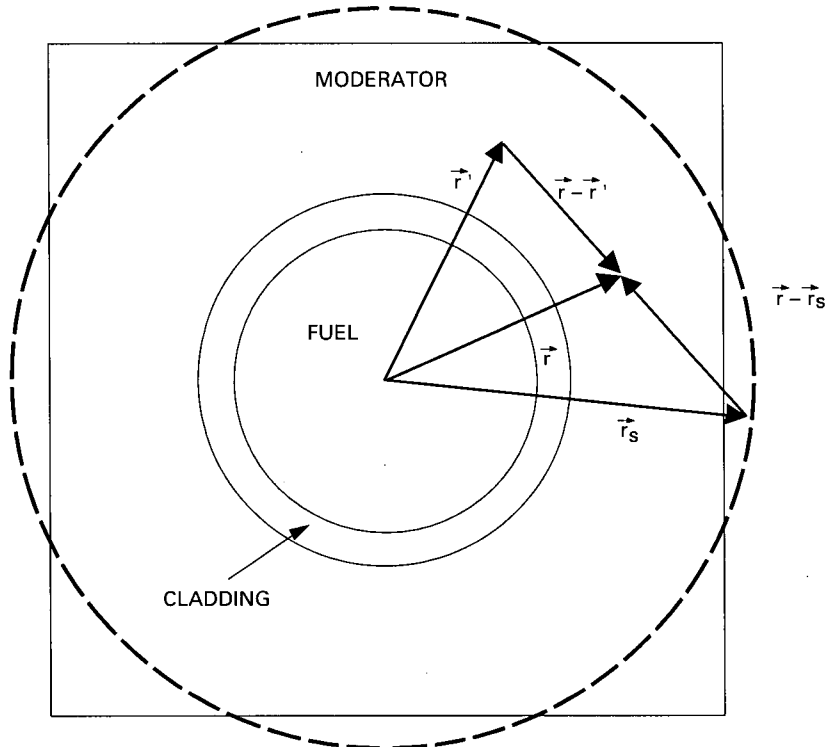


Figure 1-4. An Equivalent Fuel Cell

The integral transport form of the neutron balance equation with isotropic scattering and source in a unit cell is given by:

$$\Sigma_T(\vec{r}, E)\phi(\vec{r}, E) = \int_V dV' P(\vec{r}' \rightarrow \vec{r}, E) \left\{ \int_0^{E_c} dE' \Sigma_s(\vec{r}', E' \rightarrow E)\phi(\vec{r}', E') + Q(\vec{r}', E) \right\} + \int_S dS \hat{n} \cdot \vec{x}(\vec{r}_s, \hat{\Omega}_s, E) P(\vec{r}_s \rightarrow \vec{r}, E) \quad (1.2.1)$$

where:

$$P(\vec{r}' \rightarrow \vec{r}, E) = \frac{\Sigma(\vec{r}, E)}{4\pi|\vec{r}-\vec{r}'|^2} \exp \left[- \int_0^{|\vec{r}-\vec{r}'|} \Sigma \left(\vec{r}-R', \frac{(\vec{r}-\vec{r}')}{|\vec{r}-\vec{r}'|} \right) dR' \right].$$

Here:

- $\Sigma_s(\vec{r}, E' \rightarrow E)$ = the scattering kernel,
- $Q(\vec{r}, E)$ = the slowing-down source,
- $P(\vec{r}' \rightarrow \vec{r}, E)$ or $P(\vec{r}_s \rightarrow \vec{r}, E)$ = the transport kernel,

$\vec{J}_- (\vec{r}_s, \hat{\Omega}_s, E)$ = the incoming surface current,

\vec{r} = the position vector inside the cell,

\vec{r}_s = the position vector on the boundary surface,

E_C = the upper thermal cutoff energy,

$\hat{\Omega}_s$ = $(\vec{r} - \vec{r}_s) / |\vec{r} - \vec{r}_s|$, and

\hat{n} = the outward normal direction of boundary surface

Physically, the left-hand side of Equation (1.2.1) is the collision removal term for neutrons with energy E at position \vec{r} , the first term on the right-hand side is the corresponding source term from all other parts inside the cell, and the second term on the right-hand side represents the surface source term.

The cell is divided into sub-regions composed of constant cross-sections, then integrated over the volume element V_n with the assumption of isotropic incoming surface current. The conventional flat flux and flat source approximation is then applied and the result is discretized into the multi-group form. The incoming partial current \vec{J}_- is expressed in terms of the net cell leakage and the surface-to-surface transport probability.

1.2.1.4 Surface Leakage

To solve the multi-group integral transport equation presented in the previous subsection, the group-dependent albedo boundary conditions (α_g) need to be specified. A technique called the L-method (L represents surface leakage) is used to evaluate the albedo α_g because the net surface leakage L_g is related to α_g by:

$$L_g = (J_g^- - J_g^+)S = (\alpha_g - 1)S J_g^+$$

where J_g^- and J_g^+ are incoming and outgoing surface partial current densities, and S is the cell surface area.

In the L-method, the g^{th} group net boundary-surface leakage L_g is assumed to be proportional to the cell absorption of that group:

$$L_g \propto A_g = \int_{\text{cell}} \Sigma_{ag}(\vec{r}) \phi_g(\vec{r}) dV$$

or

$$L_g = \frac{L}{A} A_g, \quad g = 1, 2, \dots, G$$

where:

$$L = \sum_{g=1}^G L_g; A = \sum_{g=1}^G A_g.$$

The cell total thermal leakage, which equals the cell slowing-down source minus cell total thermal absorption, can be evaluated from a broad-thermal-group bundle diffusion calculation with slowing-down sources. However, the broad-thermal-group cross sections for the bundle diffusion calculation are generated from the fine-group flux-weighted collapsing expressions, and the fine-group fluxes can only be obtained by solving the cell integral transport equations with leakage boundary conditions. As a result, the individual cell fine-thermal-group transport calculations and the bundle broad-thermal-group diffusion calculation depend on each other because of the thermal leakage coupling.

To account for this thermal leakage coupling, the broad-thermal-group cross sections are assumed to be a function of the cell total thermal leakage L as:

$$\Sigma(L) = \Sigma_0 + \frac{aL}{b+L}, \quad (1.2.2)$$

where Σ_0 , a, and b are the L-fitting parameters. We note that $\Sigma(0) = \Sigma_0$ and $\Sigma(\infty) = \Sigma_0 + a$. The three L-fitting parameters can be determined by repeating the L-dependent THERMOS calculations for three different assumed L-values in the neighborhood of the actual L-value. The actual L-value for each cell region is determined by means of the L-iterations in the bundle broad-thermal-group diffusion calculation, until the L-dependent cross section $\Sigma(L)$ is converged.

1.2.1.5 Thermal Homogenized Cross Section and Diffusion Coefficient Generation

The homogenized cross sections are formulated by preserving region-wise, thermal reaction rates as:

$$\sum_x^j = \frac{\sum_{i,j,k,g} N_i^{j,k} \sigma_{x,g}^{i,j,k} \phi_g^{j,k} \Delta v_g V_k}{\sum_{k,g} \phi_g^{j,k} \Delta v_g V_k}, \quad x = T, tr, f, a \quad (1.2.3)$$

where:

- $N_i^{j,k}$ = atom density of i^{th} isotope in k^{th} subregion of j^{th} region,
- V_k = k^{th} volume element,
- g = g^{th} fine group,
- Δv_g = g^{th} group speed interval, and
- x = type of reaction – total (T), transport (tr), fission (f), or absorption (a).

The homogenized diffusion coefficients are expressed in terms of the transport cross-sections and are determined first by energy group condensation:

$$\Sigma_{tr}^{j,k} = \frac{\sum_g \phi_g^{j,k} \Delta v_g}{\sum_g \phi_g^{j,k} \Delta v_g / \Sigma_{tr,g}^{j,k}} \quad (1.2.4)$$

then by spatial summation:

$$D_j = \frac{\sum_k \phi_{jk} V_k}{3 \sum_k \Sigma_{tr}^{j,k} \phi_{j,k} V_k} \quad (1.2.5)$$

where:

$$\phi_{jk} = \sum_g \phi_g^{j,k} \Delta v_g.$$

The preceding expressions for the homogenized thermal diffusion parameters cannot be used for control blades, which are composed of strong absorption material. The control blade regions are treated similarly but utilizing a P1 blackness model.

1.2.2 Fast and Epi-thermal Spectrum and Diffusion Parameter Calculations

This section presents a discussion of the generation of fast and epithermal cross-sections and diffusion coefficients. This process includes the consideration of Dancoff factors, the calculation of resonance cross sections, the determination of heterogeneity correction factors from averaged-fuel-rod-cell transport calculation and the fine-group transport calculation for a one-dimensional equivalent bundle.

1.2.2.1 Dancoff Factor Calculation

In 1944, Dancoff and Ginsburg first analyzed the shadowing effect on incident neutrons to a fuel rod due to the block of neighboring rods, and calculated the shadowing factors subsequently known as the Dancoff factors. Dancoff factors play an important role in calculating the effective resonance cross-sections and the heterogeneity effect in the fast and epithermal energy regions. They are particularly important for BWR lattices because of the presence of the channel box and the water gap, and the non-uniformity of the water density due to the un-voided water outside the channel box and inside the water rods. This causes the resonance integrals to vary from rod to rod in the lattice and the variation is taken into account through the use of a rod-dependent Dancoff factor, together with a rod-dependent atomic concentration of the resonant nuclide.

In the formulation of the Dancoff factor, the following assumptions were made:

- (1) The fuel rods are black to neutrons in the resonance energy range (i.e., they absorb all incident resonance neutrons).

- (2) The source distribution of resonance neutrons in the moderator is isotropic and spatially constant.
- (3) Each resonance is narrow such that any collision in the moderator removes the neutron from that resonance interval.

The Dancoff factor of a given rod is defined as the probability that a resonance neutron (produced by slowing down from a fission neutron) in the moderator is shielded from the rod by neighboring rods in the lattice. The factors are calculated for each individual fuel rod and include the effects of the fuel rod cladding. The average value of the Dancoff factor for a fuel bundle is simply the arithmetic average of the Dancoff factors for the individual fuel rods.

1.2.2.2 Resolved Resonance Treatment

The resonance absorption of heavy nuclides, especially U^{238} , is a major factor in determining the neutron multiplication factor of a light water reactor. The resonance cross sections are calculated using an improved intermediate resonance (IR) approximation by Mizuta [Reference 3], and using a fine energy mesh model for certain resonance levels for certain isotopes as specified by the user. The improvements include: (1) temperature dependence of the IR parameters; (2) interference between the potential scattering and the resonance scattering; and (3) improved A-factor in the Wigner rational approximation for the fuel escape probability. The fine energy mesh model solves the Chernick equation in a heterogeneous (3 regions) model near the resonance of interest. This model is used for the Pu^{240} 1.056 eV resonance and optionally for other U^{238} resonances.

1.2.2.3 Unresolved Resonance Treatment

The average neutron energy decrement per collision is much larger than the average level spacing in the unresolved resonance region; therefore, narrow resonance approximation is applied for unresolved resonance treatment. Moreover, since the neighboring resonance peaks are unresolved with each other, the reduced neutron widths are assumed to distribute according to the Porter-Thomas distribution:

$$P(y) = \frac{e^{-y/2}}{\sqrt{2\pi y}},$$

where y is the ratio of each individual reduced width to the average reduced width.

1.2.2.4 Determination of Heterogeneity Correlation Factors from Averaged Fuel-Rod-Cell Transport Calculation

In the fast and epithermal energy range, the flux distribution is quite flat and near-periodic across various fuel-rod-cell regions inside a fuel bundle because the total neutron mean-free-path is much longer than a single fuel-cell pitch. Hence, the flux variation inside each fuel-rod cell is approximately represented by the flux variation obtained from an averaged fuel-rod-cell transport calculation. The fast and epithermal spatial and the fast spectrum heterogeneity factors can then be determined from the flux solution of the averaged fuel-rod-cell transport calculation.

1.2.2.5 Fine-Group Transport Calculation for a One-Dimensional Equivalent Bundle

The neutron spectrum in various regions of the fuel bundle is required for condensing and homogenizing the fine-group cross sections as described in the thermal energy range. In the fast and epithermal range, the neutron spectrum in the two-dimensional bundle is approximated by the spectrum obtained from a one-dimensional equivalent bundle transport calculation.

The one-dimensional equivalent bundle is established by preserving the hydrogen-to-uranium atom ratio (H/U) of the actual bundle, because the fast and epithermal spectrum is very sensitive to H/U. [[

- 1.
- 2.
- 3.
- 4.
- 5.
- 6.
- 7.
- 8.
- 9.
- 10.
11.]]

The approximate two dimensional to one-dimensional geometric relationship can be seen in Figure 1-5.

[[

]]

Figure 1-5 Geometric Relationship Between the One-Dimensional Equivalent and the Actual Bundles

1.2.2.6 Diffusion-Transport Correlation Factor Calculation

The fast and epithermal homogenized diffusion cross sections are to be determined by preserving the transport removal reaction rates in terms of region-wise, group-dependent, diffusion-transport correction factors. The diffusion-transport correction factors are defined as the ratios of transport removal and diffusion removal reaction rates in each of the spectrum regions of the preceding one-dimensional equivalent bundle:

$$f_{L,G}^{DT} \equiv \frac{G^{\text{th}} \text{ group transport removal rate in } L^{\text{th}} \text{ spectrum region}}{G^{\text{th}} \text{ group diffusion removal rate in } L^{\text{th}} \text{ spectrum region}}$$

Here, the broad-group transport removal rates are evaluated from the fine-group fluxes, removal cross-sections, and region-volumes of one-dimensional bundle transport calculations. The fast and epithermal diffusion removal rates are evaluated from the broad-group fluxes, removal cross-sections and region-volumes of two-dimensional bundle diffusion calculations.

Although the resonance cross sections used in the one-dimensional transport and the two-dimensional diffusion calculations are obtained based on averaged atom density and Dancoff factor, the preceding diffusion-transport correction factors are used as transport-correction factors to rod-by-rod, density- and Dancoff-factor-corrected (absorption, fission, production, and slowing-down) cross sections for the few-group bundle diffusion calculation to be described in the next section. However, there are no transport corrections to the fast and epithermal diffusion coefficients.

1.2.3 Bundle Flux, Power, and Miscellaneous Calculations

This section describes the methods for calculating the neutron flux distributions, the power-related distributions and the bundle-averaged diffusion parameters. Three broad-energy groups are used for these bundle calculations. The first group spans the fast energy range from [[]], and includes all neutrons born in fission. The second group spans the resonance energy range from [[]]. The third group is the thermal group that includes all neutrons with energies below [[]].

1.2.3.1 Two-Dimensional Few-Group Coarse-Mesh Diffusion Calculation

To prepare for the coarse-mesh diffusion calculation, the following assumptions are made to represent the fuel bundle:

- (1) Each fuel rod (including water rod, plenum rod, and vanished rod cells) and its surrounding moderator are replaced by a homogenized cell region, and are represented by one node located at the center of that region.
- (2) The round corners of the channel box are replaced by the equivalent rectangular corners.
- (3) The channel box and water film are homogenized together as one material type in external regions.

1.2.3.2 Nodal Diffusion Equations

The two-dimensional few-group diffusion equations for the bundle flux calculations are given by:

$$\begin{aligned}
 & -\frac{\partial}{\partial x} D_g(x, y) \frac{\partial}{\partial x} \phi_g(x, y) - \frac{\partial}{\partial y} D_g \frac{\partial}{\partial y} \phi_g + \Sigma_{Rg}(x, y) \phi_g = \\
 & \frac{1}{k} \chi_g \sum_{g'=1}^G \nu_{g'} \Sigma_{fg'}(x, y) \phi_{g'} + \sum_{g'=1}^{g-1} \Sigma_{S, g'g}(x, y) \phi_{g'}, \quad g = 1, \dots, G
 \end{aligned} \tag{1.2.6}$$

where all notations are standard, and no up-scattering is assumed. Since each region is homogenized, the nuclear parameters in that region are represented by their homogenized (constant) values; that is,

$$D_g(x, y) = D_g^{i,j}, \Sigma_{Rg}(x, y) = \Sigma_{R,g}^{i,j}, \Sigma_{fg}(x, y) = \Sigma_{fg}^{i,j},$$

and

$$\Sigma_{S, g'g}(x, y) = \Sigma_{S, g'g}^{i,j} \text{ in the region confined by } x_{i+1/2} > x > x_{i-1/2}$$

and

$$y_{j+1/2} > y > y_{j-1/2},$$

as show in Figure 1-6.

Equation (1.2.6) is transformed to the finite difference equation, and then solved by using the successive over-relaxation iterative method.

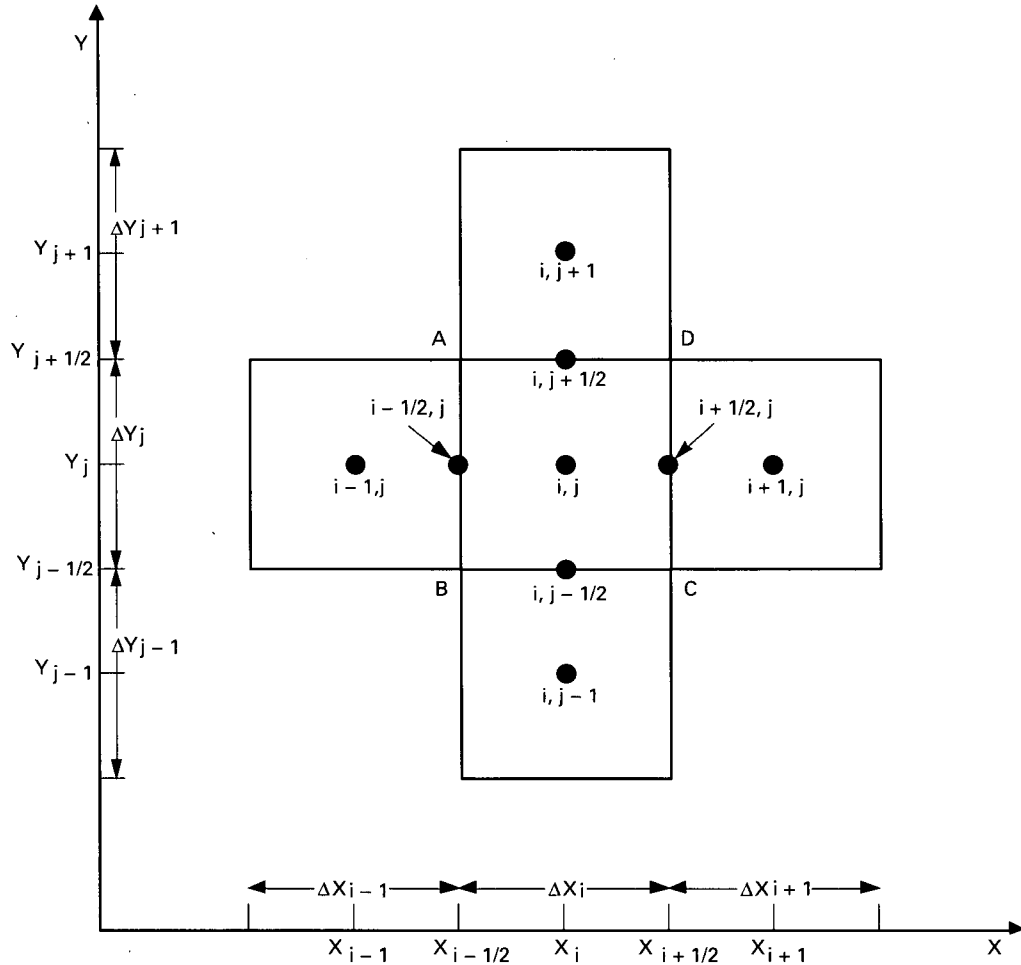


Figure 1-6. Typical Mesh Point and Its Nearest Neighbors

1.2.3.2.1 Boundary Conditions

The external boundary conditions used in most design calculations are the reflecting or zero-current boundary conditions:

$$\frac{\partial \phi_g(x, y^s)}{\partial x} = 0 \text{ and } \frac{\partial \phi_g(x^s, y)}{\partial y} = 0, g = 1, 2, \dots, G$$

where $x=x^s$ and $y=y^s$ are the boundary plane surfaces that bisect the water gaps and control blades between fuel bundles. These reflecting boundary conditions result from the assumption that the core is composed of an infinite repeating array of symmetric fuel bundles. In most cases, this approximation is adequate due to the fact that a BWR lattice is a very large system composed of near-periodic, symmetric fuel bundles, and that the water gaps in a BWR lattice tend to decouple the neutron spectra of adjacent bundles.

1.2.3.3 Power-Related Distributions

1.2.3.3.1 Fission Density Distribution

The fission density of each rod is calculated from the neutron fluxes as:

$$F_n = V_r \sum_{g=1}^G \sum_{j=1}^J \sum_{fj, g}^{(n)} \phi_g^{(n)}, n = 1, 2, \dots, N \quad (1.2.7)$$

where

- V_r = volume of the fuel region
- $\sum_{fj, g}^{(n)}$ = g^{th} group fission cross section for the j^{th} isotope in the n^{th} rod;
- J = total number of fissionable nuclides; and
- N = total number of fission-producing rods.

Dividing F_n by the average fission density \bar{F} yields the relative rod fission density \tilde{F}_n :

$$\tilde{F}_n = \frac{F_n}{\bar{F}} = \frac{F_n}{\frac{1}{N} \sum_{n=1}^N F_n}, n = 1, 2, \dots, N.$$

1.2.3.3.2 Power Distribution

The relative fission-density distribution is sometimes taken approximately as the relative thermal power distribution. However, the actual relative power distribution is different from the relative fission-density distribution because:

- (1) Different fissionable nuclides yield somewhat different amounts of energy per fission.

- (2) A fraction of the fission energy is released in the form of gamma rays, which have long mean-free-paths inside a reactor lattice and, therefore, their energy is often deposited far from their original source. This has the effect of spreading the thermal energy inside the lattice and consequently reducing the power peaking.
- (3) Neutron capture results in the release of gamma rays, which lose their energy in the same way as the fission gamma rays.

The fission-energy sources can be separated into two types based on their properties. One is the locally deposited fission energy, which is the kinetic energy of various short-ranged particles including fission fragments, fission neutrons and betas, and the other is the long-ranged gamma ray energy. The locally deposited power P_{Ln} in the n^{th} rod is given by:

$$P_{Ln} = V_n \sum_{g=1}^G \sum_{j=1}^J E_{Lj} \Sigma_{fj,g}^{(n)} \phi_g^{(n)} \quad (1.2.8)$$

where E_{Lj} is the locally deposited energy per fission (obtained from ENDF/B-V) for j^{th} fissionable isotope. Similarly, the local source of gamma ray energy $S_{\gamma n}$ is given by:

$$S_{\gamma n} = V_n \sum_{g=1}^G \sum_{j=1}^J \left(E_{\gamma fj} \Sigma_{fj,g}^{(n)} + E_{\gamma cj} \Sigma_{cj,g}^{(n)} \right) \phi_g^{(n)}, \quad (1.2.9)$$

where $E_{\gamma fj}$ and $E_{\gamma cj}$ are the energy released by the fission gammas and capture gammas of the j^{th} isotope.

The eight-group gamma number sources are given by:

$$Q_{n,g'}^{\gamma} = V_n \sum_{g=1}^G \sum_{j=1}^J \left(E_{\gamma fj} \Sigma_{fj,g}^{(n)} \chi_{fj}^{gg'} + E_{\gamma cj} \Sigma_{cj,g}^{(n)} \chi_{cj}^{gg'} \right) \phi_g^{(n)} \quad g' = 1, 2, \dots, g \quad (1.2.10)$$

where $\chi_{fj}^{gg'}$ ($\chi_{cj}^{gg'}$) is the number of photons emitted in gamma-energy group g' per unit gamma energy (MeV) due to a fission (capture) occurring in neutron-energy group g of the j^{th} nuclide. The gamma energies are divided into groups with boundaries [[]]

A complex gamma transport calculation is required to obtain the smeared gamma energy distribution. Based on previous transport calculations, the smeared gamma power $P_{\gamma n}$ in the n^{th} rod can be approximately given by:

$$P_{\gamma n} = \bar{S}_{\gamma} + \beta (S_{\gamma n} - \bar{S}_{\gamma}) \quad (1.2.11)$$

where \bar{S}_{γ} is the average gamma source, and β is a constant depending on lattice size.

The total power P_{Tn} in the n^{th} rod is the sum of the locally deposited fission power and smeared gamma power:

$$P_{T_n} = P_{L_n} + P_{G_n} \quad (1.2.12)$$

Typical values for P_{L_n} and P_{G_n} are [[]]

The relative power \tilde{P}_{T_n} is given by:

$$\tilde{P}_{T_n} = \frac{P_{T_n}}{\frac{1}{N} \sum_{n=1}^N P_{T_n}} \quad (1.2.13)$$

1.2.3.3 R-Factor Distribution

The power distribution calculated in the preceding subsection is the local fission power distribution without considering the coolant heat exchange among neighboring rods. Since the water in the adjacent coolant channel rapidly mixes together, the heat is exchanged among neighboring rods. To account for this heat exchange, a weighted peaking factor called the R-factor is used to characterize the local thermal peaking pattern in the vicinity of a given rod for the calculation of coolant-smear power distribution. This R-factor is related to, but not necessarily equal to, the bundle R-factor since weightings may change for various correlations and the various lattices comprising a bundle must be appropriately weighted. The R-factor distribution calculated here is given as a lattice design guide.

[[]]

(1.2.14)

]]

1.2.3.4 Pellet Radial Power Distribution

The radial power distribution within a pellet is calculated for use in fuel rod temperature calculations. The fission density distribution is the sum of the fission reaction rates in the three broad energy groups, i.e.,

$$F(r) = \sum_{g=1}^3 F_g f_g(r)$$

where F_g is the total number of fissions in-group g per unit volume and $f_g(r)$ is a radial distribution function for group g . For the fast energy range (i.e., greater than $[[\quad]]$), $f_g(r)$ is assumed to be flat, or independent of radius. In the epithermal range, the radial direction is divided into ten equal volume radial rings and a generic distribution is used. This generic distribution is computed by Monte Carlo methods and is assumed to be independent of pellet composition. The thermal group distribution $f_g(r)$ is typically computed for ten equal volume radial rings by the THERMOS based integral transport method described in Section 1.2.1. The radial fission distribution is then fit to a polynomial form for use in fuel pellet temperature calculations.

1.2.3.4 Bundle-Averaged Diffusion Parameters

The group-wise bundle-averaged diffusion coefficients and cross sections are calculated by using the conventional flux-weighted expressions, which preserve the bundle reaction rates. These expressions are:

$$D_g = \left[\frac{\sum_j \phi_{jg} V_j / D_{jg}}{\sum_j \phi_{jg} V_j} \right]^{-1} \quad (1.2.15)$$

$$\Sigma_{xg} = \frac{\sum_j \Sigma_{xg}^j \phi_{jg} V_j}{\sum_j \phi_{jg} V_j}, \quad x=f, S, R; \quad g = 1, \dots, G.$$

where the summation of j is over the whole bundle. The bundle-averaged diffusion parameters are used in the core diffusion calculation.

1.2.4 Nuclide Depletion Calculation

The nuclide depletion calculation is discussed in this section. The process includes the introduction of fission-related nuclide chains and the formulation of nuclide depletion equations. The half-lives in Figure 1-7 and Figure 1-8 are obtained from the Table of Isotopes edited by Lederer and Shirley or ENDF-VI edited data. The fission fraction yields for 10 actinides based on ENDF-349 [Reference 4] is utilized to determine the fission product source.

1.2.4.1 Fission-related Nuclide Chains

There are two types of fission-related nuclide chains: (1) fissionable nuclide and (2) fission product. The relationship among various nuclides in these chains is important for calculating the production and destruction of major nuclides as functions of exposure in a nuclear reactor.

The fissionable nuclide chains are shown in Figure 1-7. The β -decay and radioactive capture (n- γ reaction) are two main reactions in these chains. The (n, 2n) reaction and α -decay also occur, but their contribution to the production and destruction is usually small.

Two fission product models are available within TGBLA. The base fission product model consists of 29 major fission products (fission products and their daughters with significant neutron absorption), two gadolinium product isotopes, one gadolinium tail product, 6 zero cross section transition isotopes, and one pseudo fission product representing the contribution from the other minor fission products. The expanded fission product model consists of 40 major fission products (fission products and their daughters with significant neutron absorption), two gadolinium tail isotopes, a gadolinium tail product, 5 zero cross section transition isotopes, and one pseudo fission product representing the contribution from the other minor fission products. The fission product chains are shown in Figure 1-8.

1.2.4.2 Nuclide Depletion in Fuel Rods

For nuclide depletion, each regular fuel rod is assigned a burn region and each Gd fuel rod is divided up into a maximum of 20 (normally 10) burn regions to track the gadolinium isotopes. In each burn region, the nuclide- depletion equations are:

$$\frac{d N_i(t)}{d t} = P_i(t) - L_i(t), \quad i=1, 2, \dots, I \quad (1.2.16)$$

where

$N_i(t)$ = nuclide density;

$P_i(t)$ = production rate;

$L_i(t)$ = loss rate; and subscript "i" represents a nuclide type.

Equation (1.2.16) is a set of coupled, first-order differential equations that governs the changes of nuclide densities with respect to time in a burn region.

[[

Figure 1-7. Fissionable Nuclide Chains

]]

[[

]]

Figure 1-8. Fission Product Nuclide Chains

The production rate of the i^{th} nuclide is the sum of its total yield from fissions of all fissionable nuclides, the neutron capture rate of its k^{th} precursor (which has the same atomic number but with a mass number one unit smaller), and the beta decay rate from its m^{th} precursor (which has the same mass number but with an atomic number one unit smaller):

$$P_i(t) = \sum_{j=1}^G Y_i^{(j)} N_j(t) \sum_{g=1}^G \sigma_{fg}^{(j)} \phi_g + N_k(t) \sum_{g=1}^G \sigma_{cg}^{(k)} \phi_g + \lambda_m N_m(t) \quad (1.2.17)$$

where $Y_i^{(j)}$ is the fission yield of the i^{th} nuclide due to the j^{th} fissionable nuclide, and λ_m is the decay constant of the m^{th} precursor. The loss rate of the i^{th} nuclide is the sum of its decay and absorption rates:

$$L_i(t) = N_i(t) \left[\lambda_i + \sum_{g=1}^G \sigma_{ag}^{(i)} \phi_g \right]. \quad (1.2.18)$$

Substituting Equations (1.2.17) and (1.2.18) into Equation (1.2.16) yields:

$$\begin{aligned} \frac{dN_i(t)}{dt} = & \lambda_m N_m(t) - \lambda_i N_i(t) + \sum_{j=1}^J Y_i^{(j)} N_j(t) \sum_{g=1}^G \sigma_{fg}^{(j)} \phi_g \\ & + \sum_{g=1}^G \left[\sigma_{cg}^{(k)} N_k(t) - \sigma_{ag}^{(i)} N_i(t) \right] \phi_g, \quad i=1, 2, \dots, I. \end{aligned} \quad (1.2.19)$$

which is a set of coupled, nonlinear, differential equations for nuclide depletion. These depletion equations are solved using the fourth-order Runge-Kutta-Gill numerical integration technique.

1.3 LATTICE PHYSICS METHODS QUALIFICATION

1.3.1 Monte Carlo Benchmark Comparison

Fundamental qualification of the lattice physics system was accomplished by performing neutron balance and relative fission density comparisons between Monte Carlo analysis results and lattice physics calculations for designs ranging from 7x7 to 10x10 including numerous design features (i.e. small water rods, large water rods, square water rods, part length rods, plenum rods, and water cross designs). The Monte Carlo calculation is based on the exact neutron transport method and serves as a benchmark for the lattice physics code.

The lattice physics qualification includes cycle tracking, and benchmarking versus Monte Carlo simulations. Over 160 separate lattice comparisons were performed versus Monte Carlo lattice calculations to ensure that performance is equally accurate over the entire application range of the code. Neutron multiplication, isotope specific reaction rates and the overall neutron balance were all subject to examination.

The lattice physics code was benchmarked against Monte Carlo simulations of the same lattice at zero exposure and by utilizing the isotopic content generated by the lattice physics method, an exposed lattice simulation is made. The MCNP Monte Carlo neutral particle transport code, with continuous energy cross sections generated from the latest ENDF/B-V libraries, was used for these studies. These benchmarks provide detailed comparisons of multiple physics parameters such as absorption rates, fission reaction rates, fission density distribution, regional fluxes, burnable absorber reaction rates and k-infinity of the lattice, just to name a few. A broad range of lattice characteristics were examined with these methods. This comparison effort was extensive and the results voluminous. The global results of the comparisons can, however, be presented in the form of k-infinity differences between the two codes. Figure 1-9 shows the deviation of k-infinity of TGBLA06 from the benchmark MCNP calculation for the same beginning of life lattice and state conditions. Figure 1-10 shows the deviation of k-infinity of TGBLA06 from the benchmark MCNP calculation for a simulation of lattices with three (3) different concentrations of Gadolinium as a function of exposure at 40% void fraction. [[

]]

[[

]]

**Figure 1-9. Comparison of K-infinities for Beginning-of-Life Lattices
(TGBLA06 vs. MCNP)**

[[

]]

**Figure 1-10. Comparison of K-infinities for Exposed Lattices
(TGBLA06 vs. MCNP)**

Table 1-2 and Table 1-3 shows comparisons of neutron balances between the Monte Carlo and lattice physics results at 0.40 void fraction for a 10x10 fuel lattice without vanished rods and a 10x10 fuel lattice with vanished rods. The isotopic neutron balances are represented by the normalized three-group neutron absorption and production rates where the total neutron absorption is normalized to one. The overall neutron balance is represented by the production total which is equivalent to the lattice multiplication factor (K_{inf}). The standard deviation (σ) of the multiplication factor from the Monte Carlo analysis is ~ 0.001 . [[

]]. The isotopic absorption and production comparisons also show good agreement. [[

]]

Table 1-4 and Table 1-5 provides a sample of relative rod fission density from the Monte Carlo and the lattice physics calculations for two lattices at 0.40 void fraction. The Monte Carlo standard deviation is approximately 1% for each rod. [[

]]

Table 1-2. Neutron Balance Comparisons between Monte Carlo and Lattice Physics								
10x10 Lattice without Vanished Rods at 40% Void Fraction								
Isotope	Absorption				Production			
	1	2	3	Total	1	2	3	Total
U234	[[
Delta								
U235								
Delta								
U238								
Delta								
Gd154								
Delta								
Gd155								
Delta								
Gd156								
Delta								
Gd157								
Delta								
Gd158								
Delta								
Gd160								
Delta								
H2O								
Delta								
O-fuel								
Delta								
Zr*								
Delta								
TOTAL								
Delta]]

* Zr production is N,2N reaction

Table 1-3. Neutron Balance Comparisons between Monte Carlo and Lattice Physics								
10x10 Lattice with Vanished Rods at 40% Void Fraction								
	Absorption				Production			
Isotope	1	2	3	Total	1	2	3	Total
U234	[[
Delta								
U235								
Delta								
U238								
Delta								
Gd154								
Delta								
Gd155								
Delta								
Gd156								
Delta								
Gd157								
Delta								
Gd158								
Delta								
Gd160								
Delta								
H2O								
Delta								
O-fuel								
Delta								
Zr*								
Delta								
TOTAL								
Delta]]

* Zr production is N,2N reaction

Table 1-5. 10x10 Lattice with Vanished rods at 0.40 Void Fraction

[[

									11

(MONTE CARLO standard deviation is about 1%)

Table 1-6. Summary of Relative Fission Density Comparison between Monte Carlo and Lattice Physics

Lattice Type	Fuel Rods (UO ₂ +Gad)	Water Rods	Vanished Rods	Plenum Rods	00 VF	40VF	70VF
[[
]]
Samples	1240	Overall Weighted Average			[[]]		

- Notes:
1. Lattice is Water cross design.
 2. Lattice is Water box design.
 3. Lattice contains vanished or plenums rods on periphery.

The overall agreement between TGBLA06 and MCNP for various lattice state conditions is shown in Figure 1-11. The cases are grouped into categories such as “all” for all cases taken together, “cold” for the 20°C cases, “0 void” for the hot, 0% in-channel void fraction cases, etc. The error bars indicate the observed uncertainty (1σ) for each of the case types. [[

]]

[[

Figure 1-11. K-infinity Comparison of TGBLA06 vs. MCNP for Various Lattice State Conditions

]]

1.3.2 Conclusions

Extensive qualification of the lattice physics methodology demonstrates that the code will accurately predict the lattice nuclear performance of all GE fuel designs including 10x10 designs. Finally, neutron balance benchmark comparisons between Monte Carlo analysis results and lattice physics calculations for a 10x10 fuel bundle designs, show that the multiplication factor and the neutron absorption and production rates are also in good agreement.

1.4 THREE-DIMENSIONAL NUCLEAR MODEL

The nuclear model is based on coarse mesh nodal, one-group, static diffusion theory. The nodalization is described in Section 1.4.10. The mesh points are distributed approximately every two fast neutron mean free paths. Because of the short thermal neutron mean free path in a water reactor, most neutron diffusion takes place at high neutron energy. Therefore, the model is oriented toward accurate representation of fast neutron diffusion.

It is important to account for lattice fine structure in determining nuclear data for the coarse-mesh global model. Separability is assumed for lattice cells consisting of one or more fuel bundles. The nuclear input preparation is performed by detailed calculations for the lattice cells or fuel types. Coarse-mesh diffusion parameters are fit parametrically as a function of moderator density, exposure, control state, and moderator density history. (Moderator density history accounts for spatial isotopic concentrations which are affected by the neutron spectrum during burnup; the spectrum, in turn, is sensitive to moderator density.) These parametric calculations produce isotopic compositions and three-group cross-section data homogenized over the lattice cell. The methods and procedures used in the lattice physics model are described in Section 1.2. Additional data and correlations are added by a pre-processor system for use in the BWR Simulator. A simplified flow chart can be seen in Figure 1-3.

The nuclear model includes representation of Doppler broadening as a function of effective average fuel temperature. Xenon poisoning is considered with the spatial xenon concentration calculated for equilibrium conditions or input specified for non-equilibrium conditions. Provisions are also made to account for the reactivity effect of crud deposited on fuel rods.

Convergence of inner flux iterations and, separately, the outer void loops is achieved through the use of Chebyshev polynomials. Neutron flux is converted to fission power for thermal-hydraulic coupling.

Spatial isotopic concentrations are calculated for fuel cycle analysis. Simulated in-core instrument readings can also be calculated.

1.4.1 Coarse-Mesh Nodal, One-Group Diffusion Theory

The derivation of the nodal equations begins with the three-group neutron diffusion equations:

$$-\nabla \cdot D_1 \nabla \phi_1(\underline{r}) + \Sigma_1 \phi_1(\underline{r}) = \frac{1}{\lambda} \sum_g \nu_g \Sigma_{fg} \phi_g(\underline{r}) \quad (1.4.1)$$

$$-\nabla \cdot D_2 \nabla \phi_2(\underline{r}) + \Sigma_2 \phi_2(\underline{r}) = \Sigma_{s\ell 1} \phi_1(\underline{r}) \quad (1.4.2)$$

$$-\nabla \cdot D_3 \nabla \phi_3(\underline{r}) + \Sigma_3 \phi_3(\underline{r}) = \Sigma_{s\ell 2} \phi_2(\underline{r}) \quad (1.4.3)$$

where

- g = neutron group; $g=1, 2, \text{ or } 3$
- $\phi_g(\underline{r})$ = neutron flux;
- D_g = diffusion coefficient;
- Σ_g = removal cross section;
- $\Sigma_{s\ell g}$ = slowing-down cross section;
- ν_g = number of neutrons per fission;
- Σ_{fg} = fission cross section; and
- λ = effective multiplication constant.

Define

$$k \equiv \frac{1}{\Sigma_1} \sum_g \nu_g \Sigma_{fg} \phi_g / \phi_1 \quad (1.4.4)$$

$$B_1^2 \equiv \frac{k/\lambda - 1}{M_1^2} \quad (1.4.5)$$

$$M_1^2 \equiv D_1 / \Sigma_1 \quad (1.4.6)$$

Then the equation for the fast group becomes:

$$\frac{1}{D_1} \nabla \cdot D_1 \nabla \phi_1(\underline{r}) + B_1^2 \phi_1(\underline{r}) = 0. \quad (1.4.7)$$

This equation depends implicitly on the resonance (group 2) and thermal (group 3) fluxes through the definition of B_1^2 . These fluxes must be approximated some way in order for the

diffusion calculation to be limited to one group. The procedure used is to assume that the geometric bucklings in all three energy groups are the same.

$$\frac{\nabla \cdot D_3 \nabla \phi_3}{D_3 \phi_3} \sim \frac{\nabla \cdot D_2 \nabla \phi_2}{D_2 \phi_2} \sim \frac{\nabla \cdot D_1 \nabla \phi_1}{D_1 \phi_1} = -B_1^2 \quad (1.4.8)$$

Using these approximations, the resonance-to-fast and thermal-to-resonance flux ratios may be obtained from Equations (1.4.2) and (1.4.3):

$$\phi_2 / \phi_1 \cong \frac{\Sigma_{s\ell 1} / \Sigma_2}{1 + M_2^2 B_1^2} = \frac{\phi_2^\infty / \phi_1^\infty}{1 + M_2^2 B_1^2} \quad (1.4.9)$$

$$\phi_3 / \phi_2 \cong \frac{\Sigma_{s\ell 2} / \Sigma_3}{1 + M_3^2 B_1^2} = \frac{\phi_3^\infty / \phi_2^\infty}{1 + M_3^2 B_1^2} \quad (1.4.10)$$

where ϕ_1^∞ , ϕ_2^∞ , and ϕ_3^∞ denote the fluxes in an infinite system.

These results are then substituted into Equations (1.4.4) and (1.4.5) to obtain:

$$B_1^2 \cong \frac{1}{M_1^2} \left[\frac{1}{\lambda \Sigma_1} \left(\nu \Sigma_{f1} + \left(\nu \Sigma_{f2} + \nu \Sigma_{f3} \frac{\phi_3^\infty / \phi_2^\infty}{1 + M_3^2 B_1^2} \right) \frac{\phi_2^\infty / \phi_1^\infty}{1 + M_2^2 B_1^2} \right) - 1 \right] \quad (1.4.11)$$

This equation is solved by multiplying through by the factors involving B_1^2 and then eliminating terms of order B_1^4 and B_1^6 , yielding:

$$\lambda(1 + M^2 B_1^2) \cong k_\infty + A_\infty B_1^2 \quad (1.4.12)$$

or

$$B_1^2 \cong \frac{k_\infty / \lambda - 1}{M^2 - A_\infty / \lambda} \quad (1.4.13)$$

where the following definitions have been made.

$$M^2 \equiv M_1^2 + M_2^2 + M_3^2 \quad (1.4.14)$$

$$k_\infty \equiv \frac{1}{\Sigma_1} \left(\nu \Sigma_{f1} + \nu \Sigma_{f2} \phi_2^\infty / \phi_1^\infty + \nu \Sigma_{f3} \phi_3^\infty / \phi_1^\infty \right) \quad (1.4.15)$$

$$A_\infty \equiv \frac{1}{\Sigma_1} \left(\nu \Sigma_{f1} (M_2^2 + M_3^2) + \nu \Sigma_{f2} M_3^2 \phi_2^\infty / \phi_1^\infty \right) \quad (1.4.16)$$

Equation (1.4.13) is an approximate expression for the buckling, whereas Equation (1.4.5) is exact.

Equations (1.4.7) and (1.4.13) together form the basis for the one-group model. The next step in the derivation is to discretize these equations in the spatial dimension. In order to limit the number of nodes to a practical value, a coarse-mesh approach is adopted with dimensions roughly 15.24 cm. (6 in.) on each edge. A definition of the model used to describe the core geometry is contained in Section 1.3.3.

The first step is to integrate Equation (1.4.7) over a single node:

$$\frac{1}{\Delta V D_i} \int_{\Delta V} d^3 \underline{r} \nabla \cdot D_i \nabla \phi_i(\underline{r}) + \frac{B_i^2}{\Delta V} \int_{\Delta V} d^3 \underline{r} \phi_i(\underline{r}) = 0. \quad (1.4.17)$$

where the subscript referencing the fast group has been eliminated and replaced with a subscript "i" denoting the node under consideration. Making use of Gauss' Theorem:

$$\frac{1}{\Delta V D_i} \int_{S_i} d\underline{S} \cdot D_i \nabla \phi_i(\underline{r}_s) + B_i^2 \bar{\phi}_i = 0. \quad (1.4.18)$$

where the "bar" over the flux ($\bar{\phi}$) indicates an average over the node.

Discretization

In one dimension, a piecewise linear flux expansion is made:

$$\phi(x) = \phi_i + \frac{(x - x_i)}{\Delta x / 2} (\phi_{si}^+ - \phi_i) \quad x_i \leq x \leq x_i + \Delta x / 2 \quad (1.4.19)$$

$$= \phi_i - \frac{(x - x_i)}{\Delta x / 2} (\phi_{si}^- - \phi_i) \quad x_i - \Delta x / 2 \leq x \leq x_i \quad (1.4.20)$$

where the surface fluxes are discontinuous:

$$f_i^+ \phi_{si}^+ = f_{i+1}^- \phi_{si+1}^- \quad f_i^- \phi_{si}^- = f_{i-1}^+ \phi_{si-1}^+$$

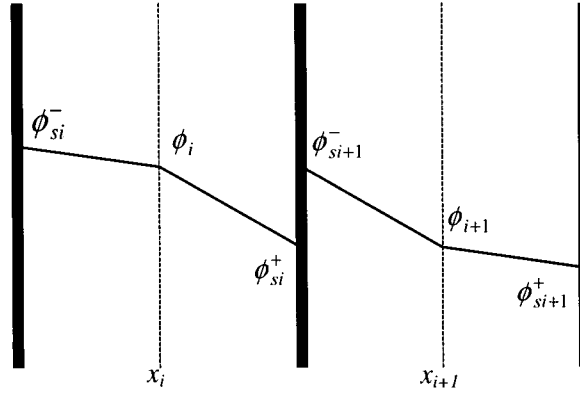


Figure 1-12. Piecewise-Linear Flux Variation

Substituting the piece-wise linear flux expansion into the nodal equation and integrating:

$$\frac{1}{\Delta x} \left[\frac{(\phi_{si}^+ - \phi_i)}{\Delta x/2} + \frac{(\phi_{si}^- - \phi_i)}{\Delta x/2} \right] + \frac{B_i^2}{\Delta x} \left[\phi_i \Delta x + (\phi_{si}^+ - \phi_i) \frac{\Delta x}{4} + (\phi_{si}^- - \phi_i) \frac{\Delta x}{4} \right] = 0 \quad (1.4.21)$$

The surface fluxes are eliminated from these equations by requiring continuous current at the nodal interfaces:

$$J_{s_i} = -D_i \left. \frac{\partial \phi}{\partial x} \right|_{x = x_i + \Delta x/2} = -D_{i+1} \left. \frac{\partial \phi}{\partial x} \right|_{x = x_{i+1} - \Delta x/2} \quad (1.4.22)$$

The derivatives are approximated by finite differences.

$$-D_i \frac{(\phi_{si}^+ - \phi_i)}{\Delta x/2} = -D_{i+1} \frac{(\phi_{i+1} - \phi_{si+1}^-)}{\Delta x/2} \quad (1.4.23)$$

Solving for the surface fluxes:

$$\phi_{si}^+ = \frac{D_i \phi_i + D_{i+1} \phi_{i+1}}{D_i + D_{i+1}} \frac{f_i^+}{f_{i+1}^-} \quad \phi_{si}^- = \frac{D_i \phi_i + D_{i-1} \phi_{i-1}}{D_i + D_{i-1}} \frac{f_i^-}{f_{i-1}^+} \quad (1.4.24)$$

Then the nodal equation can be written:

$$\sum_{j=1}^6 \frac{D_{ij}}{h_{ij}^2 D_i} (\phi_j \zeta_{j,i} - \phi_i \zeta_{i,j}) + B_i^2 \bar{\phi}_i = 0 \quad (1.4.25)$$

where the average nodal flux is defined as

$$\bar{\phi}_i = \phi_i + \frac{1}{8} \sum_{j=1}^6 \frac{D_{ij}}{D_i} (\phi_j \zeta_{j,i} - \phi_i \zeta_{i,j})$$

where the subscript j refers to any one of the six face-adjacent nodes and h_{ij} is the distance between nodes i and j .

The nodal coupling parameter, D_{ij} , is defined as:

$$\begin{aligned} D_{ij} &\equiv \frac{2D_i D_j}{D_i f_j^+ + D_j f_i^-} & i > j \\ &\equiv \frac{2D_i D_j}{D_i f_j^- + D_j f_i^+} & i < j \end{aligned} \quad (1.4.26)$$

and $\zeta_{i,j}$ is defined as:

$$\begin{aligned} \zeta_{i,j} &\equiv f_i^+ & i < j \\ &\equiv f_i^- & i > j \end{aligned}$$

Boundary Conditions

The boundary conditions at the core/reflector interface are of the “mixed” type:

$$D\hat{n} \cdot \nabla F(\underline{r}_s) + \Gamma F(\underline{r}_s) = 0, \quad \underline{r}_s \in \text{core boundary} \quad (1.4.27)$$

Finite differencing the gradient of the flux and solving for Γ :

$$\begin{aligned} \Gamma &= -D_r \frac{\nabla F}{F} \equiv -D_r \frac{(\phi_r - \phi_{sr})}{\phi_{sr} (\Delta x / 2)} & \phi_r > \phi_{sr} \\ &\equiv -D_r \frac{(\phi_{sr} - \phi_r)}{\phi_{sr} (\Delta x / 2)} & \phi_r < \phi_{sr} \end{aligned} \quad (1.4.28)$$

Arbitrarily setting ϕ_r to zero and solving for the reflector diffusion coefficient:

$$D_j = \frac{\Gamma \Delta x}{2} \quad (1.4.29)$$

The value of Γ used in this model is synthesized from the reflector cross sections. A single set of reflector cross sections which vary linearly with the relative water density of the top fuel node may be provided.

1.4.2 Void and Exposure Effects

The nuclear parameters M^2 , $D1$, k_∞ , and A_∞ are obtained from the detailed X-Y physics calculations described in Section 1.2 and performed for lattice cells (fuel types) normally consisting of one fuel bundle and its surrounding water. These multi-group calculations produce three-group cross sections homogenized over the lattice cell. The data are represented by polynomial fits and by Lagrangian interpolation of tabulated values for each fuel type.

In the solution of the coarse mesh nodal approximation of the one-group diffusion theory model, void, exposure, and fuel type conditions of a node in three-dimensional space are used in the fits and tables to interpret nuclear properties for that node. In this way, void feedback, burnup effects, and heterogeneous fuel loading are taken into account.

Void dependence is represented by the ratio of cell average water density relative to saturated water density used in the lattice cell calculation. This ratio is given by:

$$\frac{\rho}{\rho_f} = 1 + \left(\frac{\rho_g}{\rho_f} - 1 \right) [F \alpha_i + (1-F)\alpha_o] \quad (1.4.30)$$

where

- ρ = cell average water density;
- ρ_f and ρ_g = saturated liquid and vapor water density, respectively;
- F = volume fraction of water inside the channel (exclusive of water rods) relative to total water for the cell;
- α_i = in-channel void fraction; and
- α_o = out-of-channel void fraction.

The parameter U is used to represent relative moderator density for the cell:

$$U = \frac{\rho}{\rho_f}. \quad (1.4.31)$$

Every node in three-dimensional space has a value of U at a given operating point during burnup of the core; therefore, U is an instantaneous relative moderator density. By averaging U with respect to exposure of the node E , history-dependent relative moderator density is defined as:

$$UH = \frac{\int U dE}{\int dE}. \quad (1.4.32)$$

Spatial isotopic concentrations in the cell are dependent upon the neutron spectrum during burnup, which is expressed as a function of UH . The spectrum at any point in exposure is expressed as a function of U .

Void distribution in the core is determined by the thermal-hydraulics model (described in Section 1.5) according to power and flow distributions and core average pressure. Exposure is accumulated during plant simulation by knowing power and fuel weight distributions and the time of operation (or core average accumulated exposure). Local U , UH , and E conditions determine nuclear properties of a node according to correlations of the lattice cell physics calculations. For each fuel type, k_{∞} is dependent upon U , UH , and E , while M^2 , D_1 , and A_{∞} are expressed in terms of U only.

1.4.3 Control Rod Effects

The detailed lattice cell calculations described in Section 1.2 are performed with the control rod in or out. Therefore, nuclear parameters are obtained for each fuel type at several void and exposure conditions, controlled and uncontrolled. In the three-dimensional diffusion theory solution, the control rod configuration is accounted for by using controlled or uncontrolled data for each node. If a control rod is only partially inserted into a node, linear averaged nuclear data are used. For each fuel type, k_{∞} , D_1 , and M^2 are control dependent. A_{∞} , which is a small correction to the migration area for fast and resonance fission, is not strongly dependent on the presence of a control blade and therefore uncontrolled data are used.

During plant simulation, control rod maneuvering affects the static power distribution and, therefore, void distribution and exposure accumulation.

1.4.4 Doppler Effects

Fuel temperature (T) affects resonance absorption in uranium and plutonium (the Doppler effect). This is accounted for by making a Doppler reactivity correction of k_{∞} at each node in the form:

$$k_{\infty}(T) = k_{\infty}(T_o) \left[1 + \frac{\Delta k}{k}(T) \right] \quad (1.4.33)$$

where T_o represents base fuel temperature, and

$$\frac{\Delta k}{k}(T) = C_T \left[\sqrt{T} - \sqrt{T_o} \right]. \quad (1.4.34)$$

The Doppler coefficient C_T is dependent upon control and U for each fuel type. It is determined by lattice cell physics calculations performed parametrically as a function of fuel temperature.

The effective fuel temperature (T) is represented as a quadratic function of the nodal power for each fuel type.

$$T(P_N) = a_0 + a_1 P_N + a_2 P_N^2, \text{ } ^\circ\text{K}$$

where

$$\begin{aligned} P_N &= P_{ijk} * PDC/P_{base} \\ P_{ijk} &= \text{Relative nodal power} \\ PDC &= \text{Core Power Density} \\ P_{base} &= \text{base (reference) power density} \end{aligned}$$

This relationship is obtained by detailed heat conduction solutions using appropriate thermal conductivity and fuel rod diameter. Knowing the power and void distributions, Equation (1.4.34) gives Doppler reactivity for each node.

1.4.5 Xenon Effects

Xenon is a fission product that acts as a strong absorber of thermal neutrons. It is produced directly from fission and indirectly by decay of iodine. The xenon poisoning effect is accounted for by making a xenon reactivity correction to k_{∞} at each node in the form:

$$k_{\infty}(N_x) = k_{\infty}(N_x = 0) \left[1 + \frac{\Delta k}{k}(N_x) \right] \quad (1.4.35)$$

where N_x represents xenon concentration. Xenon reactivity is expressed by:

$$\frac{\Delta k}{k}(N_x) = C_x \frac{N_x}{N_x^r} \quad (1.4.36)$$

where N_x^r represents xenon concentration at rated power density. The xenon coefficient C_x is evaluated at rated power density and represented as a function of exposure, control state, and water density for each fuel type.

Neglecting absorption in iodine, the static (equilibrium) xenon concentration may be expressed by:

$$N_x = \frac{(\gamma_x + \gamma_i) f}{\lambda_x + \sigma_x \phi_t} \quad (1.4.37)$$

where

- | | | |
|-----------|---|---|
| γ | = | fission yield; |
| i | = | iodine; |
| f | = | fission rate; |
| λ | = | decay constant; |
| σ | = | microscopic absorption cross section; and |
| ϕ_t | = | thermal flux. |

Therefore,

$$\frac{N_x}{N_x^r} = \frac{f}{f^r} \frac{(g+1)}{\left(g + \frac{\phi_t}{\phi_t^r} \right)} \quad (1.4.38)$$

where r represents conditions at rated power density, and

$$g = \frac{\lambda_x}{\sigma_x \phi_t^r} \quad (1.4.39)$$

Letting p be nodal power density relative to rated, and assuming

$$p = \frac{f}{f^r} = \frac{\phi_i}{\phi_i^r} \quad (1.4.40)$$

leads to

$$\frac{\Delta k}{k}(N_x) = C_x p \frac{(g+1)}{(g+p)} \quad (1.4.41)$$

The parameter g is evaluated at one power condition for each fuel type. Knowing power and exposure distributions, Equation (1.4.36) gives xenon reactivity for each node.

1.4.6 Conversion of Flux to Power

Solution of the one-group diffusion theory model (Equation (1.4.9)), using nodal-dependent values for the nuclear parameters k_∞ , M^2 , D_1 , and A_∞ , yields the neutron flux ϕ_i at each node. Neutron flux must be converted to fission power to determine how much heat is being produced to evaluate thermal-hydraulic feedback effects such as flow, void, and fuel temperature. The equation for power is made consistent with the one-group model in the following derivation.

The power at each node "i" in the core is determined by integrating the fission density over the nodal volume:

$$P_i = \frac{1}{\Delta V} \int d^3r \varepsilon_i \sum_g \Sigma_{fgi} \phi_{gi}(\underline{r}) \quad (1.4.42)$$

$$= \varepsilon_i \sum_g \Sigma_{fgi} \bar{\phi}_{gi} \quad (1.4.43)$$

where Σ_{fg} is the macro fission cross section and ε_i is a conversion factor relating fissions to energy. In this model, ε_i is assumed to be constant throughout the core and arbitrarily set to 1. The power is normalized such that the average nodal power is 1.

The epi-thermal flux is estimated from the infinite lattice flux ratio:

$$\frac{\bar{\Phi}_2}{\bar{\Phi}_1} = \frac{\Phi_2^\infty}{\Phi_1^\infty} = \frac{\Sigma_{s1}}{\Sigma_2}$$

The thermal flux estimation starts with the thermal group equation:

$$-\nabla \cdot D_3 \nabla \Phi_3(\underline{r}) + \Sigma_3 \Phi_3(\underline{r}) = \Sigma_{s2} \Phi_2(\underline{r}) \quad (1.4.44)$$

Integrating over the volume of the node:

$$\frac{1}{V} \iiint \nabla J_3 dV + \frac{1}{V} \iiint \Sigma_3 \Phi_3 dV = \frac{1}{V} \iiint \Sigma_{sl2} \Phi_2 dV \quad (1.4.45)$$

Transforming to a surface integral using Gauss's Theorem:

$$\frac{1}{V} \iint_S J_3 \cdot \hat{n} dA + \Sigma_3 \bar{\Phi}_3 = \Sigma_{sl2} \bar{\Phi}_2 \quad (1.4.46)$$

The surface integral term is simply a sum of the surface currents times surface areas:

$$\frac{\bar{\Phi}_3}{\bar{\Phi}_1} = \frac{\Phi_3^\infty}{\Phi_2^\infty} \frac{\bar{\Phi}_2}{\bar{\Phi}_1} - \frac{\sum_n J_n S_n}{V \Sigma_3 \bar{\Phi}_1} \quad (1.4.47)$$

$$\frac{\bar{\Phi}_3}{\bar{\Phi}_1} = \frac{\Phi_3^\infty}{\Phi_2^\infty} \frac{\bar{\Phi}_2}{\bar{\Phi}_1} - \frac{\sum_n J_n S_n}{V \Sigma_3 \bar{\Phi}_1} \quad (1.4.48)$$

where S_n is the surface area of node face "n".

The thermal flux estimate is simplified to:

$$\frac{\bar{\Phi}_3}{\bar{\Phi}_1} = \frac{\Phi_3^\infty}{\Phi_1^\infty} - \frac{\sum_n J_n S_n}{V \Sigma_3 \bar{\Phi}_1} \quad (1.4.49)$$

The surface currents can be approximated from one-dimensional analytical solutions.

The thermal diffusion equations for this node and an adjacent node are:

$$\begin{aligned} \nabla \cdot D_3 \nabla \Phi_3(r) - \Sigma_3 \Phi_3(r) + \Sigma_{sl2} \Phi_2(r) &= 0 & x < 0 \\ \nabla \cdot D_{3n} \nabla \Phi_{3n}(r) - \Sigma_{3n} \Phi_{3n}(r) + \Sigma_{sl2n} \Phi_{2n}(r) &= 0 & x > 0 \end{aligned} \quad (1.4.50)$$

where the subscript "n" denotes the adjacent node corresponding to face "n".

Assuming uniform slowing down sources the equations may be expressed as:

$$\begin{aligned} D_3 \frac{d^2 \Phi_3}{dx^2} - \Sigma_3 \Phi_3(x) + S &= 0 & x < 0 \\ D_{3n} \frac{d^2 \Phi_{3n}}{dx^2} - \Sigma_{3n} \Phi_{3n}(x) + S_n &= 0 & x > 0 \end{aligned} \quad (1.4.51)$$

where the source terms are defined as:

$$S = \Sigma_{sl2} \bar{\Phi}_2 \quad S_n = \Sigma_{sl2n} \bar{\Phi}_{2n} \quad (1.4.52)$$

The boundary conditions can be expressed as:

$$\Phi_3(-\infty) = \Phi_3^\infty = \frac{\sum_{s/2} \bar{\Phi}_2}{\Sigma_3} \quad \Phi_{3n}(+\infty) = \Phi_{3n}^\infty = \frac{\sum_{s/2n} \bar{\Phi}_{2n}}{\Sigma_{3n}} \quad (1.4.53)$$

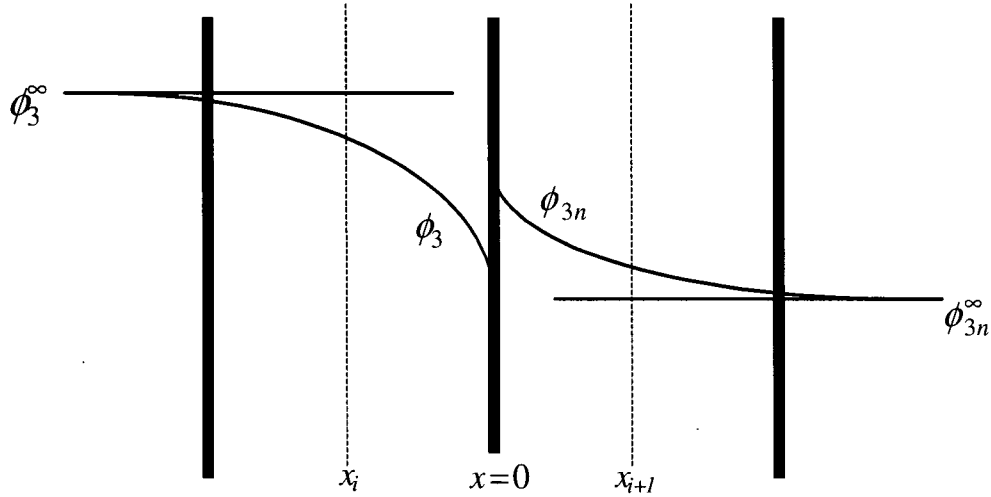


Figure 1-13. Thermal Flux Variation Within and Between Nodes

The interface conditions can be expressed as:

$$\begin{aligned} -D_3 \frac{d\Phi_3}{dx} \Big|_{x=0} &= -D_{3n} \frac{d\Phi_{3n}}{dx} \Big|_{x=0} && \text{continuous current} \\ f_3^\pm \Phi_3(x=0) &= f_{3n}^\mp \Phi_{3n}(x=0) && \text{discontinuous flux} \end{aligned} \quad (1.4.54)$$

Dropping the subscript “3”, the general solutions are :

$$\begin{aligned} \Phi(x) &= Ae^{-\kappa x} + Be^{+\kappa x} + \frac{S}{\Sigma} && x < 0 \\ \Phi_n(x) &= A_n e^{-\kappa x} + B_n e^{+\kappa x} + \frac{S_n}{\Sigma_n} && x > 0 \end{aligned} \quad (1.4.55)$$

where “kappa” is defined as the inverse migration area:

$$\kappa^2 \equiv \frac{1}{M^2} = \frac{\Sigma}{D} \quad \kappa_n^2 \equiv \frac{1}{M_n^2} = \frac{\Sigma_n}{D_n} \quad (1.4.56)$$

The interface currents are expressed as:

$$J_n = -D \left. \frac{d\Phi}{dx} \right|_{x=0} = D\kappa(A - B) \quad (1.4.57)$$

Applying the boundary and interface conditions, the “B” coefficient is found and the thermal interface currents are:

$$J_n = -D\kappa B = \frac{\left(f^\pm \frac{S}{\Sigma} - f_n^\mp \frac{S_n}{\Sigma_n} \right)}{\left(\frac{f^\pm}{\kappa D} + \frac{f_n^\mp}{\kappa_n D_n} \right)} \quad (1.4.58)$$

These interface currents are used to calculate the thermal flux estimate of Equation (1.4.49) which is needed in the nodal power calculation, Equation (1.4.42).

1.4.7 Isotopic Tracking

This section has been removed.

1.4.8 In-Core Instrumentation Calculation

The BWR incorporates in-core nuclear instrumentation to measure operating power distributions. These monitors are located in the bypass flow gap at the corners of selected four bundle cells. The monitor reading is influenced by each of these surrounding bundles. The BWR Simulator calculates predicted in-core readings for either gamma or thermal neutron instrumentation which can be compared with measured in-core data to qualify the accuracy of the analytical model. Also, the calculated in-core results can be used to predict monitor response during actual BWR operation. The models described in this section are fuel type dependent.

The detector response at axial node k in a given detector string is an average response based on estimates from the four surrounding nodes:

$$R_k = \frac{P_{ijk} DR_{ijk} + P_{i+ljk} DR_{i+ljk} + P_{ij+lk} DR_{ij+lk} + P_{i+l+j+lk} DR_{i+l+j+lk}}{4} \quad (1.4.59)$$

where P_{ijk} is the relative nodal power and DR_{ijk} is the nodal detector response. The nodal detector response is dependent on fuel type, exposure, voids, void history, control fraction and detector type (gamma or thermal).

1.4.9 Power-Void Iteration

For a given control rod pattern and exposure distribution, material buckling B^2 depends upon the thermal-hydraulic feedback effects of moderator density, fuel temperature and possible crud deposition. Equilibrium xenon distribution is another feedback mechanism. If B^2 is known (or assumed known) at every node, solution of the one-group diffusion theory model (Equation

(1.4.7)) yields the flux distribution. This solution involves inner iterations to determine the fundamental mode flux and effective multiplication constant k .

Once the flux distribution is determined, fission power distribution is given by Equation (1.4.42). The power distribution affects thermal-hydraulics in the reactor. In particular, fission power determines fuel temperature and heat flux to the moderator. Fuel temperature establishes the amount of Doppler feedback in accordance with Equation (1.4.34). Heat flux affects the amount of boiling in the channel, which determines moderator density feedback and channel pressure drop. Flow into each channel must be distributed to balance the pressure drop across all channels because the lower plenum to upper plenum pressure drop is constant. Equilibrium xenon feedback is expressed in terms of relative power distribution by Equation (1.4.41).

The resulting feedback effects may not be the same as originally assumed in the determination of material buckling B^2 . In this case, flux must be reevaluated to represent the new B^2 distribution. This defines an outer loop iteration, which must be continued until the fission power distribution is in equilibrium with the distribution of feedback effects (power-void iteration). The iteration is represented schematically in Figure 1-14.

After power is calculated and before performing additional flux iterations (if required), a neutron balance calculation is performed to improve the estimate of effective multiplication constant k .

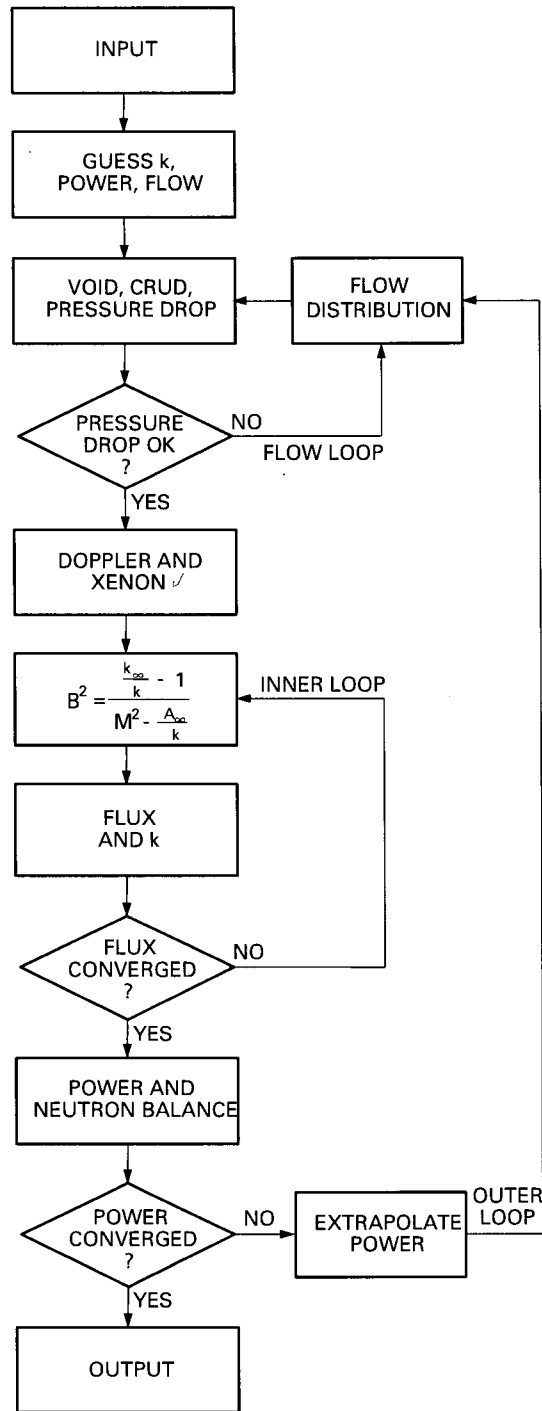


Figure 1-14. Power-Void Iteration Flow Chart

1.4.10 Core Geometry for Nuclear Model

The core is described in X-Y-Z geometry with the restriction that there is equal mesh spacing in the X-Y directions. The X, Y, Z mesh is indicated by i, j, k nomenclature, respectively (Figure 1-15 and Figure 1-16). In a horizontal plane, each fuel assembly or flow channel is described by one mesh point at the center. Mesh point (1,1,k) is in the upper left corner of horizontal plane, k. Vertically, the first point (k=1) is $(\Delta Z/2)$ away from the bottom, and the last point (k=KMAX) is $(\Delta Z/2)$ from the top. In addition to full core representation, quarter-core and half-core options are available with either mirror or rotational symmetry conditions (Figure 1-16).

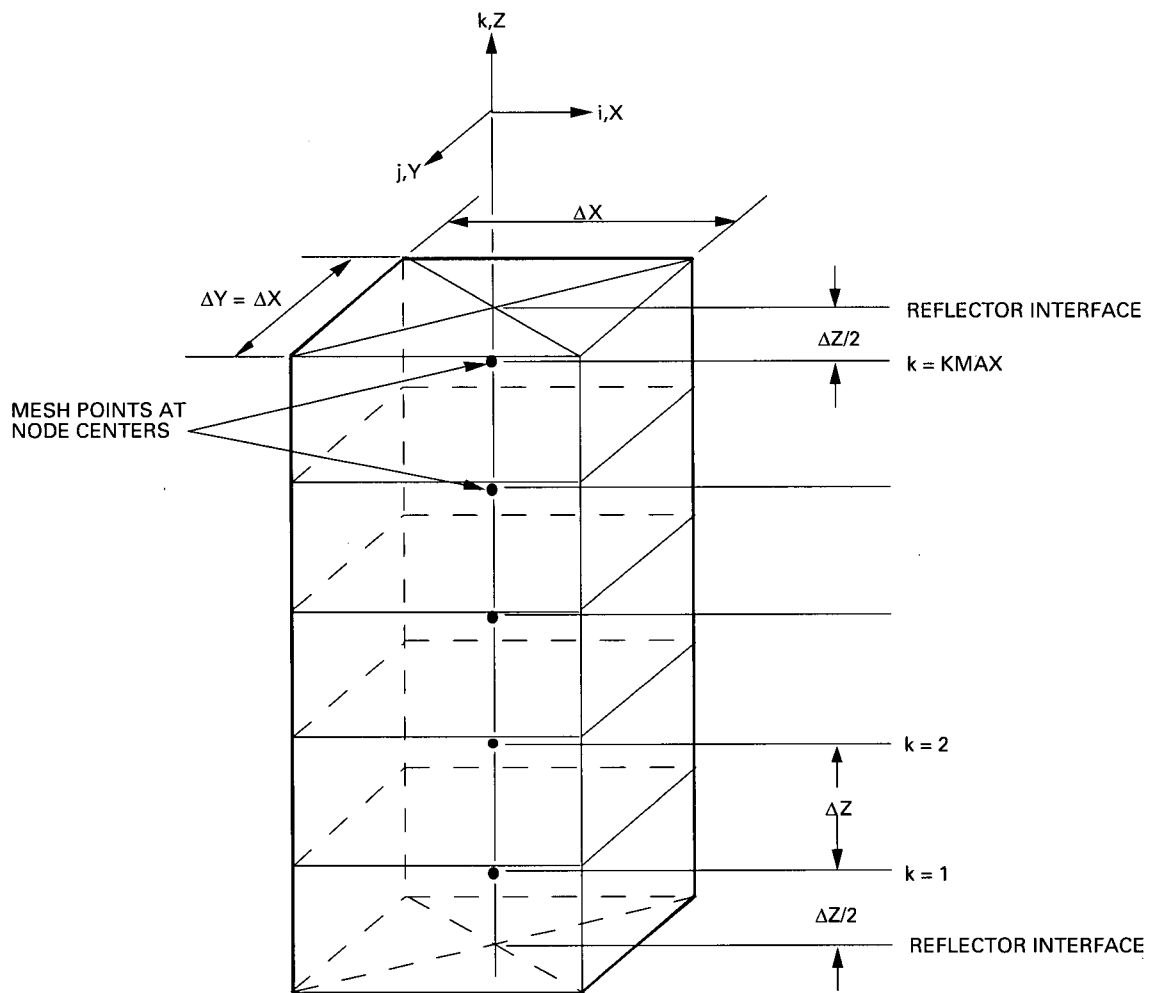


Figure 1-15. Node and Mesh Arrangement for a Given Channel

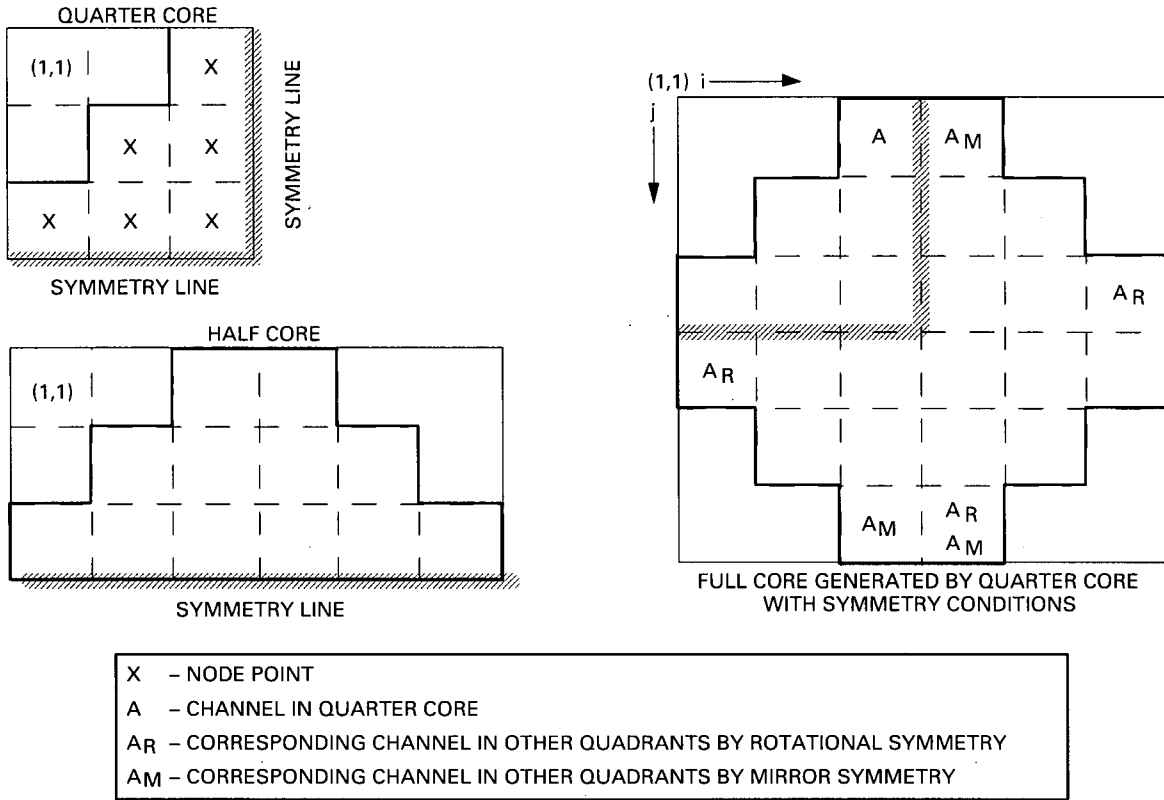


Figure 1-16. BWR Symmetry Options

1.4.10.1 Channel Types

Different fuel assembly characteristics are provided by making the appropriate quantities channel-type-dependent. All mesh points in a vertical line have the same channel type characteristics (Figure 1-17).

The thermal-hydraulic and geometric properties of a fuel assembly are channel-type-dependent. Different channel types are channels with different flow properties, axial Gd distribution, channel thickness, fuel rod diameter, flow area, etc. A typical plant might have three channel types for the initial loading with different axial Gd distributions. Subsequent core loadings could have more channel types. The program presently is dimensioned for a maximum of 20 channel types.

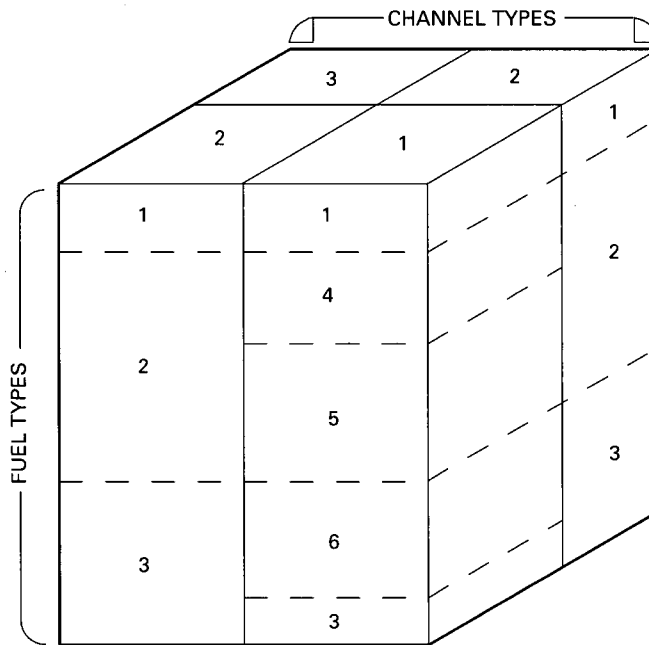


Figure 1-17. Channel and Fuel Types

1.4.10.2 Fuel Types

Different fuel characteristics are provided by definition of a fuel type, it, which may vary axially within each channel type. This two-dimensional array defines the fuel type present at axial node k in channel type i . Thus, all channels of type i have the same axial fuel characteristics (Figure 1-17).

The nuclear properties within individual planes of a fuel assembly vary with fuel type. Different fuel types typically are defined for varying initial enrichments, gadolinia poison rods, etc.

1.4.10.3 Orifice Types

Any of three different orifice types can be associated with the location (i,j) . The channel flow and bypass flow correlation coefficients are a function of orifice type. The orifice type is set and, even though the fuel at (i,j) is moved to (i',j') , the orifice type remains at (i,j) . This allows an analysis of both a fixed grid plate orificing arrangement and channels in which the orificing is built into the nose piece of the fuel assembly, since orifice loss coefficients can also be assigned to the channel itself.

1.4.10.4 Control Rod Positions

A control rod may be associated with each channel in the core. The control rod for point (i,j,k) is located in the lower right corner of the channel at (i,j) (Figure 1-18).

1.4.10.5 In-Core Monitor Positions

Similar to the control rod definition, the in-core monitor locations are assigned to the lower right of a mesh point (Figure 1-18). The location of the monitors is only needed for an edit of simulated instrument response.

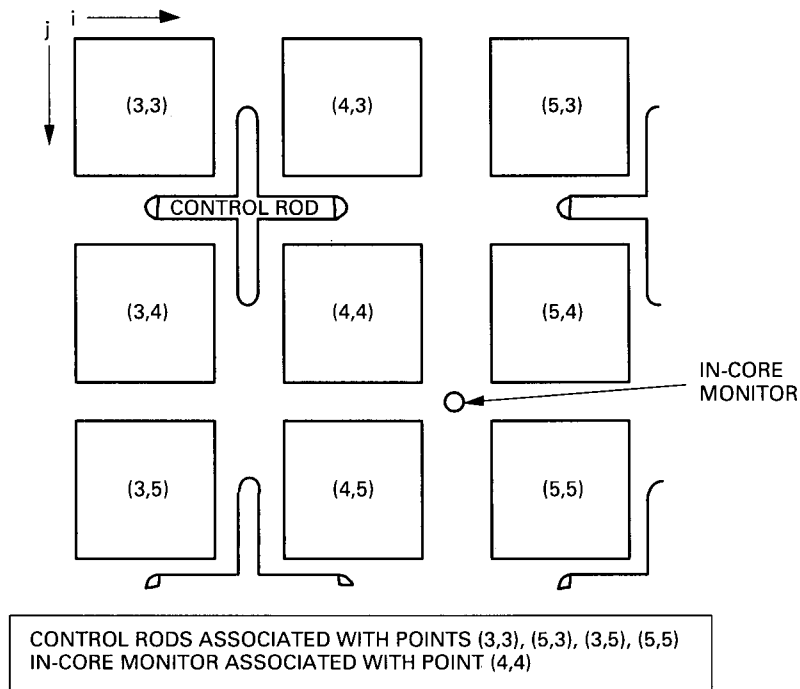


Figure 1-18. Control Rod and Monitor Positions

1.5 THERMAL-HYDRAULICS MODEL

Power-void feedback of a BWR core makes the thermal-hydraulic representation of considerable importance to the nuclear calculation. Nuclear parameters and, therefore, the power distribution are sensitive to local steam void content.

Formulas from the 1967 ASME Steam Tables are used to evaluate coolant properties as a function of reactor core pressure and inlet enthalpy. All thermal-hydraulic variables are assumed to vary linearly between nodes, where the nodal representation is the same as that for the neutron flux (Figure 1-15 in Section 1.4.10); therefore, the thermal-hydraulic model is consistent with the difference equations used for solution of the nuclear model.

In the BWR, the nominal total core flow is obtained from external sources for use in the 3D simulator. The typical source for the total core flow is the plant instrumentation or external analytical analysis. For the ESBWR core design, the nominal core flow is obtained through the use of the TRACG model [Reference 12]. The flow distribution for the characteristic parallel channels is determined by balancing core pressure drop. Characteristic channels are determined by combinations of total channel power, axial power shape, inlet orifice design, channel geometry (e.g., number of fuel rods, spacer design, lower and upper tie plate design), and buildup of crud on the fuel rods. The flow into individual channels is obtained by interpolation among characteristic channels of the same geometry and orifice type as a function of radial and axial power factors and crud thickness.

The axial enthalpy and quality distribution is determined for each channel by a nodal energy balance which considers fuel rod heat flux to the coolant, neutron moderation and gamma heating in the coolant and in the flow channel wall, heat transfer through the channel wall to the bypass region, and γ , (n,γ) , and (n,α) heating in control blades. The void distribution is given by a void-quality correlation which provides a physically based representation of sub-cooled and bulk boiling through a few empirical constants which describe the local flow structure. Part length fuel rods are treated in the same manner as in the steady state thermal hydraulics evaluation model.

Flow-power-void iteration is required to reach an equilibrium condition (Figure 1-14). Once this is obtained, the thermal-hydraulics model enables evaluation of the margin relative to thermal limits.

1.5.1 Flow Distribution

The purpose of the flow distribution calculation is to determine the distribution of total core inlet flow into individual channels, such that the pressure drop across each channel is the same. This pressure drop is given by a combination of friction, elevation, acceleration, and local losses, which are influenced by coolant density, orificing, lower and upper tie plate design, spacer design, fuel bundle geometry, and crud thickness. Coolant density is determined by pressure, inlet subcooling, and the distribution of steam voids, which is affected by the total power generated in the fuel rods within the channels and by the axial power distribution.

Because current BWR designs have a large number of fuel channels (up to 1280), the following steps are used to reduce the computational effort for determining flow distribution:

- (1) Define a limited number of characteristic channels.
- (2) Obtain the flow in each characteristic channel by balancing channel pressure drops while preserving total core flow.
- (3) Calculate the flow in each individual channel of the reactor based upon the variation of that channel relative to the characteristic channels.

Characteristic channels are defined by combinations of the parameters primarily affecting pressure drop;

- (1) total channel power;
- (2) axial power shape;
- (3) crud deposit thickness;
- (4) orifice size and
- (5) channel geometry.

To calculate the radial power effects, the maximum (RADMAX) and minimum (RADMIN) bundle powers are determined from the bundle power distribution $AVGBP_{ij}$. The characteristic radial powers are determined as follows:

$$[[\quad \quad \quad]] \quad (1.5.1)$$

The total number of radial powers $NRAD$ is:

$$[[\quad \quad \quad]]$$

The axial power shape of each channel is characterized by the fraction of the power, which is below the core mid-plane. This fraction is calculated as follows:

$$[[\quad \quad \quad]] \quad (1.5.2)$$

where,

$KMAX$ is the maximum value of K in the core mesh,

KK is equal to $KMAX/2$,

PC_{ij} is the integrated bundle power of bundle at location (i,j) = [[]],

P_{kij} is the nodal power.

As with the radial power, the maximum ($AXMAX$) and minimum ($AXMIN$) axial shape factors are calculated and used to determine the axial power shapes for the characteristic channels.

$$\left[\begin{array}{c} \text{---} \\ \text{---} \\ \text{---} \end{array} \right] \quad (1.5.3)$$

The total number of axial power shapes, NAX , to be considered is:

$$\left[\begin{array}{c} \text{---} \\ \text{---} \end{array} \right]$$

The crud parameter is taken to be the average crud thickness in a bundle, $CRUD_{ij}$. This parameter is calculated assuming equal nodal volumes as:

$$\left[\left[\begin{array}{c} \text{---} \\ \text{---} \end{array} \right] \right] \quad (1.5.4)$$

where $TCRU_{kij}$ is the crud array.

The maximum ($CRDMAX$) and minimum ($CRDMIN$) crud values are determined and used to calculate the crud

$$\left[\left[\begin{array}{c} \text{---} \\ \text{---} \end{array} \right] \right] \quad (1.5.5)$$

The total number of crud sizes, $NKRD$, is:

$$\left[\left[\begin{array}{c} \text{---} \\ \text{---} \end{array} \right] \right]$$

The effects of bundle geometry on the flow distribution are determined by two parameters: (1) the orifice loss and (2) the local losses in the bundle itself. These local losses are related to the lower tie plate and the spacers, which define a characteristic geometry (channel) type.

The geometric and power characteristics associated with each of the characteristic bundles are defined by all possible combinations of RADP(1), RADP(2), AXP(1), AXP(2), CRD(1), CRD(2) and by the geometry and orifice types.

The total number of characteristic channels is defined as

$$[[\quad \quad \quad]] \quad (1.5.6)$$

where,

NORF is the actual number of orifice types in the core,

NCHT is the actual number of geometry types in the core.

The characteristic channel at each core location (i,j) is assigned as follows:

$$[[\quad \quad \quad]] \quad (1.5.7)$$

where,

$$[[$$

]]

The following major assumptions are used to efficiently compute pressure drop and flow for the characteristic channels:

- (1) Bypass (leakage) flow (Subsection 1.5.4) is given.

- (2) [[
- (3)
- (4)
- (5)
- (6)]]

Figure 1-19 is a schematic of characteristic channel nodalization depicting the active fuel section (which contains heated fuel rods), the unheated section with rods, and the unheated section without rods. Pressure drop for a characteristic channel is determined by summing the following components:

- (1) local loss pressure drop through the orifice;
- (2) acceleration pressure drop due to the area change from the inlet area to the rodded bundle area;
- (3) friction pressure drop in the heated section;
- (4) elevation pressure drop in the heated section;
- (5) acceleration pressure drop due to the density change in the heated section;
- (6) local loss pressure drop through the heated section;
- (7) acceleration pressure drop due to the area change from the rodded bundle area to the outlet area;
- (8) friction pressure drop in the unheated rodded section and
- (9) elevation pressure drop in the unheated section.

Summarizing, characteristic channel pressure drop is given by:

$$\Delta P_{\text{tot}} = \Delta P_{\text{fri}} + \Delta P_{\text{ele}} + \Delta P_{\text{loc}} + \Delta P_{\text{acc}} \quad (1.5.8)$$

The friction pressure drop is calculated from the Darcy-Weisbach expression:

$$\Delta P_{\text{fri}} = \left(\frac{L}{D_H} \right) \left(\frac{W}{A} \right)^2 \frac{f \phi_{TPF}^2}{2 g_c \rho_t} \quad (1.5.9)$$

where

$$L = \text{length of the flow passage}$$

A = flow area

D_H = hydraulic diameter

ρ_ℓ = average liquid density over L (in two-phase flow, ρ_ℓ is saturated liquid density).

W = mass flow rate for the characteristic channel

f = single-phase friction factor

ϕ_{TPF}^2 = two phase friction multiplier

The single-phase friction factor is calculated from:

$$[[\quad \quad \quad]] \quad (1.5.10)$$

where a, b and c are correlation coefficients, N_{Re} is Reynold's number evaluated at saturation properties, and ϵ is the surface roughness.

[[

]]

Figure 1-19. Schematic of Characteristic Channel Nodalization

The two-phase friction multiplier is based upon a modified Chisholm model:

$$\left[\left[\left(\frac{\rho_f}{\rho_g} \right)^2 \left(\frac{f_g}{f_f} \right) \right] \right] \quad (1.5.11)$$

where

X is flow quality

$$\left[\left[\left(\frac{\rho_f}{\rho_g} \right)^2 \left(\frac{f_g}{f_f} \right) \right] \right]$$

$$\Gamma^2 = \left(\frac{\rho_f}{\rho_g} \right)^2 \left(\frac{f_g}{f_f} \right)$$

TPFM_{1N}...TPFM_{6N} = two phase friction multiplier constants

and

ρ_ℓ = average liquid density over L (in two-phase flow, ρ_ℓ is saturated liquid density).

f = single-phase friction factor

The second term in Equation (1.5.8), elevation pressure drop, is calculated from

$$\Delta P_{ele} = \Delta Z \bar{\rho} \quad (1.5.12)$$

where ΔZ is the distance over which the elevation pressure drop is calculated and $\bar{\rho}$ is average density over the distance ΔZ . In the sub-cooled portion of the bundle, average density is:

$$\bar{\rho} = \frac{1}{2} (\rho_z + \rho_{z+\Delta z}) \quad (1.5.13)$$

In the two-phase portion of the bundle, average density is:

$$\bar{\rho} = (1 - \bar{\alpha}) \rho_f + \bar{\alpha} \rho_g \quad (1.5.14)$$

where

$$\bar{\alpha} = \frac{1}{2} (\alpha_z + \alpha_{z+\Delta z}) \quad (1.5.15)$$

and α is the void fraction and ρ_f and ρ_g are saturated liquid and vapor densities.

The third pressure drop term in Equation (1.5.8) is the irreversible pressure drop due to local flow disturbances such as fuel rod spacers or area changes in the flow path. The formulation used is:

$$\Delta P_{loc} = \left(\frac{W}{A_K} \right)^2 \frac{K \phi_{TPF}^2}{2g_c \rho_\ell} \quad (1.5.16)$$

where

K = loss coefficient;

A_K = area associated with the loss coefficient (not necessarily equal to the flow area);

ρ_ℓ = liquid density at the restriction (in sub-cooled flow, ρ_ℓ is linearly interpolated to the elevation of the flow restriction; in two-phase flow, ρ_ℓ is saturated liquid density); and

ϕ_{TPF}^2 = two phase friction multiplier

The two-phase local loss multiplier used is the homogeneous multiplier:

$$\phi_{TPL}^2 = 1 + \left(\frac{\rho_f}{\rho_g} - 1 \right) X \quad (1.5.17)$$

where X is a function of the two phase friction multipliers.

The final pressure drop component in Equation (1.5.8) results from acceleration. This includes the reversible pressure difference experienced by a fluid at an area change (the irreversible component is accounted for with a local loss coefficient) and the pressure difference resulting from density changes such as steam formation.

The reversible pressure difference resulting from a flow area change is given by:

$$\Delta P_{acc} = (1 - \sigma_A^2) \left(\frac{W}{A_2} \right)^2 \frac{1}{2g_c \rho} \quad (1.5.18)$$

where

$$\sigma_A = \frac{A_2}{A_1} = \frac{\text{final flow area}}{\text{initial flow area}}$$

The density ρ in Equation (1.5.18) is generated differently for single-phase and two-phase flow. In single-phase flow, ρ is the fluid density of the sub-cooled liquid at the elevation of the area change. In two-phase flow:

$$\rho = \frac{\rho_{KE}^2}{\rho_H} \quad (1.5.19)$$

ρ_{KE} = kinetic energy density, and

ρ_H = homogeneous density.

The kinetic energy density is defined by:

$$\frac{1}{\rho_{KE}^2} = \frac{X^3}{(\rho_g \alpha)^2} + \frac{(1-X)^3}{[\rho_f(1-\alpha)]^2} \quad (1.5.20)$$

and the homogeneous density is given by:

$$\frac{1}{\rho_H} = \frac{X}{\rho_g} + \frac{(1-X)}{\rho_f} \quad (1.5.21)$$

The acceleration pressure difference due to a density change is given by:

$$\Delta P_{acc} = \frac{1}{g_c} \left(\frac{W}{A} \right)^2 \left[\frac{1}{\rho_{H_2}} - \frac{1}{\rho_{H_1}} \right] \quad (1.5.22)$$

where ρ_H is the homogeneous water density.

An iterative process is required to determine the flow in each characteristic channel which results in equal channel pressure drop for all channels while preserving total core flow. The initial guess for flow in each characteristic channel is assumed to be equal to the total core flow rate divided by the total number of bundles. The first estimate of the core pressure drop is obtained by calculating the core pressure drop of one of the characteristic channels, for example, the one with the largest number of bundles associated with it. A separate iteration on flow is conducted for each characteristic channel. Let i represent the iteration number and WCB_N^i be the flow rate for channel N . After each iteration, the pressure drop ΔP_N^i is compared with the core pressure drop and convergence is achieved if:

$$[[\quad \quad \quad]] \quad (1.5.23)$$

where $PCOND$ is an input variable.

If the first estimate of the characteristic channel flow, WCB_N^1 does not produce the required pressure drop, a new flow guess is generated from the following ratio:

$$[[\quad \quad \quad]] \quad (1.5.24)$$

For succeeding iterations, a simple linear interpolation is used:

$$[[\quad \quad \quad]] \quad (1.5.25)$$

Convergence of the core pressure drop is gauged by summing all the characteristic channel flows and comparing the results against the total core flow, reduced by bypass flow:

$$[[\quad \quad \quad]] \quad (1.5.26)$$

where,

$WCOND$ is an input constant,

WCT the total core flow,

$BUNDL_N$ the number of bundles in the core associated with characteristic channel N ,

$RLFF$ is the leakage flow fraction.

$RLFF$ is calculated as $[[\quad \quad]]$, where the total bypass flow $WBPR$ is a know quantity obtained by a two-dimensional linear table lookup using the total core power and the total core flow. The bypass flow in PANAC11 can be input or obtained from a $[[$

]].

For the PANAC11 calculations presented in the DCD, the first technique was used (i.e. $[[$ $]]$). The value of the bypass flow was obtained from a $[[$ $]]$, which was in turn $[[$

$]]$.

If the criteria is not met, then the core pressure drop is incorrect and is adjusted. This is accomplished by renormalizing the characteristic channel flows such that:

$$[[\quad \quad \quad]] \quad (1.5.27)$$

and then repeating the iterations on channel flow.

The characteristic channel flow rates are then distributed to individual channels of the same geometry and orifice type by linear interpolation on total channel power axial power shape, and crud thickness. The flow rate in each fuel bundle, which is a member of the group of channels represented by the characteristic channel IX_{ij} is set equal to the characteristic channel flow, $WCB(IX)$, modified by corrections which vary linearly with the amount that the actual bundle at

(i,j) is removed from characteristic variables, namely radial power, axial power, and crud build-up. The bundle flow is then calculated as follows:

$$\left[\left[\right] \right] \quad (1.5.28)$$

where $DWDRAD_{IX}$, $DWDAXP_{IX}$ and $DWDCRD_{IX}$ are derivatives of the flow with respect to the radial power, axial power factor and crud thickness. These derivatives are determined by first calculating the flow rates, using the known converged pressure drop, $DELTP$, and the average values of the continuous variables $RADP(3)$, $AXP(3)$ and $CRUD(3)$. For example, the flow versus radial power is shown in the illustration below.

[[]]

Subscript M_1 denotes the characteristic bundle with specific geometry, axial power and the lowest level of radial power $RADP(1)$, and M_2 denotes the characteristic bundle with the identical geometry and axial power but with the highest level of radial power $RADP(2)$. The flow rates associated with both characteristic bundles M_1 and M_2 are calculated during the

pressure drop iterations. By calculating the flow for the same geometry and axial power, and using the average radial power RADP(3), the derivatives at M_1 and M_2 can be calculated as

$$\left[\begin{matrix} \\ \end{matrix} \right] \quad (1.5.29)$$

and

$$\left[\begin{matrix} \\ \end{matrix} \right] \quad (1.5.30)$$

These calculations are performed for every combination of geometry and axial power shape. In a similar way, derivatives are calculated for the axial power and crud thickness. After the bundle flows have been calculated, they are normalized such that the sum of the bundle flows plus bypass flow will equal the total core flow, WCT:

$$\left[\begin{matrix} \\ \end{matrix} \right] \quad (1.5.31)$$

1.5.2 Enthalpy-Quality Distribution Calculation

Once the flow into each channel has been determined, an energy balance up the channel is used to calculate enthalpy at each axial node. (See Figure 1-15 in Section 1.4.10 for axial nodalization). Quality is directly related to enthalpy. Similar calculations were required for each characteristic channel during the determination of flow distribution.

Figure 1-20 illustrates the geometry of a typical flow channel. The nodal energy balance for in-channel coolant flow accounts for the following components:

- (1) energy carried by coolant from the node below;
- (2) energy deposited in the coolant by heat flux through the fuel rod cladding;
- (3) energy absorbed by the coolant from neutron slowing down and gamma heating;
- (4) energy absorbed by the channel wall from neutron slowing down and gamma heating which is transferred to the coolant by conduction and convection and
- (5) energy transferred by convection and conduction from in-channel coolant to bypass coolant through the channel wall.

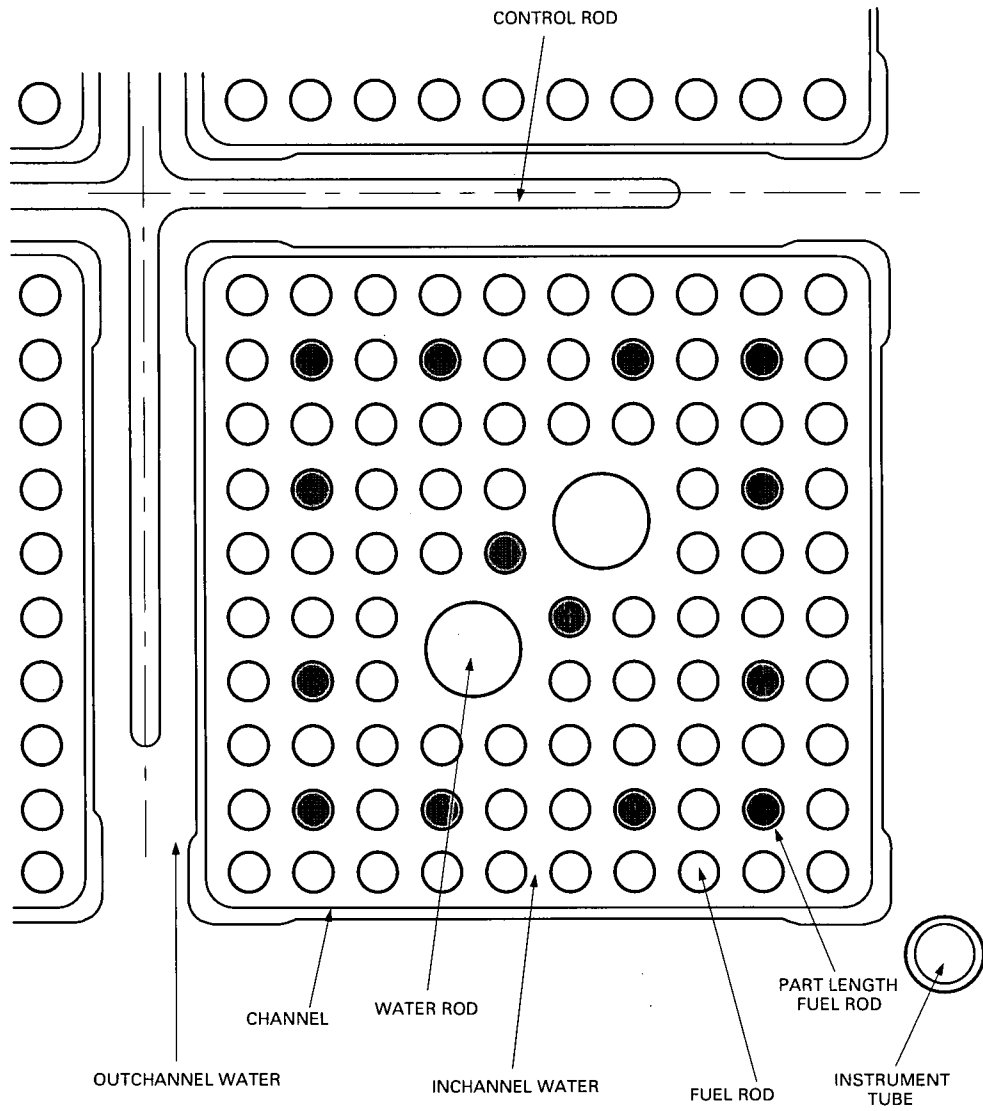


Figure 1-20. Flow Channel Geometry

The core inlet enthalpy (subcooling) is a given quantity. Neutron slowing-down and gamma heating factors are obtained from detailed X-Y physics calculations performed for lattice cells parametrically as a function of coolant density, control rod position (in or out), and lattice geometry.

The in-channel coolant energy and mass flows yield enthalpy h at axial level k . Flow quality at level k is given by:

$$X = \frac{h - h_\ell}{h_g - h_\ell} \quad (1.5.32)$$

where h_g is saturated vapor enthalpy and h_ℓ is bulk liquid enthalpy. The bulk liquid enthalpy calculation accounts for subcooled boiling effects and the bulk boiling limit, where h_ℓ is simply the saturated liquid enthalpy h_f . Vapor flow (boiling) is indicated whenever $X \geq 0$.

1.5.3 Void Distribution

The void fraction correlation and the subcooling model are described in this section. Using the general Zuber-Findlay expression for two-phase flow, the void fraction can be expressed as

$$\alpha = \frac{j_g}{C_o * j + \bar{V}_{gj}} \quad (1.5.33)$$

where

C_o	= distribution parameter
\bar{V}_{gj}	= drift velocity (lb/hr/ft ²)
j	= volumetric flux of mixture
j_g	= volumetric flux of vapor

The distribution parameter is correlated for low and high void fraction regions. The form of C_o is

$$[[\quad \quad \quad]] \quad (1.5.34)$$

where

γ	= ratio of saturated density, ρ_g/ρ_f
Re	= Reynold's number, $G * D_H / \mu_f$

The expressions for $f_1(\gamma)$, $f_2(Re)$, and $f_3(\alpha)$ are given in Table 1-7.

The drift velocity is correlated separately for three flow regions:

[[

(1.5.35)

(1.5.36)

]]

(1.5.37)

where

- σ = surface tension
- g = acceleration of gravity
- g_c = gravitational constant

The expressions for K_ℓ , K_g , α_2 , and $f_4(\text{Re})$ are given in Table 1-8.

Table 1-7. Correlating Functions For Distribution Parameter, C_0

[[

]]

Table 1-8. Correlating Functions For Drift Velocity, \bar{V}_{gi}

[[

]]

In the subcooled boiling region, the void fraction is correlated so as to vary the distribution parameter between zero at the incipience of significant void h_{ℓ,z_0} and Equation (1.5.34) for saturated liquid conditions. To account for subcooled boiling, the form of the distribution parameter is modified as follows:

$$[[\hspace{15em}]] \hspace{10em} (1.5.38)$$

The Saha-Zuber subcooled boiling model is used to predict the incipience of significant void. Table 1-9 gives the expressions for $\theta(h_{\ell})$, h_{ℓ,z_0} , h_{ℓ} , and the Saha-Zuber criterion.

$$[[\hspace{15em}]] \hspace{10em} (1.5.39)$$

$$(1.5.40)$$

$$(1.5.41)$$

]]

Table 1-9. Subcooled Boiling Correlating Functions

[[

]]

Table 1-10. Void Fraction Correlating Functions

[[
]]

Table 1-11. Void Fraction Correlating Functions (Continued)

[[
]]

implies that for each region the solution is given by

$$\alpha = \frac{-B - \sqrt{B^2 - 4AC}}{2A} \quad (1.5.42)$$

The void fraction given by Equation (1.5.42) depends upon the choice of coefficients K_1 , K_2 , K_3 and K_4 . Since these coefficients vary with void fraction, an iterative technique is employed in determining the void fraction.

1.5.4 Bypass Region Calculation

Thermal-hydraulics effects in the bypass flow region are modeled in a manner similar to the in-channel flow region. The following assumptions are used:

- (1) Coolant mixes uniformly in the bypass region; therefore, only one bypass flow region is considered. That is, the gaps between all fuel bundles (Figure 1-20) are lumped together to form one uniform flow region.
- (2) Inlet flow and enthalpy to the bypass region are given.
- (3) The average control rod fraction at level k is used to determine the bypass flow area and heating resulting from γ , (n,γ) , and (n,α) reactions in the control rods.
- (4) The temperature of water in the vessel annulus (downcomer) region is equal to the core inlet temperature.

As for in-channel coolant flow, a nodal energy balance is performed for the bypass coolant. The following components are considered:

- (1) energy carried by coolant from the node below;
- (2) energy absorbed by the coolant from neutron slowing down and gamma heating;
- (3) energy absorbed by the channel wall from neutron slowing down and gamma heating which is transferred to the coolant by conduction and convection;
- (4) energy transferred by convection and conduction from in-channel coolant to bypass coolant through the channel wall;
- (5) energy absorbed by control rods from γ , (n,γ) , and (n,α) reactions which is transferred to the coolant by conduction and convection and
- (6) energy transferred by convection and conduction from bypass coolant to water in the vessel annulus through the core shroud.

The energy contribution from heat generation in the core shroud and upper and lower core structures is ignored. This is compensated by neglecting energy losses due to neutron and gamma leakage from the core.

Once energy to the bypass coolant is determined, axial enthalpy, flow quality, and void distributions are calculated following the same procedure used for in-channel flow.

1.5.5 Total Core Energy Balance

When performing a BWR simulation, the total core power level is given. It is necessary to insure that the power absorbed by in-channel coolant and bypass coolant sums to the given total core power level.

Specifically, the neutron and gamma direct heating components of the nodal energy balances are expressed in terms of fuel rod heat flux through the cladding for each channel. For example, energy absorbed by the channel wall from neutron slowing down and gamma heating is given by the ratio of direct heating in the channel wall relative to cladding heat flux. Therefore, each direct heating component of the nodal energy balance is written as the product of cladding heat flux times the appropriate direct heating ratio. The cladding heat flux (more than 95% of the total core power) becomes a parameter which may be adjusted until the power deposited into the coolant equals the given total core power level. This adjustment is performed during the outer loop of the power-void iteration (Figure 1-14).

The power deposited into the coolant is found by adding in-channel and bypass portions:

$$P_C = \left[\sum_n (h_{e_n} - h_i) W_n \right] + (h_{e_b} - h_i) W_b \quad (1.5.43)$$

where n represents each flow channel, b represents the bypass region, h_i and h_e are inlet and exit enthalpy, respectively. The average cladding heat flux at node (i,j,k) is:

$$\bar{Q}_{i,j,k} = P_{ijk} \cdot P_C \cdot F_Q / S_{i,j} \quad (1.5.44)$$

$P_{i,j,k}$ = power distribution (normalized to 1.0)

F_Q = fraction of total power per channel which is transmitted by convection from fuel rod cladding to in-channel coolant

$S_{i,j}$ = cladding heat transfer surface area for the channel at (i,j)

F_Q is the parameter that is adjusted each power-void iteration until P_C is equal to the given total core power level.

1.5.6 Thermal Limits Calculation

Once the power-void iteration is converged, the nodal power distribution is in equilibrium with the distribution of feedback effects (moderator density, fuel temperature, xenon poisoning, and crud deposition). Detailed core performance characteristics may then be determined. Three important characteristics with respect to thermal performance limits are: (1) peak cladding heat flux; (2) maximum and average fuel rod linear heat generation rate; and (3) critical power ratio. The third quantity (CPR) expresses margin relative to boiling transition.

The nuclear model determines average power for each (i,j,k) node by Equation (1.4.42). For thermal limits evaluation, it is necessary to calculate the peak power within the node (i.e., the maximum fuel rod power within the bundle represented by the node).

The local peaking P_{lm} in a rod (l,m) is

$$P_{lm} = P_{lm}^{\infty} \Phi_3(x_l, y_m) / \bar{\Phi}_3 \quad (1.5.45)$$

where P_{lm}^{∞} is the infinite lattice local peaking factor, $\Phi_3(x_l, y_m)$ is the thermal flux at the position of rod (l,m) and $\bar{\Phi}_3$ is the average thermal flux. The thermal flux is calculated as a superposition of the partial fluxes in the two dimensions considered in the lattice physics solution:

$$\Phi_3(x, y) = \Phi_{3x}^+ e^{-x/M_3} + \Phi_{3x}^- e^{x/M_3} + \Phi_{3y}^+ e^{-y/M_3} + \Phi_{3y}^- e^{y/M_3} + \text{cross-terms} \quad (1.5.46)$$

[[

]] (1.5.47)

These reconstructed pin powers are then used to obtain the maximum rod peaking in a node.

From the three group flux estimates, the power of each node can be calculated explicitly. The exact expression for the nodal power is given in Equation (1.5.48):

$$P_i = \epsilon_i \sum_g \Sigma_{fgi} \bar{\phi}_{gi} \quad (1.5.48)$$

where ϵ_i is the conversion factor relating fissions to energy from the lattice physics calculation for the node, Σ_{fgi} is the nodal fission cross section and $\bar{\phi}_{gi}$ is the node averaged flux in group g

Peak cladding heat flux at node (i,j,k) is:

$$\hat{Q}_{i,j,k} = (P_{lm} \bar{Q})_{i,j,k} \quad (1.5.49)$$

where P_{lm} represents local peaking factor. The maximum and average fuel rod linear heat generation rates are:

$$LHGR_{i,j,k} = \hat{Q}_{i,j,k} O_{i,j} \quad (1.5.50)$$

and

$$\overline{LHGR}_{i,j,k} = \bar{Q}_{i,j,k} O_{i,j} \quad (1.5.51)$$

where O_{ij} is the heated perimeter per fuel rod for the channel at (i,j). It is assumed that each fuel rod in the bundle has the same O . Note that \overline{LHGR} given by Equation (1.5.50) is normally referred to as average planar linear hear generation rate (APLHGR).

The GE Thermal Analysis Basis (GETAB) [Reference 5] is used to identify thermal margin relative to boiling transition. The GEXL correlation predicts bundle average critical quality X_C by the general form:

$$X_C = X_C(L_B, L_A, D_Q, G, L, P, R) \quad (1.5.52)$$

where

L_B = boiling length;

L_A = annular flow length;

D_Q = thermal diameter [i.e., $4A/(\text{total rodded perimeter})$];

G = (W/A) = mass flux;

L = heated length;

P = system pressure; and

R = a parameter which characterizes the local peaking pattern within the bundle, lattice dimensions, and spacer configuration.

For each channel type, R is dependent upon channel average exposure and control configuration. Local peaking pattern data for R are obtained from the detailed lattice physics calculations. Critical power ratio (CPR) is defined as the ratio of bundle power which would yield X_C (boiling transition) relative to existing bundle power. As used here, the term bundle power is the total power absorbed by in-channel coolant for a particular channel.

1.6 THREE-DIMENSIONAL SIMULATOR MODEL QUALIFICATION

1.6.1 Introduction

The BWR Simulator model (PANAC11) in this report has been qualified against data obtained from numerical benchmarks and operating Boiling Water Reactors. The qualification studies consist of: (1) simulation comparisons to fine mesh 3D diffusion models; (2) simulation and tracking of nine operating cycles on three plants; and (3) cold critical measurements taken during seven cycles at two plants.

1.6.2 Fine Mesh Diffusion Comparison

The core simulator code was benchmarked against DIF3D, a fine mesh, 3 energy group diffusion theory code from Argonne National Laboratory. For the comparisons, both codes used the same set of cross sections from TGBLA06. The purpose of the comparison is to validate the coarse mesh diffusion theory of PANAC11 with an alternate calculation. This isolates the neutronics solution methods, rendering it separable from thermal-hydraulics and lattice physics considerations. The fine mesh code was run on the same spatial grid as the lattice physics code, with each fuel pin cell being a node in the 3D code. This comparison technique allows not only the eigenvalue and power distribution to be validated, but also serves as qualification of the pin power reconstruction model developed for PANAC11.

Figure 1-21 is a comparison of the core effective eigenvalue difference between that calculated by PANAC11 and the benchmark code DIF3D. There are 23 separate core configurations shown in these benchmark tests covering various loading patterns, exposure distributions and void distributions. The cases are denoted by a key letter that can be found in Table 1-12, a cycle number, the cycle exposure state (BOC=beginning of cycle, MOC=middle of cycle, EOC=end of cycle) and the core average void fraction. As can be seen from the figure, PANAC11 is in very good agreement with the benchmark code for eigenvalue calculation [[]] indicating that the PANAC11 neutronics solution is accurately reproducing the fine mesh 3D benchmark solution.

[[

]]

**Figure 1-21. Quarter Core Hot Benchmarks:
 Eigenvalue Difference between DIF3D and PANACEA**

Table 1-12. Plant Description for DIF3D Benchmark Study			
Plant Key	BWR Type	Lattice Type	No. of Bundles
A	ABWR	N	872
B	BWR/4	C	764
C	BWR/6	S	800
D	BWR/4	D	560
E	ABWR	N	872
F	BWR/4	D	240
G	BWR/4	C	764
H	BWR/5	C	764

The power calculation of PANAC11 is also compared to the fine mesh, 3 energy group diffusion theory code DIF3D. The spatial mesh for the DIF3D is the same as for the lattice code, TGBLA06. The results are shown in Figure 1-22 and Figure 1-23 below. Figure 1-22 is a plot of the RMS nodal power differences between the core simulator and the benchmark and Figure 1-23 is a plot of the peak to peak nodal power differences. Once again, cases are identified by plant key, cycle number and by void fraction. [[

]]

[[

]]

**Figure 1-22. Quarter Core Hot Benchmarks:
Nodal Power RMS Differences Between DIF3D and PANACEA**

[[

]]

**Figure 1-23. Quarter Core Hot Benchmarks:
Nodal Peak to Peak Power Differences Between DIF3D and PANACEA**

1.6.3 Gamma Scan Comparisons

Traversing in-core probe (TIP) signals are used, together with the core monitoring system, to monitor the three-dimensional power distribution in the reactor during operation. The TIP signals provide a good picture of the axial power distribution but do not provide a detailed measured bundle by bundle power distribution because there is only one TIP location for every 16 bundles. An alternate method for estimating the reactor power distribution just prior to a reactor shutdown independent of the core simulator can be obtained by the procedure known as gamma scanning. The gamma scan technique consists of removing the fuel bundles from the reactor core and measuring the gamma ray intensity as a function of axial position in the bundle. The gamma ray measured is the 1.596 MeV gamma ray that is produced by the decay of Lanthanum-140 (La^{140}).

The La^{140} comes from the beta decay of Ba^{140} , a fission product with a half-life of 12.79 days. The La^{140} has a half life of 1.68 days which provides an active mono-energetic gamma source which can be readily measured. Measurement of the La^{140} activity and correction for the Ba^{140} decay yields a relative Ba^{140} concentration as a function of position in the core just prior to shutdown. The Ba^{140} distribution, in turn, closely follows the actual power distribution.

Global gamma scan measurements have been performed at the end of Cycles 1 and 3 of Hatch 1. In each of the cases, roughly one-eighth of the bundles in the octant symmetric core were scanned. The relative concentration of Ba^{140} has been calculated by the 3D simulator using plant tracking calculations similar to the calculations shown in Section 1.6.4, using the power distributions calculated near the end of cycle coupled with the Ba^{140} decay equations. The overall nodal and bundle RMS differences are summarized in Table 1-13. [[

]]. These are excellent results and are perhaps better than nominal expectations.

The procedure used to evaluate the comparisons is as follows:

1. Evaluate of all lattice designs with lattice physics (TGBLA)
2. Exposure tracking to the end of cycle of interest using the core simulator (PANACEA)
3. Calculate estimated nodal relative Ba^{140} predictions using the power and exposure distributions from approximately the last sixty days of operation.
4. Correct the experimental nodal La^{140} (Ba^{140}) predictions for decay between shutdown and measurement.
5. Statistically compare the experimental and predicted Ba predictions.

The final step involves the following operations: (a) Read the nodal gamma scan data and simulator predictions; (b) Interpolate the gamma scan data if information is not available for every axial node; (c) Normalize the gamma scan data and simulator predictions given the portion of the core which was scanned; (d) Perform statistical comparisons between the data sets.

For all tables below, if g_i denotes the gamma scan data and p_i denotes the simulator prediction, "SIGMA" denotes the following relationship.

$$d_i = p_i - g_i$$

$$\bar{D} \equiv \frac{1}{N} \sum_{i=1}^N d_i$$

$$SIGMA = \sigma = \sqrt{\frac{1}{N-1} \sum_{i=1}^N (d_i - \bar{D})^2}$$

Table 1-13. Hatch 1 Gamma Scan Comparisons

Cycle Number	Bundle SIGMA	Nodal SIGMA
1	[[
3]]

For additional information, the PANAC11 bundle gamma scan comparisons for the primary quadrant analyzed in cycles 1 and 3 are presented in Figure 1-24 and Figure 1-25.

[[

]]

Figure 1-24. Bundle Gamma Scan Comparison for Cycle 1

[[

]]

Figure 1-25. Bundle Gamma Scan Comparison for Cycle 3

1.6.4 Plant Tracking Results

In plant tracking calculations, the 3D simulator (using cross sections generated from the lattice physics model) is used to simulate the behavior of a plant during operation. The reactor power, flow and pressure are input to the simulator, which then calculates the core keff and power distributions as a function of cycle exposure. The operating reactor is critical; hence, the calculated keff is compared to 1.0. Accurate and technically well-founded simulators should calculate a keff close to 1.0 and the difference between keff and 1.0 should not vary appreciably from plant to plant or as a function of fuel exposure. Consistency of keff bias ensures that accurate cycle length estimates will be obtained in future core designs. Occasional, random deviations due to variations in plant data or to non-equilibrium conditions may occur which are as large as two or three standard deviations. This is to be expected and should not detract from the generally good agreement.

Five plants were studied to evaluate eigenvalue trends during plant operation. The plant characteristics are identified in Table 1-14. The summary of all cycles studied for the identified plants can be seen in Figure 1-26. A detailed summary of the plant tracking results for Plant A Cycle 18 is provided as additional information in Table 1-15. Results available in Table 1-15 include the core power, core flow, power density, core average exit void fraction, maximum channel exit void fraction, thermal margins, and hot critical eigenvalue as a function of cycle exposure. These data are taken directly from the core tracking analyses, and are based solely on

calculations performed by the nuclear methods. There is no adaption to the core monitoring data included in these results.

Figure 1-26 indicates that the simulation of the reactor core is well behaved as a function of plant type, cycle length, and fuel design type. [[

]]. The consistency of the tracking results is key to the overall performance of the simulations system.

Table 1-14. Key Core Parameters for Reference Plants

Plant	GE BWR Type	Number of Bundles	Original Licensed Thermal Power (OLTP) MWt	Rated Flow (Flow at OLTP) Mlbm/hr	Licensed Power Uprate (PU) % OLTP	Licensed Core Flow Range at PU % Rated Flow	Power Density at Licensed PU kW/l
A	BWR/4	368	1593	49.0	120	99-100	58.7
B	BWR/6	748	3579	104.0	105	81-105	56.8
C	BWR/4	240	997.2	29.7	110	87-111	51.7
D	BWR/4	560	2436	77.0	120	99-105	59.0
E	BWR/6	624	2894	84.5	120	99-107	62.9

[[

]]

Figure 1-26 Hot Critical Eigenvalue for Studied BWR Cycles

Table 1-15. Exposure Accounting Data for Plant A, Cycle 18

Cycle Expo.	Core Power	Core Flow	Power Density	Avg. Core Exit Void Fract.	Max. Chan. Exit Void Fract.	MFLCPR	MFLPD	MAPRAT	Hot Critical Eigenvalue
GWd/ST	% OLTP	% Rated	kW/l						
0.02	34.1	55.3	16.7	0.54	0.66	[[
0.03	60.8	55.7	29.7	0.70	0.77				
0.17	77.9	79.2	38.1	0.70	0.77				
0.21	82.7	63.5	40.4	0.75	0.83				
0.34	104.2	98.1	51.0	0.73	0.81				
0.37	48.2	57.8	23.6	0.63	0.71				
0.38	83.7	65.6	40.9	0.75	0.82				
0.41	104.1	97.0	50.9	0.74	0.81				
0.72	104.0	96.9	50.9	0.73	0.81				
0.75	55.2	57.4	27.0	0.67	0.74				
0.78	104.1	94.9	50.9	0.74	0.82				
1.05	104.0	95.2	50.8	0.74	0.82				
1.16	103.9	93.2	50.8	0.74	0.82				
1.21	103.9	93.4	50.8	0.74	0.82				
1.25	89.0	72.2	43.5	0.75	0.83				
1.26	50.5	56.2	24.7	0.65	0.73				
1.28	103.7	97.8	50.7	0.73	0.81				
1.44	103.9	96.1	50.8	0.74	0.81				
1.61	104.1	94.6	50.9	0.74	0.82				
1.64	86.9	71.2	42.5	0.74	0.84				
1.66	103.9	97.8	50.8	0.73	0.83				
1.91	104.0	95.2	50.9	0.73	0.84				
2.14	104.1	94.5	50.9	0.74	0.84				
2.34	104.0	93.1	50.9	0.74	0.84				
2.66	104.1	93.6	50.9	0.74	0.84				
2.73	104.0	92.5	50.9	0.74	0.84				
3.04	104.0	93.3	50.9	0.74	0.84				
3.06	47.1	76.6	23.1	0.56	0.71				
3.07	50.0	68.4	24.5	0.59	0.74				
3.09	99.2	85.6	48.5	0.74	0.85				
3.21	103.8	96.2	50.8	0.73	0.84				
3.37	104.1	95.9	50.9	0.73	0.84				
3.41	103.8	95.6	50.8	0.73	0.84				
3.43	72.6	73.8	35.5	0.69	0.79				
3.45	94.2	75.1	46.1	0.75	0.86				
3.47	100.4	85.8	49.1	0.74	0.85				
3.51	104.0	92.4	50.8	0.74	0.85				
3.55	98.1	81.3	48.0	0.75	0.86				
3.57	104.0	91.8	50.8	0.74	0.85				
3.60	107.8	94.4	52.7	0.75	0.85				
3.69	110.5	95.6	54.0	0.75	0.86				

Table 1-15. Exposure Accounting Data for Plant A, Cycle 18

Cycle Expo.	Core Power	Core Flow	Power Density	Avg. Core Exit Void Fract.	Max. Chan. Exit Void Fract.	MFLCPR	MFLPD	MAPRAT	Hot Critical Eigen-value
3.96	112.3	96.0	54.9	0.75	0.86				
4.50	111.7	94.5	54.6	0.75	0.86				
4.63	112.4	95.6	55.0	0.75	0.86				
4.64	59.9	61.3	29.3	0.67	0.77				
4.67	112.1	97.9	54.8	0.75	0.86				
4.96	111.0	98.6	54.3	0.74	0.86				
5.25	111.1	96.6	54.3	0.74	0.86				
5.26	53.1	49.8	26.0	0.67	0.78				
5.28	94.0	72.8	46.0	0.76	0.85				
5.31	111.0	93.2	54.3	0.75	0.85				
5.57	111.0	95.4	54.3	0.75	0.84				
5.77	111.0	94.1	54.3	0.75	0.85				
5.94	111.1	93.1	54.3	0.75	0.85				
6.13	111.0	96.4	54.3	0.75	0.84				
6.15	89.1	80.6	43.6	0.72	0.84				
6.17	108.7	88.6	53.1	0.76	0.85				
6.37	112.2	95.1	54.9	0.75	0.85				
6.57	112.2	94.4	54.9	0.75	0.85				
6.91	112.2	96.6	54.9	0.75	0.85				
7.16	112.3	94.7	54.9	0.75	0.85				
7.18	112.3	94.6	54.9	0.75	0.86				
7.40	112.5	96.6	55.0	0.75	0.86				
7.62	112.3	94.9	54.9	0.75	0.86				
7.82	112.4	93.8	55.0	0.75	0.86				
7.85	112.4	96.6	55.0	0.75	0.86				
7.88	76.2	64.9	37.3	0.72	0.85				
7.90	111.0	90.1	54.3	0.75	0.87				
7.92	112.3	95.9	54.9	0.75	0.86				
8.14	112.2	94.2	54.9	0.75	0.86				
8.42	112.4	93.7	55.0	0.75	0.87				
8.64	112.1	96.2	54.8	0.74	0.86				
8.86	112.3	95.6	54.9	0.75	0.86				
9.10	112.4	94.6	55.0	0.75	0.87				
9.13	111.2	98.2	54.4	0.74	0.86				
9.15	112.2	96.7	54.9	0.74	0.86				
9.42	112.3	95.3	54.9	0.75	0.87				
9.68	112.5	95.3	55.0	0.75	0.87				
9.69	47.3	60.4	23.1	0.57	0.77				
9.72	109.8	91.2	53.7	0.75	0.87				
9.74	112.2	95.2	54.9	0.75	0.87				
10.06	112.2	93.9	54.9	0.75	0.87				
10.09	109.2	94.6	53.4	0.74	0.86				
10.11	66.8	65.0	32.7	0.68	0.83				

Table 1-15. Exposure Accounting Data for Plant A, Cycle 18

Cycle Expo.	Core Power	Core Flow	Power Density	Avg. Core Exit Void Fract.	Max. Chan. Exit Void Fract.	MFLCPR	MFLPD	MAPRAT	Hot Critical Eigen-value
10.13	78.8	89.9	38.5	0.66	0.82				
10.18	77.8	59.5	38.1	0.73	0.86				
10.20	80.4	71.1	39.3	0.72	0.85				
10.22	112.4	94.1	55.0	0.75	0.87				
10.35	112.3	97.3	54.9	0.74	0.86				
10.62	112.2	96.0	54.9	0.74	0.86				
10.79	112.2	94.1	54.9	0.75	0.86				
11.01	112.3	95.4	54.9	0.75	0.86				
11.03	67.4	68.5	33.0	0.67	0.80				
11.04	77.2	67.9	37.8	0.71	0.83				
11.07	109.7	89.9	53.7	0.75	0.87				
11.26	112.5	97.1	55.0	0.74	0.85				
11.49	112.2	94.0	54.9	0.75	0.86				
11.71	112.3	96.3	54.9	0.74	0.85				
11.90	112.4	94.1	55.0	0.75	0.86				
12.13	112.3	96.8	54.9	0.74	0.85				
12.35	112.3	93.7	54.9	0.75	0.85				
12.57	112.4	97.1	55.0	0.74	0.85				
12.69	112.4	96.0	55.0	0.74	0.85				
12.91	112.4	97.0	55.0	0.74	0.86				
13.23	112.5	96.0	55.0	0.74	0.86				
13.25	84.6	73.8	41.4	0.72	0.85				
13.28	112.5	94.5	55.0	0.74	0.87				
13.37	112.4	97.7	55.0	0.74	0.86				
13.58	112.5	95.7	55.0	0.74	0.86				
13.59	71.2	53.6	34.8	0.73	0.85				
13.62	104.5	99.2	51.1	0.72	0.85				
13.64	112.2	97.7	54.9	0.74	0.86				
13.89	112.3	93.4	54.9	0.74	0.87				
13.98	112.3	96.8	54.9	0.74	0.86				
14.08	112.1	96.9	54.8	0.74	0.86				
14.16	112.4	98.1	55.0	0.73	0.86				
14.23	112.3	98.1	54.9	0.73	0.86				
14.30	112.4	98.7	55.0	0.73	0.86				
14.35	112.2	98.3	54.9	0.73	0.86				
14.45	112.3	98.3	54.9	0.73	0.86]]

1.6.5 Cold Critical Measurements

BWRs are designed so that they can be shut down in the cold condition (20°C) with a single control rod or rod pair withdrawn. In order to qualify the ability of the BWR simulator code to accurately predict the cold shutdown margin, a number of cold critical data points have been tabulated.

Cold critical eigenvalue data for each of the cycles studied is provided in Table 1-16. The studied plants are identified in Table 1-14. Cold critical data is provided for each point in the cycle where a cold critical test was performed. Table 1-16 shows the cycle exposure at which the test was performed, the measured cold critical eigenvalue, and the design basis eigenvalue which was selected for design purposes prior to operation. The design basis eigenvalues are selected by the responsible design engineer and are based on the prior history of the particular plant and known trends of the nuclear methods used for design. Figure 1-27 shows the cold critical eigenvalues as a function of cycle exposure. [[

]]. The trend is consistent and is accounted for in the design process.

The measured cold critical eigenvalues are obtained by running the 3D Simulator at the same exposure and with the critical rod patterns used in the test. The eigenvalue calculated by the simulator is then corrected for the positive period measured during the test. The data in Table 1-16 include both distributed control rod patterns (as would occur during normal startup or shutdown) and local criticals where control rod(s) are withdrawn in a particular core location. Note that the design basis cold eigenvalue is not provided for Plant B, Cycle 9, and Plant E, Cycle 9. The reason for this exception is that when these cycles were being designed, PANAC10 was used, but the analysis of the test was performed with PANAC11. Therefore, the actual design basis eigenvalue was based on the earlier version of the 3D Simulator, and it would not be valid to compare it to the PANAC11-based measured eigenvalue.

The results of this sample of cold critical results are summarized in Table 1-16. [[

]]. This sample indicates that the core simulation system is capable of providing excellent predictive capability over a wide range of plants and core designs. The uncertainty in the results is consistent with expectations and in addition to the nuclear methods uncertainty includes all other uncertainties (i.e. plant instrumentation, manufacturing, etc) associated with the design and operation of a nuclear reactor.

Table 1-16. Cold Critical Eigenvalues for All Studied Cycles			
Plant, Cycle	Cycle Exposure GWD/ST	Measured Cold Critical Eigenvalue	Nuclear Design Basis Cold Critical Eigenvalue
Plant A, C18	0.00	[[
	3.04		
	6.13		
	7.85		
	9.68		
	13.58		
	13.58		
Plant A, C19	0.00		
	4.80		
	4.87		
	4.88		
Plant B, C9	0.00		
	11.86		
Plant B, C10	0.00		
	0.00		
	8.68		
Plant C, C30	0.00		
	0.00		
	0.00		
	0.00		
	6.34		
	7.60		
	7.60		
	7.60		
	7.60		
	7.60		
Plant C, C31	0.00		
	0.00		
	0.00		
	0.00		
	0.00		
	0.00		
	0.00		
	0.00		
	0.00		
	0.00		
	7.83		
	7.83		
	7.83		
7.83]]	

Table 1-16. Cold Critical Eigenvalues for All Studied Cycles			
Plant, Cycle	Cycle Exposure GWD/ST	Measured Cold Critical Eigenvalue	Nuclear Design Basis Cold Critical Eigenvalue
Plant D, Cycle15	0.00	[[
	3.4		
Plant E, Cycle 9	0.00		
Plant E, Cycle 10	0		
	3.4		
Average			
Standard Deviation]]

NOTE: PANAC10 was used to design both of these cycles, using PANAC10-based eigenvalues for the Nuclear Design Basis. The tests, however, were evaluated with PANAC11, for which there were no Nuclear Design Basis eigenvalues defined.

[[

]]

Figure 1-27. Cold Critical Eigenvalues for All Cycles Studied

1.6.6 TIP Data Summary for the Cycles Studied

Summary core-wide statistics for the TIP data taken during the cycles studied is provided in Table 1-17. This table provides the cycle exposure at which the TIP data was taken, the core power and flow, the RMS differences between the TIP data and the power distribution calculated by the 3D Simulator, the core average and maximum channel exit void fractions, and the thermal margins calculated by the 3D Simulator at each of the TIP state points. The RMS differences are calculated for the Bundle (Radial), Axial and Nodal quantities at each state point. [[

]]. This shows excellent overall agreement and does not indicate any degradation of the simulation as a function of cycle exposure or core design.

Table 1-17. TIP Comparisons for the Studied Cycles										
Cycle Expo.	Core Power	Core Flow	Bundle RMS	Axial RMS	Nodal RMS	Avg.Core Exit Void Fract	Max Chan. Exit Void Fract	MFLCPR	MFLPD	MAPRAT
GWd/ST	%OLTP	% Rated	%	%	%					
Plant A – Cycle 18										
2.34	104.0	93.6	[[0.74	0.84	[[
3.37	103.4	94.2				0.73	0.84			
4.18	112.2	94.4]]	0.75	0.86]]
Plant A – Cycle 19										
0.24	112.4	94.8	[[0.76	0.83	[[
1.17	112.5	92.8				0.76	0.83			
2.13	112.4	94.3				0.76	0.84			
2.50	112.3	95.4				0.75	0.85			
3.16	112.3	96.9				0.75	0.85			
4.19	112.5	93.6				0.76	0.86			
4.51	112.2	97.6				0.75	0.84			
5.18	112.5	97.9				0.75	0.84			
6.26	112.3	94.4				0.76	0.85			
7.22	112.4	94.4				0.75	0.86			
8.13	112.6	94.3				0.75	0.86			
9.02	112.6	96.0]]	0.75	0.86]]
Plant B – Cycle 9										
0.26	104.8	99.4	[[0.74	0.83	[[
0.54	104.9	90.6				0.76	0.84			
0.79	104.9	91.1				0.76	0.84			
1.42	104.8	96.9				0.74	0.83			
1.61	105.0	94.9				0.75	0.84			
2.20	104.6	89.7				0.76	0.85			

Table 1-17. TIP Comparisons for the Studied Cycles

Cycle Expo.	Core Power	Core Flow	Bundle RMS	Axial RMS	Nodal RMS	Avg.Core Exit Void Fract	Max Chan. Exit Void Fract	MFLCPR	MFLPD	MAPRAT
GWd/ST	%OLTP	% Rated	%	%	%					
2.50	104.9	89.7				0.76	0.86			
3.41	104.6	85.7				0.76	0.87			
3.87	104.6	85.0]]	0.76	0.87]]
4.39	105.0	92.1	[[0.75	0.86	[[
5.92	104.7	87.6				0.76	0.86			
6.92	105.1	86.4				0.76	0.87			
7.20	105.0	98.0				0.74	0.86			
7.76	104.9	95.5				0.74	0.86			
8.49	105.0	92.9				0.75	0.87			
9.20	105.0	91.0				0.75	0.87			
9.58	96.8	103.9				0.70	0.82			
10.06	105.1	100.6				0.73	0.85			
10.34	104.8	99.6				0.73	0.85			
11.12	105.1	99.5				0.73	0.85			
12.00	101.1	103.3				0.71	0.85			
13.21	104.6	101.3				0.72	0.85			
13.71	104.8	93.1				0.74	0.87			
14.24	104.9	97.2				0.73	0.86			
14.49	104.1	102.9				0.72	0.84			
14.76	104.6	102.1				0.72	0.85			
15.21	102.8	104.1				0.71	0.84			
15.63	88.1	103.5				0.67	0.81			
15.99	89.2	103.6]]	0.67	0.81]]
Plant B – Cycle 10										
0.19	94.1	102.7	[[0.70	0.80	[[
0.27	104.5	102.1				0.73	0.83			
0.80	105.0	98.1				0.74	0.84			
1.64	104.9	96.9				0.74	0.84			

Table 1-17. TIP Comparisons for the Studied Cycles

Cycle Expo.	Core Power	Core Flow	Bundle RMS	Axial RMS	Nodal RMS	Avg.Core Exit Void Fract	Max Chan. Exit Void Fract	MFLCPR	MFLPD	MAPRAT
GWd/ST	%OLTP	% Rated	%	%	%					
2.45	105.0	96.7				0.74	0.85			
4.10	104.9	92.3				0.75	0.85			
4.18	105.0	92.6				0.75	0.85			
4.46	104.9	95.6]]	0.74	0.85]]
5.01	104.9	95.5	[[0.74	0.86	[[
5.77	104.9	94.0				0.74	0.86			
6.61	104.9	93.0				0.74	0.87			
7.08	104.8	97.4				0.73	0.86			
7.92	104.9	95.4				0.74	0.87			
8.20	105.1	95.4				0.74	0.87			
8.68	105.0	92.3]]	0.74	0.88]]
Plant C – Cycle 30										
0.43	110.0	98.2	[[0.71	0.88	[[
1.13	109.8	97.7				0.71	0.87			
1.85	109.8	94.7				0.71	0.88			
2.25	109.5	93.8				0.72	0.89			
2.53	109.8	93.4				0.72	0.89			
3.33	109.7	94.5				0.72	0.87			
3.84	109.9	88.6				0.73	0.90			
4.01	109.9	90.2				0.73	0.90			
4.71	109.5	98.9				0.71	0.88			
5.34	106.7	87.0				0.72	0.90			
6.25	109.5	105.7				0.68	0.87			
6.48	94.3	88.5				0.68	0.87			
6.91	105.1	109.8				0.65	0.85			
Plant C – Cycle 31										
0.50	103.7	87.7				0.72	0.88			

Table 1-17. TIP Comparisons for the Studied Cycles

Cycle Expo.	Core Power	Core Flow	Bundle RMS	Axial RMS	Nodal RMS	Avg.Core Exit Void Fract	Max Chan. Exit Void Fract	MFLCPR	MFLPD	MAPRAT
GWd/ST	%OLTP	% Rated	%	%	%					
0.98	110.2	97.8				0.72	0.87			
1.68	110.0	93.7				0.72	0.87			
2.45	109.9	92.3				0.72	0.87			
3.10	109.7	93.0				0.72	0.87			
3.92	109.9	94.8				0.72	0.87			
4.61	109.6	90.9]]	0.72	0.88]]
5.38	109.6	99.1	[[0.71	0.87	[[
5.86	109.7	90.1				0.72	0.90			
6.72	109.5	107.8				0.68	0.86			
7.28	109.3	109.2]]	0.66	0.85]]
Plant E – Cycle 9										
0.25	111.1	92.6	[[0.75	0.87	[[
0.51	111.2	98.2				0.74	0.86			
3.72	111.7	94.0				0.76	0.86			
3.77	111.6	94.7				0.75	0.86			
4.78	109.8	92.5				0.75	0.86			
5.69	109.5	90.9				0.76	0.87			
7.54	109.3	90.8				0.76	0.87			
9.31	109.5	92.5				0.76	0.87			
10.20	111.5	93.7				0.76	0.87			
11.03	112.0	94.6				0.76	0.87			
11.98	112.2	95.0				0.76	0.86			
12.91	109.0	94.0				0.75	0.86			
14.62	106.0	103.2				0.73	0.82			
15.40	100.8	104.3]]	0.70	0.80]]
Plant E – Cycle 10										
0.14	111.7	95.4	[[0.76	0.84	[[

Table 1-17. TIP Comparisons for the Studied Cycles

Cycle Expo.	Core Power	Core Flow	Bundle RMS	Axial RMS	Nodal RMS	Avg.Core Exit Void Fract	Max Chan. Exit Void Fract	MFLCPR	MFLPD	MAPRAT
GWd/ST	%OLTP	% Rated	%	%	%					
0.79	111.0	93.9				0.76	0.84			
1.71	113.5	95.6				0.77	0.85			
2.47	114.6	96.6				0.76	0.85			
3.58	114.2	96.2				0.77	0.86			
5.73	113.8	97.5				0.76	0.85			
6.58	113.3	96.6				0.76	0.85			
7.38	113.9	95.9				0.77	0.86			
8.45	110.8	95.8]]	0.76	0.86]]

1.6.7 Conclusions

The GE BWR Simulator has undergone extensive testing by comparison of calculated results with alternate three dimensional methods, end-of-cycle gamma scan data and operating reactor data.

Comparisons to alternate three dimensional methods indicates good agreement over a wide range of plant types and core conditions.

A further indication of the GE nuclear design methods ability to track operating plants is the comparison of calculated results to gamma scan measurements. Gamma scan measurements were taken at the end of two cycles of operation at Hatch Unit 1. [[

]]

Hot critical effective multiplication factors (k_{eff}) have been tracked for a number of plants at different exposure points and for different operating cycles. [[

]] The results indicate that the GE nuclear design models track core reactivity very well.

Cold critical effective multiplication factors have been calculated and compared to a number of measured critical core configurations. [[

]] These results indicate that the GE nuclear design methods track the cold k_{eff} very well.

Numerous examples of the ability of the GE nuclear design models to track the core power distributions are given. Comparisons to in-core plant instrumentation indicates good agreement over numerous cycles of operation for various plant types. The calculated results show that the GE methods track the measured (by the core monitoring system) core radial power distributions very well.

These results show that the GE BWR simulator is a valid and accurate predictor of BWR behavior and is suitable for performing the nuclear safety analyses for BWRs.

1.7 REACTIVITY COEFFICIENT METHODS

The Doppler reactivity coefficient is determined by using an NRC-approved lattice physics code. The Doppler coefficient is determined using the theory and methods for steady-state nuclear calculations, described above.

The lattice physics code is used to calculate k_{∞} for any lattice at two temperatures. The first temperature is the standard hot operating temperature. The second temperature is set at 1773K. The calculations are made at as a function of void fraction and at every standard hot uncontrolled exposure depletion point.

The Doppler Reactivity Coefficient (DRC) is characterized as CDOP as follows:

$$CDOP = \frac{1000(k_{T_1} - k_{T_0})}{k_{T_0} (\sqrt{T_1} - \sqrt{T_0})}$$

where:

- T_0 = normal hot operating temperature (Kelvin)
- T_1 = elevated temperature (Kelvin)
- k_{T_1} = eigenvalue at elevated temperature
- k_{T_0} = eigenvalue at normal operating temperature.

While the reactivity change caused by the Doppler effect is small compared to the moderator void reactivity changes during normal operation, it becomes very important during postulated rapid power excursions in which large fuel temperature changes occur.

The 3D core simulator is used in determining the void coefficient of reactivity. A detailed discussion of the methods used to calculate moderator void reactivity coefficients, the accuracy and application to plant transient analyses, is presented in Reference 9. The In-Channel Void Coefficient (VODCOF) is the ratio of the change in k-effective to the change in (percent) void fraction because of a perturbation in some particular parameter:

$$VODCOF = \frac{1}{k} \frac{\partial k}{\partial (\%VOID)}$$

The calculation of the void reactivity coefficient is accomplished through perturbation of the inlet enthalpy to the core, although perturbation of pressure or core flow are also possible to effect a change in voids and reactivity. The derivative in the above equation is determined by a higher-order numerical scheme, which requires two points above and two points below the base point in addition to the base point itself. After evaluating four perturbations to the original system, one obtains a better estimate than any of the original four approximate derivatives. This type of evaluation is subsequently less sensitive to the type and size of the perturbation for evaluation of a particular derivative.

The moderator temperature coefficient (MODCOF) is calculated using a combination of the lattice physics code and core simulator. The lattice physics code is used to evaluate infinite lattice properties of each of the various lattices in the fuel bundle as a function of exposure, void history and temperature. Introducing the temperature specific nuclear libraries from the lattice physics code into the core simulator and performing a standard cold eigenvalue calculation then simulates a core temperature change. From the differential in core eigenvalue, the moderator temperature coefficient of reactivity may be obtained as:

$$MODCOF = \frac{1}{k} \frac{\partial k}{\partial (^\circ K)}$$

2. NUCLEAR DESIGN BASES

The design bases are those that are required for the plant to operate, meeting all safety requirements. The safety design bases that are required fall into two categories:

- The reactivity basis, which prevents an uncontrolled positive reactivity excursion, and
- The overpower bases for the control of power distribution, which prevent the core from operating beyond the fuel integrity limits.

2.1 NEGATIVE REACTIVITY FEEDBACK BASES

Reactivity coefficients, the differential changes in reactivity produced by differential changes in core conditions, are useful in calculating stability and evaluating the response of the core to external disturbances. The base initial condition of the system and the postulated initiating event determine which of the several defined coefficients are significant in evaluating the response of the reactor. The coefficients of interest are the Doppler coefficient, the moderator void reactivity coefficient and the moderator temperature coefficient. Also associated with the BWR is a power reactivity coefficient. The power coefficient is a combination of the Doppler and void reactivity coefficients in the power operating range; this is not explicitly evaluated. The Doppler coefficient, the moderator void reactivity coefficient and the moderator temperature coefficient of reactivity shall be negative for power operating conditions, thereby providing negative reactivity feedback characteristics.

The above design basis meets General Design Criterion 11.

2.2 CONTROL REQUIREMENTS (SHUTDOWN MARGINS)

The core must be capable of being made subcritical, with margin, in the most reactive condition throughout the operating cycle with the highest worth control rod, or rod pair, stuck in the full-out position and all other rods fully inserted. This satisfies General Design Criterion 26.

2.3 CONTROL REQUIREMENTS (OVERPOWER BASES)

The nuclear design basis for control requirements is that Maximum Linear Heat Generation Rate (MLHGR) and Minimum Critical Power Ratio (MCPR) constraints shall be met during operation. The MCPR and MLHGR are determined such that, with 95% confidence, the fuel does not exceed required licensing limits during abnormal operational occurrences.

These parameters are defined as follows:

2.3.1 Maximum Linear Heat Generation Rate

The MLHGR is the maximum linear heat generation for the fuel rod with the highest surface heat flux at a given nodal plane in the bundle. The MLHGR operating limit is bundle type dependent. The MLHGR can be monitored to assure that all mechanical design requirements are met. The fuel will not be operated at MLHGR values greater than those found to be acceptable within the

body of the safety analysis under normal operating conditions. Under abnormal conditions, including the maximum overpower condition, the MLHGR will not cause fuel melting or cause the stress and strain limits to be exceeded.

2.3.2 Minimum Critical Power Ratio

The MCPR is the minimum CPR allowed for a given bundle type to avoid boiling transition. The CPR is a function of several parameters; the most important are bundle power, bundle flow, the local power distribution and the details of the bundle mechanical design. The plant Operating Limit MCPR (OLMCPR) is established by considering the limiting anticipated operational occurrences (AOOs) for each operating cycle. The OLMCPR is determined such that 99.9% of the rods avoid boiling transition during the transient of the limiting analyzed AOO.

The above basis satisfies General Design Criterion 10.

2.4 CONTROL REQUIREMENTS (STANDBY LIQUID CONTROL SYSTEM)

GDC 27 requires that the reactivity control systems have a combined capability, in conjunction with poison addition by the emergency core cooling system, of reliably controlling reactivity changes under postulated accident conditions, with appropriate margin for stuck rods. The nuclear design basis is that, assuming a stuck rod, or rod pair, the SLCS provide sufficient liquid poison into the system so that sufficient shutdown margin is achieved.

2.5 STABILITY BASES

The licensing basis for stability must comply with the requirements of 10 CFR 50, Appendix A, "General Design Criteria for Nuclear Power Plants". The Appendix A criteria related to stability are Criteria 10 and 12.

Criterion 10 (Reactor Design) requires that:

"The reactor core and associated coolant, control, and protection systems shall be designed with appropriate margin to assure that specified acceptable fuel design limits are not exceeded during any condition of normal operation, including the effects of anticipated operational occurrences."

Criterion 12 (Suppression of Reactor Power Oscillations) requires that:

"The reactor core and associated coolant, control, and protection systems shall be designed to assure that power oscillations which can result in conditions exceeding specified acceptable fuel design limits are not possible or can be reliably and readily detected and suppressed."

3. BUNDLE NUCLEAR DESIGN EVALUATION

3.1 INTRODUCTION

ESBWR bundle and lattice designs have been developed using the methodology and codes described in Section 1. This section presents the GE14E bundles that have been designed for equilibrium core operation. An equilibrium core design is defined as having a similar discharge of burnt fuel, a similar loading pattern of fresh fuel and a similar set of rod patterns that deplete the core in a consistent manner over multiple simulated cycles. The proposed GE14E bundles have been designed to achieve the desired distribution of power in both radial and axial directions, thereby meeting the key design bases that were discussed in Section 2.

3.2 BUNDLE AND LATTICE DESIGNS

A total of two unique GE14E bundle designs have been developed for the ESBWR reference equilibrium core. Each bundle design is comprised of several unique lattice configurations as shown below. These bundle designs are described in Figures 3-1 through 3-8. The figures include the 2-D pin-by-pin enrichment array for each lattice, axial profiles for each unique rod type, the axial location of each lattice within the bundle and the splits and weights for each bundle.

Bundle Number	Bundle Name	Number of Lattices	Lattice Numbers
3194	[[
3195]]

Many factors are considered in the development of these bundle designs in addition to overall cycle energy requirements and operating strategy. Perhaps the key considerations are given to achieving the desired reactivity and local peaking behavior required for an equilibrium core application. Acceptability of the designs can be confirmed when the overall performance is assessed by 3-D simulator evaluations using the methodology and codes discussed in Section 1. Lattice reactivity characteristics can be judged by the core hot excess reactivity and cold shutdown margin behavior. Lattice k-infinities versus burn-up for the hot uncontrolled condition at three void history fractions have been provided in Tables 3-1 through 3-9 and in Figures 3-9 through 3-17 for each lattice design. Similarly, lattice local peaking characteristics can be judged by the thermal margin performance as determined by 3-D simulator calculations. The maximum lattice local peaking versus burn-up for the hot uncontrolled condition at the same void history fractions are provided in Tables 3-10 through 3-18 and in Figures 3-18 through 3-26 for each lattice design. Core reactivity and thermal margin performance results based on these bundle

designs will be presented in Section 4. Acceptable core performance is strongly dependent on the k-infinity and local peaking characteristics at the bundle and lattice design level.

3.2.1 GE14E Bundle Design Features for Equilibrium Core

As previously mentioned, each GE14E bundle designed for the reference equilibrium core consists of several unique lattice configurations. The top and bottom lattice of each bundle consists of a blanket of natural uranium (NAT at the bottom and N-T at the top). The first enriched lattice above the bottom natural uranium zone is referred to as the "dominant" zone (DOM). This lattice represents the largest zone within the bundle and establishes the overall reactivity characteristics. For some reload applications, the GE14E design may include a shorter power shaping zone as the first enriched zone at the bottom. However, a more simplified design that excluded the power shaping zone was chosen for this application. The remaining lattices above the dominant zone correctly model the axially varying geometry (i.e., plenums, PLE, and vanishing rods, VAN) that is associated with the part length rod features of the GE14E design.

3.2.2 Bundle Local Peaking

One of the important parameters affecting linear heat generation rate (LHGR) performance of a bundle is the local peaking value. Figures 3-27 and 3-28 provide the 2-D pin-by-pin lattice local peaking values for each dominant lattice at 40% void history fraction and beginning of life (BOL) conditions. These data are provided in addition to the maximum lattice local peaking versus burn-up data discussed above. The resulting core LHGR performance based on a roddeed depletion scenario is described in Section 4.

3.2.3 Bundle R-Factor

An important parameter affecting the critical power performance of a BWR is the exposure dependent bundle R-factor. Tables 3-19 and 3-20 show the fully uncontrolled and fully controlled R-factors for zero mils channel bow as a function of burn-up for each equilibrium bundle design. To further illustrate how these maximum values are derived, the 2-D pin-by-pin R-factors for each bundle are shown in Figures 3-29 and 3-30 at 20 GWd/ST for the fully uncontrolled condition and zero mils channel bow. In general, the bundle design for an ESBWR attempts to achieve optimum thermal margins (i.e., MLHGR and MCPR) by minimizing local peaking and R-factors. The resulting core MCPR performance based on a roddeed depletion scenario is described in Section 4.

3.2.4 Doppler Reactivity Coefficient

The Doppler coefficient is a measure of the reactivity change associated with an increase in the absorption of resonance-energy neutrons caused by a change in the temperature of the material in question. The Doppler reactivity coefficient provides instantaneous negative reactivity feedback to any rise in fuel temperature, on either a gross or local basis. The magnitude of the Doppler coefficient is inherent in the fuel design and does not vary significantly among BWR designs. For most structural and moderator materials, resonance absorption is not significant, but in U^{238}

and Pu²⁴⁰ an increase in temperature produces a comparatively large increase in the effective absorption cross-section. The resulting parasitic absorption of neutrons causes an immediate loss in reactivity.

A demonstration of this can be found by observing the k-infinities at nominal and elevated fuel temperature for the dominant lattices of each ESBWR initial core GE14E bundle design. Figure 3-31 and Figure 3-32 illustrate the hot uncontrolled k-infinities for the dominant lattice at 40% void history. The k-infinity data is also provided in Tables 3-21 through 3-22 (note "HOTUNCD" indicates k-infinity data at elevated fuel temperature). For both figures, the effects of Doppler [[]]. This trend is consistent for all ESBWR lattices within all reference designs.

A discussion on the Doppler reactivity coefficient was provided in Section 1. A parameter labeled CDOP was introduced to characterize this reactivity coefficient:

$$CDOP = \frac{1000(k_{T_1} - k_{T_0})}{k_{T_0} (\sqrt{T_1} - \sqrt{T_0})}$$

where:

T_0 = normal hot operating temperature (Kelvin).

T_1 = elevated temperature (Kelvin).

k_{T_1} = eigenvalue at elevated temperature.

k_{T_0} = eigenvalue at normal operating temperature.

The CDOP values were determined for the ESBWR GE14E equilibrium core bundles. For all cases evaluated, the CDOP value was found to be negative. Typical values for the enriched lattices found in the equilibrium core GE14E bundles range from about [[

] at zero exposure and 40% void fraction. This compares to a typical CDOP value of [[]] that was reported in Reference 8 for GE14 compliance to Amendment 22.

3.3 SUMMARY

This section described two GE14E bundle nuclear designs that have been developed to meet all nuclear design bases presented in Section 2. These bundles are intended for an equilibrium core application. Core performance utilizing these two designs is presented in Section 4.

[[

Figure 3-1. Bundle Design for 3194

]]

[[

]]

Figure 3-2. Fuel Rods for 3194

[[**Figure 3-3. Fuel Rod Axial Profiles for 3194**]]

[[

Figure 3-4. Splits and Weights for 3194

]]

[[

Figure 3-5. Bundle Design for 3195

]]

[[

]]

Figure 3-6. Fuel Rods for 3195

[[

Figure 3-7. Fuel Rod Axial Profiles for 3195

]]

[[

]]

Figure 3-8. Splits and Weights for 3195

Table 3-1. Lattice 8859 K-infinity

Exposure (GWd/ST)	K-infinity		
	VF 0.0	VF 0.4	VF 0.7
0.0	[[
0.2			
1.0			
2.0			
3.0			
4.0			
5.0			
6.0			
7.0			
8.0			
9.0			
10.0			
11.0			
12.0			
13.0			
14.0			
15.0			
16.0			
17.0			
18.0			
19.0			
20.0			
21.0			
22.0			
23.0			
24.0			
25.0			
30.0			
35.0			
40.0			
45.0			
50.0			
55.0			
60.0			
65.0]]

[[

]]

Figure 3-9. Lattice 8859 K-infinity

(* K-infinity based on three void history fractions of 0.0, 0.4 and 0.7)

Table 3-2. Lattice 8860 K-infinity

Exposure (GWd/ST)	K-infinity		
	VF 0.0	VF 0.4	VF 0.7
0.0	[[
0.2			
1.0			
2.0			
3.0			
4.0			
5.0			
6.0			
7.0			
8.0			
9.0			
10.0			
11.0			
12.0			
13.0			
14.0			
15.0			
16.0			
17.0			
18.0			
19.0			
20.0			
21.0			
22.0			
23.0			
24.0			
25.0			
30.0			
35.0			
40.0			
45.0			
50.0			
55.0			
60.0			
65.0]]

[[

]]

Figure 3-10. Lattice 8860 K-infinity

(* K-infinity based on three void history fractions of 0.0, 0.4 and 0.7)

Table 3-3. Lattice 8861 K-infinity

Exposure (GWd/ST)	K-infinity		
	VF 0.0	VF 0.4	VF 0.7
0.0	[[
0.2			
1.0			
2.0			
3.0			
4.0			
5.0			
6.0			
7.0			
8.0			
9.0			
10.0			
11.0			
12.0			
13.0			
14.0			
15.0			
16.0			
17.0			
18.0			
19.0			
20.0			
21.0			
22.0			
23.0			
24.0			
25.0			
30.0			
35.0			
40.0			
45.0			
50.0			
55.0			
60.0			
65.0]]

[[

]]

Figure 3-11. Lattice 8861 K-infinity

(* K-infinity based on three void history fractions of 0.0, 0.4 and 0.7)

Table 3-4. Lattice 8862 K-infinity

Exposure (Gwd/ST)	K-infinity		
	VF 0.0	VF 0.4	VF 0.7
0.0	[[
0.2			
1.0			
2.0			
3.0			
4.0			
5.0			
6.0			
7.0			
8.0			
9.0			
10.0			
11.0			
12.0			
13.0			
14.0			
15.0			
16.0			
17.0			
18.0			
19.0			
20.0			
21.0			
22.0			
23.0			
24.0			
25.0			
30.0			
35.0			
40.0			
45.0			
50.0			
55.0			
60.0			
65.0]]

[[

]]

Figure 3-12. Lattice 8862 K-infinity

(* K-infinity based on three void history fractions of 0.0, 0.4 and 0.7)

Table 3-5. Lattice 8863 K-infinity

Exposure (GWd/ST)	K-infinity		
	VF 0.0	VF 0.4	VF 0.7
0.0	[[
0.2			
1.0			
2.0			
3.0			
4.0			
5.0			
6.0			
7.0			
8.0			
9.0			
10.0			
11.0			
12.0			
13.0			
14.0			
15.0			
16.0			
17.0			
18.0			
19.0			
20.0			
21.0			
22.0			
23.0			
24.0			
25.0			
30.0			
35.0			
40.0			
45.0			
50.0			
55.0			
60.0			
65.0]]

[[

Figure 3-13. Lattice 8863 K-infinity

(* K-infinity based on three void history fractions of 0.0, 0.4 and 0.7)

]]

Table 3-6. Lattice 8864 K-infinity

Exposure (GWd/ST)	K-infinity		
	VF 0.0	VF 0.4	VF 0.7
0.0	[[
0.2			
1.0			
2.0			
3.0			
4.0			
5.0			
6.0			
7.0			
8.0			
9.0			
10.0			
11.0			
12.0			
13.0			
14.0			
15.0			
16.0			
17.0			
18.0			
19.0			
20.0			
21.0			
22.0			
23.0			
24.0			
25.0			
30.0			
35.0			
40.0			
45.0			
50.0			
55.0			
60.0			
65.0]]

[[

]]

Figure 3-14. Lattice 8864 K-infinity

(* K-infinity based on three void history fractions of 0.0, 0.4 and 0.7)

Table 3-7. Lattice 8865 K-infinity

Exposure (GWd/ST)	K-infinity		
	VF 0.0	VF 0.4	VF 0.7
0.0	[[
0.2			
1.0			
2.0			
3.0			
4.0			
5.0			
6.0			
7.0			
8.0			
9.0			
10.0			
11.0			
12.0			
13.0			
14.0			
15.0			
16.0			
17.0			
18.0			
19.0			
20.0			
21.0			
22.0			
23.0			
24.0			
25.0			
30.0			
35.0			
40.0			
45.0			
50.0			
55.0			
60.0			
65.0]]

[[

Figure 3-15. Lattice 8865 K-infinity

]]

(* K-infinity based on three void history fractions of 0.0, 0.4 and 0.7)

Table 3-8. Lattice 8866 K-infinity

Exposure (GWd/ST)	K-infinity		
	VF 0.0	VF 0.4	VF 0.7
0.0	[[
0.2			
1.0			
2.0			
3.0			
4.0			
5.0			
6.0			
7.0			
8.0			
9.0			
10.0			
11.0			
12.0			
13.0			
14.0			
15.0			
16.0			
17.0			
18.0			
19.0			
20.0			
21.0			
22.0			
23.0			
24.0			
25.0			
30.0			
35.0			
40.0			
45.0			
50.0			
55.0			
60.0			
65.0]]

[[

]]

Figure 3-16. Lattice 8866 K-infinity

(* K-infinity based on three void history fractions of 0.0, 0.4 and 0.7)

Table 3-9. Lattice 8867 K-infinity

Exposure (GWd/ST)	K-infinity		
	VF 0.0	VF 0.4	VF 0.7
0.0	[[
0.2			
1.0			
2.0			
3.0			
4.0			
5.0			
6.0			
7.0			
8.0			
9.0			
10.0			
11.0			
12.0			
13.0			
14.0			
15.0			
16.0			
17.0			
18.0			
19.0			
20.0			
21.0			
22.0			
23.0			
24.0			
25.0			
30.0			
35.0			
40.0			
45.0			
50.0			
55.0			
60.0			
65.0]]

[[

Figure 3-17. Lattice 8867 K-infinity

]]

(* K-infinity based on three void history fractions of 0.0, 0.4 and 0.7)

Table 3-10. Lattice 8859 Peaking

Exposure (GWd/ST)	Maximum Local Peaking		
	VF 0.0	VF 0.4	VF 0.7
0.0	[[
0.2			
1.0			
2.0			
3.0			
4.0			
5.0			
6.0			
7.0			
8.0			
9.0			
10.0			
11.0			
12.0			
13.0			
14.0			
15.0			
16.0			
17.0			
18.0			
19.0			
20.0			
21.0			
22.0			
23.0			
24.0			
25.0			
30.0			
35.0			
40.0			
45.0			
50.0			
55.0			
60.0			
65.0]]

[[

Figure 3-18. Lattice 8859 Maximum Local Peaking

(* Local peaking based on three void history fractions of 0.0, 0.4 and 0.7)

]]

Table 3-11. Lattice 8860 Peaking

Exposure (Gwd/ST)	Maximum Local Peaking		
	VF 0.0	VF 0.4	VF 0.7
0.0	[[
0.2			
1.0			
2.0			
3.0			
4.0			
5.0			
6.0			
7.0			
8.0			
9.0			
10.0			
11.0			
12.0			
13.0			
14.0			
15.0			
16.0			
17.0			
18.0			
19.0			
20.0			
21.0			
22.0			
23.0			
24.0			
25.0			
30.0			
35.0			
40.0			
45.0			
50.0			
55.0			
60.0			
65.0]]

[[

Figure 3-19. Lattice 8860 Maximum Local Peaking

]]

(* Local peaking based on three void history fractions of 0.0, 0.4 and 0.7)

Table 3-12. Lattice 8861 Peaking

Exposure (Gwd/ST)	Maximum Local Peaking		
	VF 0.0	VF 0.4	VF 0.7
0.0	[[
0.2			
1.0			
2.0			
3.0			
4.0			
5.0			
6.0			
7.0			
8.0			
9.0			
10.0			
11.0			
12.0			
13.0			
14.0			
15.0			
16.0			
17.0			
18.0			
19.0			
20.0			
21.0			
22.0			
23.0			
24.0			
25.0			
30.0			
35.0			
40.0			
45.0			
50.0			
55.0			
60.0			
65.0]]

[[

Figure 3-20. Lattice 8861 Maximum Local Peaking

]]

(* Local peaking based on three void history fractions of 0.0, 0.4 and 0.7)

Table 3-13. Lattice 8862 Peaking

Exposure (GWd/ST)	Maximum Local Peaking		
	VF 0.0	VF 0.4	VF 0.7
0.0	[[
0.2			
1.0			
2.0			
3.0			
4.0			
5.0			
6.0			
7.0			
8.0			
9.0			
10.0			
11.0			
12.0			
13.0			
14.0			
15.0			
16.0			
17.0			
18.0			
19.0			
20.0			
21.0			
22.0			
23.0			
24.0			
25.0			
30.0			
35.0			
40.0			
45.0			
50.0			
55.0			
60.0			
65.0]]

[[]]

Figure 3-21. Lattice 8862 Maximum Local Peaking
 (* Local peaking based on three void history fractions of 0.0, 0.4 and 0.7)

Table 3-14. Lattice 8863 Peaking

Exposure (GWd/ST)	Maximum Local Peaking		
	VF 0.0	VF 0.4	VF 0.7
0.0	[[
0.2			
1.0			
2.0			
3.0			
4.0			
5.0			
6.0			
7.0			
8.0			
9.0			
10.0			
11.0			
12.0			
13.0			
14.0			
15.0			
16.0			
17.0			
18.0			
19.0			
20.0			
21.0			
22.0			
23.0			
24.0			
25.0			
30.0			
35.0			
40.0			
45.0			
50.0			
55.0			
60.0			
65.0]]

[[

Figure 3-22. Lattice 8863 Maximum Local Peaking

]]

(* Local peaking based on three void history fractions of 0.0, 0.4 and 0.7)

Table 3-15. Lattice 8864 Peaking

Exposure (GWd/ST)	Maximum Local Peaking		
	VF 0.0	VF 0.4	VF 0.7
0.0	[[
0.2			
1.0			
2.0			
3.0			
4.0			
5.0			
6.0			
7.0			
8.0			
9.0			
10.0			
11.0			
12.0			
13.0			
14.0			
15.0			
16.0			
17.0			
18.0			
19.0			
20.0			
21.0			
22.0			
23.0			
24.0			
25.0			
30.0			
35.0			
40.0			
45.0			
50.0			
55.0			
60.0			
65.0]]

[[

Figure 3-23. Lattice 8864 Maximum Local Peaking

]]

(* Local peaking based on three void history fractions of 0.0, 0.4 and 0.7)

Table 3-16. Lattice 8865 Peaking

Exposure (GWd/ST)	Maximum Local Peaking		
	VF 0.0	VF 0.4	VF 0.7
0.0	[[
0.2			
1.0			
2.0			
3.0			
4.0			
5.0			
6.0			
7.0			
8.0			
9.0			
10.0			
11.0			
12.0			
13.0			
14.0			
15.0			
16.0			
17.0			
18.0			
19.0			
20.0			
21.0			
22.0			
23.0			
24.0			
25.0			
30.0			
35.0			
40.0			
45.0			
50.0			
55.0			
60.0			
65.0]]

[[

Figure 3-24. Lattice 8865 Maximum Local Peaking
 (* Local peaking based on three void history fractions of 0.0, 0.4 and 0.7)

]]

Table 3-17. Lattice 8866 Peaking

Exposure (Gwd/ST)	Maximum Local Peaking		
	VF 0.0	VF 0.4	VF 0.7
0.0	[[
0.2			
1.0			
2.0			
3.0			
4.0			
5.0			
6.0			
7.0			
8.0			
9.0			
10.0			
11.0			
12.0			
13.0			
14.0			
15.0			
16.0			
17.0			
18.0			
19.0			
20.0			
21.0			
22.0			
23.0			
24.0			
25.0			
30.0			
35.0			
40.0			
45.0			
50.0			
55.0			
60.0			
65.0]]

[[

Figure 3-25. Lattice 8866 Maximum Local Peaking

(* Local peaking based on three void history fractions of 0.0, 0.4 and 0.7)

]]

Table 3-18. Lattice 8867 Peaking

Exposure (GWd/ST)	Maximum Local Peaking		
	VF 0.0	VF 0.4	VF 0.7
0.0	[[
0.2			
1.0			
2.0			
3.0			
4.0			
5.0			
6.0			
7.0			
8.0			
9.0			
10.0			
11.0			
12.0			
13.0			
14.0			
15.0			
16.0			
17.0			
18.0			
19.0			
20.0			
21.0			
22.0			
23.0			
24.0			
25.0			
30.0			
35.0			
40.0			
45.0			
50.0			
55.0			
60.0			
65.0]]

[[

Figure 3-26. Lattice 8867 Maximum Local Peaking

]]

(* Local peaking based on three void history fractions of 0.0, 0.4 and 0.7)

[[**Figure 3-27. Rod Local Peaking (Bundle 3194, Lattice 8860, VF=40%, BOL)**]]

[[

]]

Figure 3-28. Rod Local Peaking (Bundle 3195, Lattice 8864, VF=40%, BOL)

Table 3-19. Bundle 3194 Uncontrolled and Controlled R-Factors

Exposure (GWd/ST)	R-Factor (Fully Uncontrolled)	R-Factor (Fully Controlled)
0.0	[[
0.2		
1.0		
2.0		
3.0		
4.0		
5.0		
6.0		
7.0		
8.0		
9.0		
10.0		
11.0		
12.0		
13.0		
14.0		
15.0		
16.0		
17.0		
18.0		
19.0		
20.0		
21.0		
22.0		
23.0		
24.0		
25.0		
30.0		
35.0		
40.0		
45.0		
50.0		
55.0		
60.0		
65.0]]

Table 3-20. Bundle 3195 Uncontrolled and Controlled R-Factors

Exposure (GWd/ST)	R-Factor (Fully Uncontrolled)	R-Factor (Fully Controlled)
0.0	[[
0.2		
1.0		
2.0		
3.0		
4.0		
5.0		
6.0		
7.0		
8.0		
9.0		
10.0		
11.0		
12.0		
13.0		
14.0		
15.0		
16.0		
17.0		
18.0		
19.0		
20.0		
21.0		
22.0		
23.0		
24.0		
25.0		
30.0		
35.0		
40.0		
45.0		
50.0		
55.0		
60.0		
65.0]]

[[

]]

Figure 3-29. Uncontrolled Rod R-Factors (Bundle 3194, 20 GWD/ST)

[[

]]

Figure 3-30. Uncontrolled Rod R-Factors (Bundle 3195, 20 GWD/ST)

Table 3-21. Lattice 8860 K-∞

Exposure (GWd/ST)	K-infinity (40% VF)	
	HOTUNC	HOTUNCD
0.0	[[
0.2		
1.0		
2.0		
3.0		
4.0		
5.0		
6.0		
7.0		
8.0		
9.0		
10.0		
11.0		
12.0		
13.0		
14.0		
15.0		
16.0		
17.0		
18.0		
19.0		
20.0		
21.0		
22.0		
23.0		
24.0		
25.0		
30.0		
35.0		
40.0		
45.0		
50.0		
55.0		
60.0		
65.0]]

[[

Figure 3-31. Bundle 3194 Lattice 8860 K-infinity at 40% VF

]]

Table 3-22. Lattice 8864 K-∞

Exposure (GWd/ST)	K-infinity (40% VF)	
	HOTUNC	HOTUNCD
0.0	[[
0.2		
1.0		
2.0		
3.0		
4.0		
5.0		
6.0		
7.0		
8.0		
9.0		
10.0		
11.0		
12.0		
13.0		
14.0		
15.0		
16.0		
17.0		
18.0		
19.0		
20.0		
21.0		
22.0		
23.0		
24.0		
25.0		
30.0		
35.0		
40.0		
45.0		
50.0		
55.0		
60.0		
65.0]]

[[

Figure 3-32. Bundle 3195 Lattice 8864 K-infinity at 40% VF

]]

4. CORE NUCLEAR DESIGN EVALUATION

The ESBWR is a light-water moderated reactor fueled with slightly enriched uranium-dioxide. The use of water as a moderator produces a neutron energy spectrum in which fissions are caused principally by thermal neutrons. At normal operating conditions, the moderator boils, producing a spatially variable distribution of steam voids in the core. The void reactivity feedback effect is an inherent safety feature of a BWR system. Any system change that increases reactor power, either locally or core-wide, produces additional steam voids and thus reduces power.

4.1 INTRODUCTION

The ESBWR core design is performed using the same analytical tools and methods that are applied to steady-state nuclear evaluations of all General Electric BWR cores. These nuclear physics methods, which are described in Section 1, have proven their abilities and capabilities over hundreds of reactor operating years. This section describes the various core analyses and results for the ESBWR reference equilibrium core based on these methods.

4.2 NUCLEAR DESIGN AND CORE LOADING PATTERN DESCRIPTION

The ESBWR is rated at 4500 MWth and consists of 1132 bundles and 269 control blades. The three-dimensional simulation modeling of the reference equilibrium core design was performed assuming quarter core mirror symmetry. Consequently, results in the upper left quadrant will be mirrored in the remaining three quadrants. Below are the nominal operating conditions for the ESBWR reference equilibrium core.

Parameter	Nominal Value
Power (MWth)	4500
Flow (Mlb/hr)	[[
Dome Pressure (psia)	
Bypass (%)	
Core Inlet Temperature (°F)]]

The reference core design is characterized by the fuel type loading pattern given in Figure 4-1. The reference design incorporates the GE14E bundle designs previously described in Section 3 to achieve optimum core performance (i.e., thermal limits, hot excess reactivity, cold shutdown margin, etc.) for an equilibrium cycle utilizing the Control Cell Core (CCC) loading strategy. As previously discussed, the lattice enrichments and gadolinia concentrations have been selected to achieve the desired k-infinity and local peaking behavior and the lattice arrangements, or zones, within each bundle have been chosen to yield the desired axial power characteristics when assembled in the core. The bundle types and quantities as well as beginning-of-cycle (BOC) bundle exposures are also shown in Figure 4-1. The lower enrichment assembly, shown as IAT number 6, is placed in central core locations. [[

]] With respect to the CCC loading strategy, the A-2 control rod locations typically contain lower reactivity bundles, with the lowest reactivity bundles reserved for peripheral locations. The CCC core design limits control rod movement to a fixed group of control rods and control rod motion occurs adjacent only to low power fuel. This strategy results in reduced control blade history effects and simplified operation.

This reference core is designed [[

]].

4.3 EIGENVALUE DETERMINATION

At the beginning of a core design effort, hot and cold eigenvalues are determined in order to calibrate the 3D simulator predictions to actual results of the BWR fleet. Because of the similarities between current operating BWRs and the ESBWR, as well as the identical nature of the lattice physics calculations, exposure dependent eigenvalues could be obtained. Incorporating the actual trends of other large BWR cores, the hot and cold exposure dependent eigenvalues were determined. Table 4-1 and Figure 4-2 show the design basis exposure dependent hot eigenvalue. Table 4-2 and Figure 4-3 show the design basis exposure dependent cold eigenvalue. Eigenvalue determination is used for hot and cold reactivity calculations as well as determining the appropriate control rod inventory needed to provide criticality at full power conditions.

4.4 CONTROL ROD PATTERNS INCLUDING AXIAL POWER CONSIDERATIONS

Figure 4-4 illustrates the control rod patterns for this reference equilibrium core. The maximum number of control rod notches per control blade is defined as 80. That is, for this simulation, a control rod at notch 80 is fully withdrawn; a control rod at notch 0 is fully inserted. The rod patterns utilize [[

]], maximizes operating capacity factor, and provides for improved fuel cycle efficiency.

An inherent advantage of the ESBWR is the improved fuel cycle efficiency due to spectral shift that is a function of axial power shape control. By achieving a bottom peaked core average axial power shape, the presence of voids in the middle and top of the core provides an environment helpful in creating additional fuel in the form of plutonium. Consequently, additional full power capability is provided towards EOC as the axial shape slowly migrates towards the top and the plutonium is utilized. This classic BWR characteristic is well illustrated in Figures 4-5 through 4-10, which show the progression in axial power shape throughout each of the major control rod sequences from BOC to EOC. Core average axial power results are also provided in Tables 4-3 through 4-8. Figures 4-11 through 4-16 illustrate the core average axial exposure shape from BOC to EOC for each control rod sequences. Corresponding exposure results are provided in Tables 4-9 through 4-14.

With regard to the target rod patterns, it was previously mentioned that the control rods are selected based on the design basis hot critical eigenvalue as well as thermal limit considerations. Table 4-15 and Figure 4-17 illustrate how well the target control rod patterns satisfy the design basis hot critical eigenvalue. The 2-D EOC bundle average exposure distribution at the end of this rodded burn scenario is shown in Figure 4-18.

4.5 INTEGRATED POWER DISTRIBUTION

Although a bundle integrated power constraint does not exist, this is a helpful parameter when understanding loading pattern influence on individual power generation per bundle. During typical BWR non-initial core operation, the once-burnt high reactivity fuel provides the most influence on power distribution. Similarly, towards the EOC the fresh fuel provides most of the influence. In an exposed core, it is this balance of fresh and once burnt fuel that contributes to a more uniform core power distribution. The maximum bundle integrated power value, also referred to as radial peaking factor, is shown in Table 4-16 and in Figure 4-19. The maximum range of values throughout the cycle [[]] which are bounded by current operating BWRs. The corresponding 2-D bundle integrated powers at the beginning and end of each main control rod pattern sequence are presented in Figures 4-20 through 4-31.

4.6 THERMAL LIMIT EVALUATION

The core power distribution is a function of fuel bundle design, core loading, control rod pattern, core exposure distributions and core coolant flow rate. The thermal performance parameters, MLHGR and MCPR, limit the core power distribution. The analysis of the performance of the reference equilibrium core design in terms of power distribution, and the associated MLHGR and MCPR distributions within the core throughout the cycle, are discussed below.

4.6.1 MLHGR

The Maximum Fraction of Linear Power Density (MFLPD) is shown as a function of cycle exposure in Table 4-17 and Figure 4-32. Note that the value plotted in Figure 4-32 represents the

maximum value for any node in the core at the specified exposure point. The MFLPD parameter, in general terms, is defined as:

$$\text{MFLPD} = \text{LHGR} / \text{LHGR Limit}$$

It should be noted that the thermal mechanical LHGR limit is exposure dependent, which necessitates establishing the MFLPD parameter to capture this. A MFLPD that is equal to 1.0 corresponds to a rod within a six inch node that is operating at its LHGR limit and any further increases in LHGR result in entering a Technical Specification Limiting Condition of Operation (LCO). Every rod within the node has a MFLPD. The rod with the highest MFLPD in any given node defines the maximum MFLPD and this becomes the nodal MFLPD. The node with the highest MFLPD in an assembly can be thought of as the limiting MFLPD for that assembly. The highest MFLPD for any node in the core corresponds to the most limiting node and defines the minimum operating margin ($1.0 - \text{MFLPD}$) in the reactor core. Figures 4-33 through 4-44 show the 2-D MFLPD distribution at the beginning and end of each main control rod sequence. The MLHGR limit used in the calculation of the MFLPD is reported in Reference 14.

4.6.2 MCPR

Table 4-18 and Figure 4-45 illustrate the minimum critical power ratio (MCPR) as a function of exposure throughout the cycle. Figure 4-46 through Figure 4-57 provide the 2-D MCPR distribution at the beginning and end of each control rod sequence. The Operating Limit Minimum Critical Power Ratio (OLMCPR) is expected to be [[]]. Therefore, the reference equilibrium core will conform to this OLMCPR with sufficient margin. The OLMCPR is determined in a manner described in Reference 13.

4.7 HOT EXCESS EVALUATION

A hot excess reactivity calculation illustrates the amount of excess reactivity a core design provides throughout the cycle. This calculation is performed by withdrawing all control rods at selected state points through the cycle and comparing the difference between the resulting eigenvalue and the design basis hot critical eigenvalue previously shown in Figure 4-2. Table 4-19 and Figure 4-58 shows the hot excess reactivity for this reference equilibrium core design. The BOC hot excess is estimated to be [[]]

However, control rod sequence adjustments are still adopted at fixed intervals to moderate the effects of CBH and to improve exposure burn-up and fuel cycle efficiency.

The excess reactivity described above is designed into the core and controlled by the control rod system and supplemented by gadolinia-urania fuel rods discussed in Section 3. Gadolinia is used to provide partial control of the excess reactivity available during the fuel cycle. The burnable absorber loading controls local peaking behavior and suppresses the reactivity of the fuel bundle.

An optimum bundle design will utilize a sufficient number of gadolinia rods to suppress core reactivity at BOC and a sufficient concentration to limit the peak reactivity to a manageable level throughout the cycle with little remaining residual gadolinia at EOC. The burnable absorber reduces the requirement for control rod inventory. Control rods are used primarily to compensate for reactivity changes due to burn-up and to maintain an acceptable core power distribution. A detailed description of the ESBWR equilibrium bundle designs was provided in Section 3.

4.8 COLD SHUTDOWN MARGIN EVALUATION

The ESBWR control rod system is designed to provide adequate shutdown margin and control of the maximum excess reactivity anticipated during plant operation. For this evaluation the core is assumed to be in the cold, xenon-free condition in order to ensure that the calculated values are conservative. Further discussion of the uncertainty of these calculations is given in Reference 10.

Shutdown margin results through the cycle are shown in Table 4-20 and in Figure 4-60. The shutdown margin is evaluated by calculating the core neutron multiplication with the core simulator at selected exposure points, assuming the highest worth control rod, or rod pair, is stuck in the fully withdrawn position. Since two control rod drives are assigned to a single Hydraulic Control Unit (HCU) for the ESBWR, the shutdown margin evaluation assumes that a rod pair is stuck in the fully withdrawn position. The control rod drive to HCU assignments are shown in Figure 4-59. Note that since there is an odd number of control rods, there is one HCU that is assigned a single control rod; this is HCU number 51, which is in the very center of the core. Since all rod pairs were selected with sufficient separation between them, they may be considered loosely coupled. Figures 4-61 to 4-63 are provided to demonstrate this loose coupling. Control rod worths at BOC, MOC and EOC are compared for the HCU rod pair withdrawn and the corresponding strongest single rod of the rod pair withdrawn. Control rod worths are shown to be essentially the same for the forty highest worth HCUs in the top half of the core. Given that the core loading is quadrant symmetric, and HCU assignments are half core rotational symmetric, comparing the worths for the forty highest worth HCUs effectively covers about 60% of the total control rods in the ESBWR. Consequently, 2-D SDM results and SDM results through the cycle based on the highest worth single rod out can be considered equivalent to SDM results for the strongest HCU rod pair withdrawn.

The cold k_{eff} is calculated with the highest worth control rod, or rod pair, out at various exposures through the cycle. A value R is defined as the difference between the highest worth rod pair out k_{eff} at beginning of cycle (BOC) and the maximum calculated highest worth rod pair out k_{eff} at any exposure point. For the ESBWR reference equilibrium core, the minimum shutdown margin occurs at BOC; thus, the value of R is zero. The calculated k_{eff} values with all control rods fully inserted (k_{CARI}) and with the strongest rod fully out (k_{SRO}) are shown below at BOC, MOC (defined as 8.0 GWd/ST) and EOC conditions. Also shown is the corresponding cold critical design bases eigenvalue (k_{CRIT}).

Based on the design k_{CRIT} value, the predicted shutdown margin is [[
]], which is significantly above the minimum required technical specification shutdown margin value. Additional 2-D SDM results are provided in Figures 4-64 through 4-66 at BOC, MOC and EOC conditions. Note that these figures report the SDM for a single control rod withdrawn in the

upper left quadrant. For a HCU rod pair, the SDM would be equal to the lowest value of the two control rods that are assigned to the HCU.

Control Configuration	BOC K-eff	MOC K-eff	EOC K-eff
Fully Controlled (k_{CARI})	[[
Strongest Rod Out (k_{SRO})			
Critical k-effective (k_{CRIT})]]

4.9 STANDBY LIQUID CONTROL SYSTEM EVALUATION

The Standby Liquid Control System (SLCS) is designed to provide the capability of bringing the reactor, at any time in a cycle, from full power with a minimum control rod inventory (which is defined to be at the peak of the xenon transient) to a sub-critical condition with the reactor in the most reactive xenon-free state.

The requirements of this system are dependent primarily on the reactor power level and on the reactivity effects of voids and temperature between full power and cold, xenon-free conditions. The shutdown margin is calculated for a uniformly mixed equivalent concentration of natural boron, which is required in the reactor core to provide adequate cold shutdown margin after initiation of the SLCS. Calculations are performed throughout the cycle including the most reactive critical, xenon-free condition. Calculations are performed with all control rods withdrawn. The shutdown capability of the SLCS for the ESBWR reference initial core was calculated using [[

]]. Table 4-21 and Figure 4-67 shows that significant SLCS shutdown margin exists for the ESBWR core compared to a limit of 1%.

4.10 CRITICALITY OF REACTOR DURING REFUELING EVALUATION

The basis for maintaining the reactor in a sub-critical condition during refueling is presented in Subsection 2.2, and a discussion of how control requirements are met is given in Section 4.8. The minimum required shutdown margin is given in the technical specifications.

4.11 NEGATIVE REACTIVITY FEEDBACK EVALUATION

Reactivity coefficients are a measure of the differential changes in reactivity produced by differential changes in core conditions. These coefficients are useful in understanding the response of the core to external disturbances. The Doppler reactivity coefficient, previously discussed in Section 3, and the moderator void reactivity coefficient are the two primary reactivity coefficients that characterize the dynamic behavior of BWRs.

The safety analysis methods are based on system and core models that include an explicit representation of the core space-time kinetics. Therefore, the reactivity coefficients are not

directly used in the safety analysis methods, but are useful in the general understanding and discussion of the core response to perturbations.

4.11.1 Moderator Temperature Coefficient Evaluation

The moderator temperature coefficient (MTC) is associated with the change in the water moderating capability. A negative MTC during power operation provides inherent protection against power excursions. Hot standby is the condition under which the BWR core coolant has reached rated pressure and the temperature at which boiling has begun. Once boiling begins, the moderator temperature remains essentially constant in the boiling regions.

Analyses of the MTC of the reference equilibrium core design were performed. Table 4-22 and Figure 4-68 show the eigenvalues as a function of moderator temperature at three exposure state points for the critical rod pattern configuration determined at zero xenon conditions. These eigenvalues were then used to determine the MTC for the reference equilibrium core. The variation of the MTC as a function of temperature is shown in Table 4-23 and Figure 4-69 for three exposure points through the cycle.

A second set of analyses was performed with a high xenon concentration. This conservative analysis condition might be expected to occur during a plant startup that immediately follows plant shutdown (e.g., reactor scram). The accumulation of xenon would result in a lower critical control fraction that results in a less negative MTC. Table 4-26 and Figure 4-72 show the eigenvalues as a function of moderator temperature at the same three exposure state points based on a critical rod pattern established with xenon. The variation of the MTC as a function of temperature is shown in Table 4-27 and Figure 4-73 with xenon.

The most limiting state condition was determined to be at the end of cycle for the critical core configuration. The results demonstrated that the MTC is [[

]]

The results of these analyses at these conditions indicate that the MTC is negative for all moderator temperatures in the operating temperature range.

4.11.2 Moderator Void Coefficient Evaluation

The moderator void coefficient (MVC) should be large enough to prevent power oscillation due to spatial xenon changes yet small enough that pressurization transients do not unduly limit plant operation. In addition, the MVC has the ability to flatten the radial power distribution and to provide ease of reactor control due to the void feedback mechanism. The overall MVC is always negative over the complete operating range.

The results of these analyses show that boiling of the moderator in the active channel flow area results in negative reactivity feedback for all expected modes of operation. These results are true for both sets of analyses performed, i.e., at zero xenon conditions and at high xenon concentration. The operating mode selected to represent the most limiting condition (the least negative value of MVC) was the cold critical state at the middle of the equilibrium cycle for both

xenon conditions. Table 4-24 and Figure 4-70 show the variation in eigenvalue as a function of moderator temperature and voids at three exposure state points for the critical rod configuration determined at zero xenon conditions. These eigenvalues were then used to determine the MVC for the reference equilibrium core. The variation of the MVC as a function of temperature is shown in Table 4-25 and Figure 4-71 for three exposure points through the cycle. The eigenvalue results based on high xenon conditions are shown in Table 4-28 and Figure 4-74 while the corresponding MVC results are shown in Table 4-29 and Figure 4-75.

4.12 XENON STABILITY EVALUATION

Boiling water reactors do not have instability problems due to xenon. This has been demonstrated by:

- Never having observed xenon instabilities in operating BWRs
- Special tests which have been conducted on operating BWRs in an attempt to force the reactor into xenon instability; and
- Calculations

All of these indicators have proven that xenon transients are highly damped in a BWR due to the large negative moderator void feedback. Xenon stability analysis and experiments are reported in Reference 11. Specific evaluations demonstrating the damping of xenon transients (oscillations) for an ESBWR equilibrium core are carried out in the following subsections.

4.12.1 BWR Xenon Trends

Spatial stability measurements and analytical studies for the current BWR fleet have demonstrated very stable xenon transient performance characteristics. This stability is attributed to the large negative power coefficient that characterizes the BWR design. The negative power coefficient provides for strong spatial damping of transient reactor performance that results from xenon transients. The ESBWR shares the same negative power coefficient characteristics with current BWR designs, and is similarly stable with respect to xenon transient performance.

The large negative power coefficient of reactivity is a unique characteristic that results from moderator boiling. The large change in moderator density in the boiling environment of the reactor core is primarily responsible for the large negative power coefficient.

Non-linear trends also exist in the axial xenon distributions in an ESBWR core. As the moderator density changes axially in the reactor core, the neutron spectrum also changes. As the moderator density decreases, the neutron spectrum hardens. Since the Xe^{135} isotope has a smaller absorption cross section at higher neutron energies, the Xe^{135} distribution is affected axially by the non-uniform moderator density. The I^{135} isotope, which decays to produce Xe^{135} , is substantially proportional to the axial power distribution as it is a direct result of the fission process, and is not strongly affected by the axial changes in the neutron spectrum. The resulting differences in the Xe^{135} and I^{135} distributions lead to non-linear axial trends in the transient performance, which help to dampen any oscillatory behavior caused by transient concentration differences.

The non-linear axial trends in nuclear characteristics, coupled with the negative power coefficient resulting from the non-uniform moderator density, result in non-linear axial responses that cause axial xenon redistributions to be damped in one cycle. Additionally, although large reactor cores exhibit loosely coupled characteristics, local feedback at each point in the reactor core is provided by moderator boiling. The large negative power coefficient, coupled with the local feedback provided by localized boiling, work together to effectively damp azimuthal and radial oscillations.

The physical and nuclear characteristics of the ESBWR design have different effects upon the magnitude of the power coefficient. A summary of the important design characteristics and their influence on the power coefficient are shown below. These characteristics are consistent between BWR and ESBWR designs.

Increased Variable	Effect on Power Coefficient
moderator to fuel ratio	less negative
fuel rod diameter	less negative
fuel enrichment	more negative
fuel exposure	less negative
bypass water fraction	less negative
core size	less negative
void content	more negative

The primary differences between current operating BWRs and the ESBWR design include core size, core height, and the lack of forced recirculation flow in the ESBWR. The ESBWR core design is larger than the largest operating BWR (1132 bundles vs. 872 bundles). However the active fuel height for the ESBWR is 20% shorter than current BWR fuel designs. This results in slightly improved xenon stability for the ESBWR since the axial moderator density change associated with boiling occurs over a shorter distance. The natural recirculation characteristic of the ESBWR is also an important difference, because most power maneuvers require the use of control rods to control core reactivity and core power. The control rods have a strong negative influence on the power coefficient. Control rod worth increases rapidly as water density is decreased because of the increase in the thermal neutron diffusion length with decreased moderator density. The required use of control rods to control core power complements the negative power coefficient associated with the non-uniform moderator density to effectively damp transient xenon effects.

4.12.2 EBWR Xenon Transient Response Analysis

The results of two representative xenon transient evaluations are summarized in the figures below. These calculations illustrate the inherently stable response of the ESBWR to step changes in power and the associated xenon transient effects. These calculations were performed for an ESBWR equilibrium core design using [[]]

The three-dimensional model used for the xenon transient evaluations includes all of the important non-linear trends associated with the non-uniform moderator distribution in the ESBWR. These features include a coupled nuclear thermal-hydraulics model, point-wise variability in nuclear properties, and exposure dependence of the nuclear characteristics of the fuel.

The first case (see Figure 4-76, Figure 4-77 and Figure 4-78) illustrates the ESBWR response to a rapid load drop from 100% power to 50% power. Control rods are inserted from the initial steady state critical condition at 100% power to reduce the power to 50%. The transient is then allowed to progress with no further control rod movement. As a result, the power is permitted to change in response to the changes in the xenon concentration. The addition of control blades to reduce the core power has a strong negative influence on the negative power coefficient. The resulting xenon transient [[

]].

The second case (see Figure 4-79, Figure 4-80 and Figure 4-81) illustrates the ESBWR response to a scram recovery scenario. The scram is simulated by rapidly reducing the reactor power from 100% to 4% for 8 hours. (Control rods are inserted from the initial steady state critical condition at 100% power to reduce the power to 4%.) During this 8-hour period, the xenon concentration builds up to its peak concentration. After 8 hours, the control rods are withdrawn back to their original positions from the critical control rod pattern. [[

]] The transient is then allowed to progress with no further control rod movement. The power is permitted to change in response to the changes in the xenon concentration. [[

]]

4.12.3 ESBWR Xenon Transient Conclusions

The negative power coefficient trends of an ESBWR have a pronounced effect on spatial xenon stability. The negative power coefficient results naturally from the non-uniform moderator distribution in the reactor core. This characteristic, coupled with the non-linear axial trends in nuclear characteristics, result in non-linear axial responses that cause the effects of xenon transients to be damped in one cycle. The effects of localized boiling provide direct local feedback that suppresses radial and azimuthal perturbations.

[[

]]

Figure 4-1. Reference Equilibrium Core Fuel Types and Quantities

Table 4-1. Hot Design Eigenvalues

Exposure (MWd/ST)	Hot Design K-eff
[[
]]

[[

Figure 4-2. Hot Design Eigenvalue vs. Exposure

]]

Table 4-2. Cold Design Eigenvalues

Exposure (MWd/ST)	Distributed K-eff	Local K-eff
[[
]]

[[

Figure 4-3. Cold Design Eigenvalue vs. Exposure

]]

||

Figure 4-4. Rod Patterns

||

[[

]]

Figure 4-4. Rod Patterns (Continued)

[[

]]

Figure 4-4. Rod Patterns (Continued)

[[

]]

Figure 4-4. Rod Patterns (Continued)

[[

]]

Figure 4-4. Rod Patterns (Continued)

[[

]]

Figure 4-4. Rod Patterns (Continued)

Figure 4-4. Rod Patterns (Continued)

Table 4-3. Axial Nodal Power Seq-1

Axial Node	Beginning of Sequence 1 Axial Power	End of Sequence 1 Axial Power
20	[[
19		
18		
17		
16		
15		
14		
13		
12		
11		
10		
9		
8		
7		
6		
5		
4		
3		
2		
1]]

[[**Figure 4-5. Sequence 1 Core Average Axial Power Distributions**]]

Table 4-4. Axial Nodal Power Seq-2

Axial Node	Beginning of Sequence 2 Axial Power	End of Sequence 2 Axial Power
20	[[
19		
18		
17		
16		
15		
14		
13		
12		
11		
10		
9		
8		
7		
6		
5		
4		
3		
2		
1]]

[[**Figure 4-6. Sequence 2 Core Average Axial Power Distributions**]]

Table 4-5. Axial Nodal Power Seq-3

Axial Node	Beginning of Sequence 3 Axial Power	End of Sequence 3 Axial Power
20	[[
19		
18		
17		
16		
15		
14		
13		
12		
11		
10		
9		
8		
7		
6		
5		
4		
3		
2		
1]]

[[**Figure 4-7. Sequence 3 Core Average Axial Power Distributions**]]

Table 4-6. Axial Nodal Power Seq-4

Axial Node	Beginning of Sequence 4 Axial Power	End of Sequence 4 Axial Power
20	[[
19		
18		
17		
16		
15		
14		
13		
12		
11		
10		
9		
8		
7		
6		
5		
4		
3		
2		
1]]

[[**Figure 4-8. Sequence 4 Core Average Axial Power Distributions**]]

Table 4-7. Axial Nodal Power Seq-5

Axial Node	Beginning of Sequence 5 Axial Power	End of Sequence 5 Axial Power
20	[[
19		
18		
17		
16		
15		
14		
13		
12		
11		
10		
9		
8		
7		
6		
5		
4		
3		
2		
1]]

[[**Figure 4-9. Sequence 5 Core Average Axial Power Distributions**]]

Table 4-8. Axial Nodal Power Seq-6

Axial Node	Beginning of Sequence 6 Axial Power	End of Sequence 6 Axial Power
20	[[
19		
18		
17		
16		
15		
14		
13		
12		
11		
10		
9		
8		
7		
6		
5		
4		
3		
2		
1]]

[[**Figure 4-10. Sequence 6 Core Average Axial Power Distributions**]]

Table 4-9. Nodal Exposure Seq-1

Axial Node	Beginning of Sequence 1 Axial Exposure (GWd/ST)	End of Sequence 1 Axial Exposure (GWd/ST)
20	[[
19		
18		
17		
16		
15		
14		
13		
12		
11		
10		
9		
8		
7		
6		
5		
4		
3		
2		
1]]

[[**Figure 4-11. Sequence 1 Core Average Axial Exposure Distributions**]]

Table 4-10. Nodal Exposure Seq-2

Axial Node	Beginning of Sequence 2 Axial Exposure (GWd/ST)	End of Sequence 2 Axial Exposure (GWd/ST)
20	[[
19		
18		
17		
16		
15		
14		
13		
12		
11		
10		
9		
8		
7		
6		
5		
4		
3		
2		
1]]

[[
Figure 4-12. Sequence 2 Core Average Axial Exposure Distributions]]

Table 4-11. Nodal Exposure Seq-3

Axial Node	Beginning of Sequence 3 Axial Exposure (GWd/ST)	End of Sequence 3 Axial Exposure (GWd/ST)
20	[[
19		
18		
17		
16		
15		
14		
13		
12		
11		
10		
9		
8		
7		
6		
5		
4		
3		
2		
1]]

[[
Figure 4-13. Sequence 3 Core Average Axial Exposure Distributions]]

Table 4-12. Nodal Exposure Seq-4

Axial Node	Beginning of Sequence 4 Axial Exposure (GWd/ST)	End of Sequence 4 Axial Exposure (GWd/ST)
20	[[
19		
18		
17		
16		
15		
14		
13		
12		
11		
10		
9		
8		
7		
6		
5		
4		
3		
2		
1]]

[[
Figure 4-14. Sequence 4 Core Average Axial Exposure Distributions
]]

Table 4-13. Nodal Exposure Seq-5

Axial Node	Beginning of Sequence 5 Axial Exposure (GWd/ST)	End of Sequence 5 Axial Exposure (GWd/ST)
20	[[
19		
18		
17		
16		
15		
14		
13		
12		
11		
10		
9		
8		
7		
6		
5		
4		
3		
2		
1]]

[[
Figure 4-15. Sequence 5 Core Average Axial Exposure Distributions
]]

Table 4-14. Nodal Exposure Seq-6

Axial Node	Beginning of Sequence 6 Axial Exposure (GWd/ST)	End of Sequence 6 Axial Exposure (GWd/ST)
20	[[
19		
18		
17		
16		
15		
14		
13		
12		
11		
10		
9		
8		
7		
6		
5		
4		
3		
2		
1]]

[[
Figure 4-16. Sequence 6 Core Average Axial Exposure Distributions
]]

Table 4-15. Hot K-eff vs Exposure

Exposure (MWD/ST)	K-eff
[[
]]

[[**Figure 4-17. Hot Eigenvalue vs. Cycle Exposure**]]

[[

(Note - all shaded cells indicate the A2 control rods used for Control Cell Core operation)

]]

Figure 4-18. End of Cycle Bundle Average Exposure (16.73 GWd/ST)

[[**Figure 4-20. Beginning of Sequence 1 Integrated Bundle Power (0.0 GWd/ST)**]]

[[**Figure 4-21. End of Sequence 1 Integrated Bundle Power (3.0 GWd/ST)**]]

[[**Figure 4-22. Beginning of Sequence 2 Integrated Bundle Power (3.0 GWd/ST)**]]

[[

Figure 4-23. End of Sequence 2 Integrated Bundle Power (6.0 GWd/ST)

]]

[[**Figure 4-24. Beginning of Sequence 3 Integrated Bundle Power (6.0 GWd/ST)**]]

[[**Figure 4-25. End of Sequence 3 Integrated Bundle Power (9.0 MWd/ST)**]]

[[**Figure 4-26. Beginning of Sequence 4 Integrated Bundle Power (9.0 MWd/ST)**]]

[[**Figure 4-27. End of Sequence 4 Integrated Bundle Power (12.0 GWd/ST)**]]

[[**Figure 4-28. Beginning of Sequence 5 Integrated Bundle Power (12.0 MWd/ST)**]]

[[**Figure 4-29. End of Sequence 5 Integrated Bundle Power (15.0 GWd/ST)**]]

[[**Figure 4-30. Beginning of Sequence 6 Integrated Bundle Power (15.5 MWd/ST)**]]

[[**Figure 4-31. End of Sequence 6 Integrated Bundle Power (16.73 GWd/ST)**]]

Table 4-17. MFLPD vs Exposure

Exposure (MWD/ST)	MFLPD
[[
]]

[[]]

Figure 4-32. MFLPD vs. Cycle Exposure

[[

Figure 4-33. Beginning of Sequence 1 MFLPD (0.0 GWd/ST)

]]

[[

Figure 4-34. End of Sequence 1 MFLPD (3.0 GWd/ST)

]]

[[

Figure 4-35. Beginning of Sequence 2 MFLPD (3.0 GWd/ST)

]]

[[

Figure 4-36. End of Sequence 2 MFLPD (6.0 GWd/ST)

]]

[[

Figure 4-37. Beginning of Sequence 3 MFLPD (6.0 GWd/ST)

]]

[[

Figure 4-38. End of Sequence 3 MFLPD (9.0 MWd/ST)

]]

[[

Figure 4-39. Beginning of Sequence 4 MFLPD (9.0 MWd/ST)

]]

[[

Figure 4-40. End of Sequence 4 MFLPD (12.0 GWd/ST)

]]

[[

Figure 4-41. Beginning of Sequence 5 MFLPD (12.0 MWd/ST)

]]

[[

Figure 4-42. End of Sequence 5 MFLPD (15.0 GWd/ST)

]]

[[

Figure 4-43. Beginning of Sequence 6 MFLPD (15.5 MWd/ST)

]]

[[

Figure 4-44. End of Sequence 6 MFLPD (16.73 GWd/ST)

]]

Table 4-18. MCPR vs Exposure

Exposure (MWD/ST)	MCPR
[[
]]	

[[**Figure 4-45. MCPR vs. Cycle Exposure**]]

[[

Figure 4-46. Beginning of Sequence 1 MCPR (0.0 GWd/ST)

]]

[[

Figure 4-47. End of Sequence 1 MCPR (3.0 GWd/ST)

]]

[[

Figure 4-48. Beginning of Sequence 2 MCPR (3.0 GWd/ST)

]]

[[

Figure 4-49. End of Sequence 2 MCPR (6.0 GWd/ST)

]]

[[

Figure 4-50. Beginning of Sequence 3 MCPR (6.0 GWd/ST)

]]

[[

Figure 4-51. End of Sequence 3 MCPR (9.0 MWd/ST)

]]

[[

Figure 4-52. Beginning of Sequence 4 MCPR (9.0 GWd/ST)

]]

[[

Figure 4-53. End of Sequence 4 MCPR (12.0 GWd/ST)

]]

[[

Figure 4-54. Beginning of Sequence 5 MCPR (12.0 GWd/ST)

]]

[[

Figure 4-55. End of Sequence 5 MCPR (15.0 GWd/ST)

]]

[[

Figure 4-56. Beginning of Sequence 6 MCPR (15.5 GWd/ST)

]]

[[

Figure 4-57. End of Sequence 6 MCPR (16.73 GWd/ST)

]]

[[

Figure 4-59. Hydraulic Control Unit Assignments

]]

Table 4-20. Cold Shutdown Margin

Exposure (MWD/ST)	Cold SDM (%)
[[
]]

[[]]

Figure 4-60. Cold Shutdown Margin vs. Cycle Exposure

[[

Figure 4-61. Control Rod Worth Comparisons at BOC (0.00 GWd/ST)

]]

[[

Figure 4-62. Control Rod Worth Comparisons at MOC (8.00 GWd/ST)

]]

[[

Figure 4-63. Control Rod Worth Comparisons at EOC (16.73 GWd/ST)

]]

[[

]]

Figure 4-64. Cold Shutdown Margin Distribution (%) at BOC (0.0 GWd/ST)

[[

]]

Figure 4-65. Cold Shutdown Margin Distribution (%) at MOC (8.0 GWd/ST)

[[

]]

Figure 4-66. Cold Shutdown Margin Distribution (%) at EOC (16.73 GWd/ST)

Table 4-22. Eigenvalues for MTC – Zero

Xenon

Temperature (°C)	Eigenvalue
BOC	
[[
]]
MOC	
[[
]]
EOC	
[[
]]

[[]]
Figure 4-68. Eigenvalues vs. Moderator Temperature (for MTC/Zero Xenon)

Table 4-23. MTC without Xenon

Temperature (°C)	MTC (1/k)(dk/dT)
BOC	
[[
]]
MOC	
[[
]]
EOC	
[[
]]

[[**Figure 4-69. Moderator Temperature Coefficient without Xenon**]]

Table 4-24. Eigenvalues for MVC - Zero Xenon

Temperature (°C)	Eigenvalue 0% Void	Eigenvalue 5% Void
BOC		
[[
]]
MOC		
[[
]]
EOC		
[[
]]

[[]]
Figure 4-70. Eigenvalues vs. Moderator Temperature (for MVC/Zero Xenon)

Table 4-25. MVC without Xenon

Temperature (°C)	MVC (1/k)(dk/dV)
BOC	
[[
]]
MOC	
[[
]]
EOC	
[[
]]

Figure 4-71. Moderator Void Coefficient without Xenon

Table 4-26. Eigenvalues for MTC/Xenon

Temperature (°C)	Eigenvalue
BOC	
[[
]]
MOC	
[[
]]
EOC	
[[
]]

[[**Figure 4-72. Eigenvalues vs. Moderator Temperature (for MTC/Xenon)**]]

Table 4-27. MTC with Xenon

Temperature (°C)	MTC (1/k)(dk/dT)
BOC	
[[
]]
MOC	
[[
]]
EOC	
[[
]]

[[**Figure 4-73. Moderator Temperature Coefficient with Xenon**]]

Table 4-28. Eigenvalues for MVC/Xenon

Temperature (°C)	Eigenvalue 0% Void	Eigenvalue 5% Void
BOC		
[[
]]
MOC		
[[
]]
EOC		
[[
]]

[[**Figure 4-74. Eigenvalues vs. Moderator Temperature (for MVC/Xenon)**]]

Table 4-29. MVC with Xenon

Temperature (°C)	MVC (1/k)(dk/dV)
BOC	
[[
]]
MOC	
[[
]]
EOC	
[[
]]

[[

Figure 4-75. Moderator Void Coefficient with Xenon

]]

[[

Figure 4-76. Load Drop – Power vs. Time

]]

[[

Figure 4-77. Load Drop – Xenon Worth vs. Time

]]

[[

Figure 4-78. Load Drop – Power vs. Time

]]

[[

Figure 4-79. Scram Recovery – Power vs. Time

]]

[[

Figure 4-80. Scram Recovery – Xenon Worth

]]

[[

Figure 4-81. Scram Recovery – Axial Power Shape

]]

5. REFERENCES

1. H. C. Honeck, "THERMOS: A Thermalization Transport Code for Reactor Lattice Calculations," BNL 5826 (1961).
2. H. Mizuta, "Analytical Expression for Factor A in Rational Escape Probability," J. Nucl. Sci. Tech. 10, 192 (1973).
3. H. Mizuta and M. Yamamoto, "Improved Intermediate Resonance Approximation in Heterogeneous System", J. Nucl. Sci. Tech., 21, 161 (1984).
4. T.R. England and B.F. Rider, "Evaluation and Compilation of Fission Product Yields", 1993.
5. General Electric BWR Thermal Analysis Basis (GETAB): Data, Correlation and Design Application, NEDO-10958-A, January 1977.
6. Letter from R. J. Reda (GE) to R. C. Jones (NRC), MFN-098-96, "Implementation of Improved GE Steady-State Methods"; July 2, 1996.
7. Letter from Stuart A. Richards to Glen A. Watford, "Amendment 26 to GE Licensing Topical Report NEDE-24011-P-A, GESTAR II - Implementing Improved GE Steady-State Methods (TAC No. MA6481)," November 10, 1999.
8. Global Nuclear Fuel, "GE14 Compliance With Amendment 22 of NEDE-24011-P-A (GESTAR II)," NEDC-32868P, Rev. 2, September 2007.
9. R. C. Stirn, "Generation of Void and Doppler Reactivity Feedback for Application to BWR Design," NEDO-20964, December 1975.
10. General Electric Company, "BWR/4,5,6 Standard Safety Analysis Report," Revision 2, Chapter 4, June 1977.
11. R. L. Crowther, "Xenon Considerations in Design of Large Boiling Water Reactors," APED-5640, June 1968.
12. General Electric Company, "TRACG Application for ESBWR Stability Analysis," NEDE-33083, Supplement 1, B. S. Shiralkar, et al., December 2004.
13. General Electric Company, "GE14 for ESBWR - Critical Power Correlation, Uncertainty, and OLMCPR Development", NEDC-33237P, S. Congdon, et al., March 2006.
14. General Electric Company, "GE14 for ESBWR Fuel Rod Thermal-Mechanical Design Report", NEDC-33242P, S.B. Shelton, R.A. Rand, January 2006.

Enclosure 3

MFN 09-210

**Submittal of NEDC-33239P Revision 4
and
NEDO-33239 Revision 4**

“GE14 for ESBWR Nuclear Design Report”

Affidavit

Global Nuclear Fuel – Americas, LLC

AFFIDAVIT

I, **Andrew A. Lingenfelter**, state as follows:

- (1) I am Vice President, Fuel Engineering, Global Nuclear Fuel – Americas, L.L.C. (“GNF-A”), and have been delegated the function of reviewing the information described in paragraph (2) which is sought to be withheld, and have been authorized to apply for its withholding.
- (2) The information sought to be withheld is contained in Enclosure 1 of GEH’s letter, MFN 09-210, Mr. Richard E. Kingston to U.S. Nuclear Energy Commission, entitled *Submittal of NEDC-33239P Revision 4 and NEDO-33239 Revision 4 “GE14 for ESBWR Nuclear Design Report”* dated March 31, 2009. The proprietary information in Enclosure 1, which is entitled *MFN 09-210 – Submittal of NEDC-33239P Revision 4 “GE14 for ESBWR Nuclear Design Report” – GNF Proprietary Information*, is delineated by a [[dotted underline inside double square brackets⁽³⁾]]. Figures and large equation objects are identified with double square brackets before and after the object. In each case, the superscript notation ⁽³⁾ refers to Paragraph (3) of this affidavit, which provides the basis for the proprietary determination.
- (3) In making this application for withholding of proprietary information of which it is the owner or licensee, GNF-A relies upon the exemption from disclosure set forth in the Freedom of Information Act (“FOIA”), 5 USC Sec. 552(b)(4), and the Trade Secrets Act, 18 USC Sec. 1905, and NRC regulations 10 CFR 9.17(a)(4), and 2.390(a)(4) for “trade secrets” (Exemption 4). The material for which exemption from disclosure is here sought also qualify under the narrower definition of “trade secret”, within the meanings assigned to those terms for purposes of FOIA Exemption 4 in, respectively, Critical Mass Energy Project v. Nuclear Regulatory Commission, 975F2d871 (DC Cir. 1992), and Public Citizen Health Research Group v. FDA, 704F2d1280 (DC Cir. 1983).
- (4) Some examples of categories of information which fit into the definition of proprietary information are:
 - a. Information that discloses a process, method, or apparatus, including supporting data and analyses, where prevention of its use by GNF-A’s competitors without license from GNF-A constitutes a competitive economic advantage over other companies;
 - b. Information which, if used by a competitor, would reduce his expenditure of resources or improve his competitive position in the design, manufacture, shipment, installation, assurance of quality, or licensing of a similar product;

- c. Information which reveals aspects of past, present, or future GNF-A customer-funded development plans and programs, resulting in potential products to GNF-A;
- d. Information which discloses patentable subject matter for which it may be desirable to obtain patent protection.

The information sought to be withheld is considered to be proprietary for the reasons set forth in paragraphs (4)a. and (4)b. above.

- (5) To address 10 CFR 2.390(b)(4), the information sought to be withheld is being submitted to NRC in confidence. The information is of a sort customarily held in confidence by GNF-A, and is in fact so held. The information sought to be withheld has, to the best of my knowledge and belief, consistently been held in confidence by GNF-A, no public disclosure has been made, and it is not available in public sources. All disclosures to third parties, including any required transmittals to NRC, have been made, or must be made, pursuant to regulatory provisions or proprietary agreements which provide for maintenance of the information in confidence. Its initial designation as proprietary information, and the subsequent steps taken to prevent its unauthorized disclosure, are as set forth in paragraphs (6) and (7) following.
- (6) Initial approval of proprietary treatment of a document is made by the manager of the originating component, the person most likely to be acquainted with the value and sensitivity of the information in relation to industry knowledge, or subject to the terms under which it was licensed to GNF-A. Access to such documents within GNF-A is limited on a "need to know" basis.
- (7) The procedure for approval of external release of such a document typically requires review by the staff manager, project manager, principal scientist, or other equivalent authority for technical content, competitive effect, and determination of the accuracy of the proprietary designation. Disclosures outside GNF-A are limited to regulatory bodies, customers, and potential customers, and their agents, suppliers, and licensees, and others with a legitimate need for the information, and then only in accordance with appropriate regulatory provisions or proprietary agreements.
- (8) The information identified in paragraph (2) is classified as proprietary because it contains details of GNF-A's fuel design and licensing methodology. The development of the methods used in these analyses, along with the testing, development and approval of the supporting methodology was achieved at a significant cost to GNF-A.
- (9) Public disclosure of the information sought to be withheld is likely to cause substantial harm to GNF-A's competitive position and foreclose or reduce the availability of profit-making opportunities. The information is part of GNF-A's comprehensive BWR safety and technology base, and its commercial value extends beyond the original development cost. The value of the technology base

goes beyond the extensive physical database and analytical methodology and includes development of the expertise to determine and apply the appropriate evaluation process. In addition, the technology base includes the value derived from providing analyses done with NRC-approved methods.

The research, development, engineering, analytical and NRC review costs comprise a substantial investment of time and money by GNF-A.

The precise value of the expertise to devise an evaluation process and apply the correct analytical methodology is difficult to quantify, but it clearly is substantial.

GNF-A's competitive advantage will be lost if its competitors are able to use the results of the GNF-A experience to normalize or verify their own process or if they are able to claim an equivalent understanding by demonstrating that they can arrive at the same or similar conclusions.

The value of this information to GNF-A would be lost if the information were disclosed to the public. Making such information available to competitors without their having been required to undertake a similar expenditure of resources would unfairly provide competitors with a windfall, and deprive GNF-A of the opportunity to exercise its competitive advantage to seek an adequate return on its large investment in developing and obtaining these very valuable analytical tools.

I declare under penalty of perjury that the foregoing affidavit and the matters stated therein are true and correct to the best of my knowledge, information, and belief.

Executed on this 31st day of March 2009.

Andrew A. Lingenfelter
Global Nuclear Fuel – Americas, L.L.C

goes beyond the extensive physical database and analytical methodology and includes development of the expertise to determine and apply the appropriate evaluation process. In addition, the technology base includes the value derived from providing analyses done with NRC-approved methods.

The research, development, engineering, analytical and NRC review costs comprise a substantial investment of time and money by GNF-A.

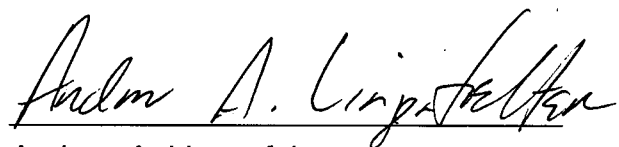
The precise value of the expertise to devise an evaluation process and apply the correct analytical methodology is difficult to quantify, but it clearly is substantial.

GNF-A's competitive advantage will be lost if its competitors are able to use the results of the GNF-A experience to normalize or verify their own process or if they are able to claim an equivalent understanding by demonstrating that they can arrive at the same or similar conclusions.

The value of this information to GNF-A would be lost if the information were disclosed to the public. Making such information available to competitors without their having been required to undertake a similar expenditure of resources would unfairly provide competitors with a windfall, and deprive GNF-A of the opportunity to exercise its competitive advantage to seek an adequate return on its large investment in developing and obtaining these very valuable analytical tools.

I declare under penalty of perjury that the foregoing affidavit and the matters stated therein are true and correct to the best of my knowledge, information, and belief.

Executed on this 31st day of March 2009.



Andrew A. Lingenfelter
Global Nuclear Fuel – Americas, L.L.C